Measurement of *CP* Violation in $B^0 \to J/\psi K^0_S$ Decays with the LHCb Experiment

Dissertation zur Erlangung des akademischen Grades

Dr. rer. nat.

vorgelegt von

Julian Tarek Wishahi

aus Mainz

Fakultät Physik
Technische Universität Dortmund

Dortmund, im November 2013

Der Fakultät Physik der Technischen Universität Dortmund zur Erlangung des akademischen Grades eines Doktors der Naturwissenschaften vorgelegte Dissertation.

Abstract

This thesis presents the LHCb measurement of CP violation in decays of neutral B^0 mesons and their anti-particles into the $J/\psi K_S^0$ final state. The interference of the B^0–$\bar{B}^0$ mixing with the decay into the common final state leads to a decay time dependent decay rate asymmetry between B^0 and $\bar{B}^0$ mesons. The CP observables, $S_{J/\psi K_S^0}$ and $C_{J/\psi K_S^0}$, allow for a determination of the CKM angle β, which is one of the most precisely measured CP parameters of the Standard Model. Thus, $B^0 \to J/\psi K_S^0$ represents an excellent reference channel for decay time dependent CP measurements at LHCb.

The analysis is performed with a dataset that corresponds to $1\,\text{fb}^{-1}$ of pp collisions collected at a centre-of-mass energy of $7\,\text{TeV}$ by the LHCb experiment at CERN. Using an unbinned maximum likelihood fit, the CP observables are measured as

$$S_{J/\psi K_S^0} = 0.73 \pm 0.07\,(\text{stat.}) \pm 0.04\,(\text{syst.}) \quad \text{and}$$
$$C_{J/\psi K_S^0} = 0.03 \pm 0.09\,(\text{stat.}) \pm 0.01\,(\text{syst.}),$$

leading to the world's best measurement of these observables at a hadron collider. Furhermore, these results are consistent with the averages of previous measurements and within expectations from the Standard Model.

Zusammenfassung

Diese Arbeit beschreibt die Messung der CP-Verletzung in Zerfällen neutraler B^0-Mesonen und ihrer Antiteilchen in den $J/\psi K_S^0$ Endzustand am LHCb-Experiment. Die Interferenz zwischen der Mischung der B^0 und $\bar{B}^0$ Zustände sowie dem Zerfall in den gemeinsamen Endzustand führt zu einer Asymmetrie zwischen den zeitabhängigen Zerfallsraten der B^0- und $\bar{B}^0$-Mesonen. Die dabei relevanten CP-Observablen $S_{J/\psi K_S^0}$ und $C_{J/\psi K_S^0}$ ermöglichen die Bestimmung des CKM-Winkels β. Dieser gehört zu den am präzisesten gemessenen CP-Parametern des Standardmodells, so dass $B^0 \to J/\psi K_S^0$ einen idealen Referenzkanal für zeitabhängige CP-Messungen bei LHCb darstellt.

Die Messung wird mit einem von LHCb aufgenommenen Datensatz durchgeführt. Dieser wurde mit Hilfe von pp-Kollisionen bei einer Schwerpunktsenergie von $7\,\text{TeV}$ gewonnen und entspricht einer integrierten Luminosität von $1\,\text{fb}^{-1}$. Ein ungebinnter Maximum-Likelihood Fit ergibt für die CP-Observablen

$$S_{J/\psi K_S^0} = 0.73 \pm 0.07\,(\text{stat.}) \pm 0.04\,(\text{syst.}) \quad \text{und}$$
$$C_{J/\psi K_S^0} = 0.03 \pm 0.09\,(\text{stat.}) \pm 0.01\,(\text{syst.}).$$

Die Ergebnisse sind in guter Übereinstimmung mit bisherigen Messungen und den Vorhersagen des Standardmodells. Gleichzeitig stellen sie die weltbeste Messung von zeitabhängiger CP-Verletzung im Zerfallskanal $B^0 \to J/\psi K_S^0$ an einem Hadronenbeschleuniger dar.

Contents

Contents

Introduction

Symmetries have played, and still do play, a fundamental role in physics. For instance, the conservation of energy and momentum can be related to the invariance of a system under translations in time and space, respectively. Actually, any continuous symmetry operation that leaves a system invariant implies a conservation law, as stated in Noether's theorem [1]. In a more abstract sense, symmetries can define the form of physical laws, similar to the role of physical laws in describing events in nature [2]. However, many of the discovered symmetries have turned out to be more or less broken. These broken symmetries are found to be important, as the search for reasons and consequences of a violated symmetry opens the way to physics beyond the generally accepted theories, the way to "New Physics".

Discrete symmetry operations, in particular the particle-anti-particle conjugation C, the parity P, and the time reversal T, play an outstanding part in the search for New Physics. For a long time, all elementary processes were assumed to be invariant under each of these transformations. First doubt on these assumptions was cast by the work of Lee and Yang, who questioned the validity of parity conservation in weak interactions [3]. Shortly after, in 1956, Wu et al. analysed the β^- decay of ^{60}Co and revealed that the weak interaction only couples to neutrinos with left-handed helicity, hereby maximally violating P symmetry [4]. Additionally, the weak interaction only couples to right-handed antineutrinos and thus violates C symmetry. However, the product of both symmetries, CP, seemed to be conserved.

Eight years later, in 1964, a small violation of the assumed CP symmetry was observed by Christenson, Cronin, Fitch, and Turlay in decays of neutral kaons [5]. As was pointed out by Kobayashi and Maskawa in 1973, this CP violation could be explained by introducing a third quark generation allowing for a complex phase in the quark mixing matrix, later known as Cabibbo-Kobayashi-Maskawa (CKM) matrix [6, 7]. Consequently, CP violating effects were expected in other heavy quark systems [8]. However, it took another 28 years to experimentally establish CP violation outside the kaon system.

Experimental evidence for the b quark, the lighter of the third generation quarks, was found by Lederman et al. in 1977 after observing bottomonium production in proton-nucleus collisions [9]. In 2001, the BaBar and Belle collaborations observed CP violation in the system of neutral B^0 mesons by measuring the time-dependent difference in decay rates in the "golden decay" of B^0 and $\bar{B}^0$ mesons into the common final state $J/\psi K_S^0$ [10, 11]. Here, the label "golden" emphasises the theoretical cleanliness of the channel. The extent of CP violation in this channel is proportional to $\sin 2\beta$, where β is one of the parameters that can be used to parameterise the CKM matrix. By now, $\sin 2\beta$ is one of the most accurately determined CP parameters, with an experimental uncertainty of less than 4% [12].

Today, CP violation in weak interactions is well embedded in the Standard Model of particle physics, which describes the strong, weak, and electromagnetic interactions of the fundamental fermions – the quarks and leptons [13–15]. As any other relativistic renormalisable

quantum field theory, it is inherently invariant under the combined *CPT* operation, but allows for *C*, *P*, and *T* (and hence *CP*) violation. Hereby, the CKM matrix plays the key role in describing *CP* violation in weak charged current transitions of quarks. In contrast, the weak neutral current, the strong, and the electromagnetic interaction are *CP* conserving. On the level of elementary interactions, the Standard Model consistently describes all *CP* violating effects, and furthermore, all processes of elementary particles measured so far. All predicted particles have been observed experimentally, with the latest example being the Higgs boson [16–18], for which a promising candidate has been recently discovered by the ATLAS and CMS collaborations [19, 20].

Though, in spite of its overwhelming success, the Standard Model cannot be deemed the final theory of everything. Some obvious reasons are its lack of a description of the gravitational force and its seemingly unmotivated 18 free parameters (7 more when neutrino masses are considered). Furthermore, it does not offer explanations for dark matter or dark energy, which make up about 27% and 68% of the energy content in today's universe, respectively [21].

A more subtle deficiency of the Standard Model is related to the dominance of matter over antimatter in the universe. In the Big Bang, around 13.8 billion years ago, matter and antimatter should have been produced in equal amounts, assuming an initial state with all charge quantum numbers equal to zero. However, in today's universe no signs of large amounts of antimatter are observed. In 1967, after the discovery of *CP* violation in the kaon system, Sakharov formulated three conditions [22] that together would allow for a dynamical emergence of a baryon asymmetry in the early evolution of the universe: Baryon number violation, *C* and *CP* violation, and departure from thermal equilibrium. Although *C* and *CP* violation seem to be properly described in the Standard Model, at least at the level of interactions of elementary particles, the CKM mechanism cannot explain the extent of the baryon asymmetry in the universe.

All of the above reasons, together with the necessity of searching for the Higgs particle and exploring the Higgs sector, which is profoundly linked to the CKM sector through the quark-mass-generating Yukawa couplings, have led to the planning and construction of the Large Hadron Collider (LHC) at the European Organisation for Nuclear Research (CERN). Equipped with four large experiments, the LHC aims at more stringent tests of the Standard Model by searching for signatures that point to New Physics. Normal operation of the LHC began in late 2009 and has only been suspended in early 2013 for a two-year shut-down, which allows both the experiments and the collider to prepare for the next data taking period.

One of the experiments is the Large Hadron Collider beauty (LHCb) experiment. It pursues an indirect search for New Physics, i.e. it performs precision measurements of observables whose precise predictions in the Standard Model could be altered by yet unknown particles or underlying mechanisms. Hereby, LHCb focusses on measuring observables in decays of *b*- and *c*-hadrons, like *CP* violating parameters or branching ratios of rare decays. Among LHCb's main foci is the precise measurement of *CP* violation in the system of neutral *B* mesons. Its access to the B_s^0 meson system extends its research field far beyond the capabilities of the former experiments BaBar and Belle, which are often referred to as the *B* factories. Although the harsh conditions at a hadron collider, involving multiple proton collisions and high track multiplicities in each event, make time-dependent *CP* measurements challenging, LHCb can profit from the large production cross-section of *b* hadrons. At the same time, it outperforms

other experiments with access to the B_s^0 system, like D0 and CDF at the Tevatron or ATLAS and CMS at the LHC, with its highly specialised equipment, e.g. its vertex detector and its particle identification systems. In particular, LHCb can pursue precision measurements of time-dependent CP asymmetries, for instance in the decay $B_s^0 \rightarrow J/\psi \phi$. An indispensable ingredient to such measurements is flavour tagging, i.e. methods to determine whether a reconstructed B meson was produced in its particle or anti-particle state. LHCb was designed to allow for flavour tagging with good performance despite the high particle multiplicity environment of LHC's pp collisions.

In addition to its efforts in the B_s^0 meson system, LHCb pursues the analysis of CP violation in the B^0 meson system. Here, the golden decay channel for CP violation, $B^0 \rightarrow J/\psi K_S^0$, is still interesting. On the one hand, the CP observable $\sin 2\beta$ has been precisely measured in this decay channel. This makes $B^0 \rightarrow J/\psi K_S^0$ a perfect reference channel for any other measurement of time-dependent CP violation, in both the B^0 and B_s^0 system, notably as benchmark for LHCb's flavour tagging. On the other hand, there is a small tension in the CKM sector between the $\sin 2\beta$ and V_{ub} measurements [23]. Clearly, the observed tension is small, but as New Physics effects have, up to now, turned out to be small as well, a further increase in experimental precision in the CKM sector is needed. It will allow for an even more stringent test of the Standard Model and its description of CP violation. With approximately two further years of data taking, LHCb will provide a $\sin 2\beta$ measurement with a better statistical precision compared to the results from the B factories.

At the same time, the upcoming higher experimental precision requires a more thorough understanding of the theoretical uncertainties, even in the "golden decay". These uncertainties arise in the determination of $\sin 2\beta$ from the measured CP observables in the $B^0 \rightarrow J/\psi K_S^0$ channel, which currently neglects the impact of CP violation at higher order. A possible approach for a better determination uses theoretical and experimental input by applying flavour symmetries. Experimentally, one of the key channels is $B_s^0 \rightarrow J/\psi K_S^0$. It has a very similar experimental signature as $B^0 \rightarrow J/\psi K_S^0$, but occurs two orders of magnitude less frequent at LHCb. Hence, the analysis of $B^0 \rightarrow J/\psi K_S^0$ decays at LHCb forms the basis for the first CP measurement in the $B_s^0 \rightarrow J/\psi K_S^0$ channel.

In this thesis, the measurement of CP violation in $B^0 \rightarrow J/\psi K_S^0$ decays with the LHCb experiment is presented. The main analysis is performed with $B^0 \rightarrow J/\psi K_S^0 \rightarrow \mu^+\mu^-\pi^+\pi^-$ candidates reconstructed in a dataset that corresponds to an integrated luminosity of $1\,\text{fb}^{-1}$ at a centre-of-mass energy of 7 TeV and was recorded in 2011. By comparing the time-dependent decay rates of B^0 and $\bar{B}^0$ mesons into the $J/\psi K_S^0$ final state, CP violation in the interference of mixing and decay can be measured, leading to the most precise determination of the CKM angle β at a hadron collider to date.

The measurement is the result of a joint effort of the LHCb groups at the Technische Universität Dortmund, Germany, and the Universidade Federal do Rio de Janeiro, Brazil, and has been published in Ref. [24]. Thus, besides the author's own work, the analysis has profited from contributions of other group members. In particular, specific studies in the context of this analysis, which have been supervised by the author, are also documented in the master's thesis of Frank Meier [25], the bachelor's thesis of Timon Schmelzer [26], the bachelor's thesis of Stefanie Roese [27], the bachelor's thesis of Tobias Tekampe [28], and the bachelor's thesis

of Margarete Schellenberg [29]. Furthermore, the analysis uses inputs from several other groups within the LHCb collaboration, especially from the flavour tagging group.

This thesis is divided into three parts:

The first part covers the theoretical foundations, beginning with a brief introduction to the Standard Model with an emphasis on the CKM sector, followed by a description of mixing and decay phenomena of neutral mesons and the influence of *CP* violation. This part ends with a thorough synopsis of the theoretical description of the $B^0 \to J/\psi K^0_S$ channel, including a discussion of the theoretical uncertainties.

In the second part, the experimental setup, i.e. the LHCb experiment, is presented. It includes a description of the various sub-detectors, as well as a description of the data taking process. Furthermore, the software framework and analysis tools are depicted, starting from the trigger, reconstruction, and selection software, and followed by a brief description of LHCb's simulation framework.

In the third part, the analysis of the $B^0 \to J/\psi K^0_S$ decays reconstructed at LHCb is explained. An introduction to the flavour tagging algorithms, which provide crucial input to the analysis by reconstructing the production flavour of each $B^0 \to J/\psi K^0_S$ candidate, and to the Decay Tree Fitter, which estimates the decay time of each $B^0 \to J/\psi K^0_S$ candidate, is given. After discussing the overall analysis strategy and the expected experimental biases that need to be accounted for, the necessary preparatory and supplemental studies are presented. For instance, the decay time resolution and flavour tagging calibration parameters, which are inputs to the final analysis, are determined. Finally, the actual measurement is presented, including the evaluation of systematic effects and subsequent estimates of systematic uncertainties.

The thesis closes with an outlook to the future development of $\sin 2\beta$ measurements, in particular in $B^0 \to J/\psi K^0_S$ decays at LHCb, and with a prospect on the *CP* measurement in $B^0_s \to J/\psi K^0_S$.

1 Symmetry Violation in the Standard Model

The Standard Model of particle physics (SM) offers a theoretical description of the dynamics of the fundamental particles and their interactions at scales of 1 fm and below. It is implemented in terms of a relativistic quantum field theory, hereby combining the realms of quantum mechanics and relativistic kinematics. As a local, Lorentz invariant quantum field theory, the SM obeys the *CPT* theorem, i.e. it is invariant under the combined *CPT* symmetry transformation. Generally, Lorentz symmetry would be broken in case of a violated *CPT* symmetry [30]. In contrast to the continuous gauge symmetries, each, *C*, *P*, and *T*, represent discrete symmetries. The parity transformation, *P*, reflects all coordinates at the origin, $r \rightarrow -r$. The charge conjugation, *C*, reverses all additive quantum numbers, e.g. charge or baryon number, while leaving linear and angular momenta unchanged. The time reversal, *T*, transforms positive to negative times, $t \rightarrow -t$. So, while *CPT* is conserved in the Standard Model by construction, it can allow for *C*, *P*, *T*, and hence *CP* violation.

1.1 Fundamental fermions and interactions

In the Standard Model, the basic constituents of matter are the fundamental fermions, the six quarks and the six leptons, which interact via bosonic force carriers. Analogously, anti-matter consists of anti-fermions, the anti-quarks and the anti-leptons. The quantum numbers of a fermion or anti-fermion, like the electric charge, the hypercharge, or the colour charge, determine its coupling strength to the different force carriers and subsequent interactions with other fermions. Three of the fundamental forces, the electromagnetic, weak, and strong force, are embedded in the Standard Model, whereas leaving out gravity.

Symmetry considerations are inherent in the Standard Model. Its most basic structure, the Dirac-Lagrangian $\mathcal{L}_0$ for a free fermion field ψ with mass m,

$$\mathcal{L}_0 = \overline{\psi}(\mathrm{i}\gamma^\mu \partial_\mu - m)\psi \,, \tag{1.1}$$

can be derived from the Poincaré group, which combines Lorentz transformations and translations in space-time. Further, the dynamics, i.e. interactions, of the fermions are introduced by requiring the Lagrangian to be invariant under local gauge transformations. For instance, Maxwell's theory of electromagnetism is generalised into Quantum Electrodynamics (QED) by requiring local $U(1)$ gauge invariance. Together with the weak interaction, it is unified to the electroweak interaction, characterised by invariance under an $SU(2) \times U(1)$ gauge group. This symmetry is spontaneously broken by the non-zero vacuum expectation value of the scalar Higgs field. Hence, electromagnetic and weak interactions become different at low

	1.	2.	3.		
Mass Charge Spin	2.3 MeV/c^2 $+^2/_3$ u $^1/_2$ up	1275 MeV/c^2 $+^2/_3$ c $^1/_2$ charm	173.5 GeV/c^2 $+^2/_3$ t $^1/_2$ top	0 $^0_1$ g gluon	126 GeV/c^2 $^0_0$ H Higgs boson

Fig. 1.1: The fundamental particles of the Standard Model and their properties. The fundamental fermions, the quarks and leptons, appear in three generations. Each generation consists of an up-type quark, a down-type quark, a charged lepton, and its corresponding neutrino. Values for the mass, electromagnetic charge, and spin are taken from Ref. [31].

momentum scales. The force carrier of electromagnetism is the massless photon γ, while the massive W^+, W^-, and Z bosons mediate the weak interaction. The particle excitation of the Higgs field is the neutral, scalar Higgs particle H. Finally, Quantum Chromodynamics (QCD), which is characterised by an $SU(3)$ gauge symmetry, describes the strong interaction of the quarks via the strong force carriers, the eight gluons. These couple to the so-called colour charge. Strongly interacting particles appear as bound states, which are called hadrons and carry a vanishing net colour charge. In total, the Standard Model describes 12 fermions and their anti-particles, 12 vector bosons, and one scalar boson, as summarised in Fig. 1.1. where the 12 fermions are organised in three generations or families.

Although QCD could accommodate for *CP* violating terms, the sole origin of *CP* violation observed experimentally can be accounted for by the charged currents in the electroweak sector of the SM. Strong *CP* violation would lead to the observation of $\eta \to \pi\pi$ decays or an electric dipole moment of the neutron, but only upper limits have been measured so far [32]. Therefore, the further discussion focuses on the electroweak sector of the SM, while a full description of the Standard Model can be found in Refs. [33, 34].

1.2 Yukawa couplings and the quark mixing matrix

In the Standard Model, the sole quark parameter with *CP* violating properties is the phase of the unitary Cabibbo-Kobayashi-Maskawa (CKM) quark mixing matrix. Its origin is the quark mass generating part of the SM Lagrangian, which requires gauge-invariant Yukawa interactions between the Higgs field and the left- and right-handed quark fields. A quark's mass is given by its specific coupling constant to the Higgs field, or more precisely to its

vacuum expectation value. Yet, the Yukawa couplings mix fermions of different generations. To obtain the mass eigenstates, the complex mass matrices for each the up-type (u, c, t) and the down-type quarks (d, s, b) needs to be diagonalised separately. Rewriting the Lagrangian in terms of quark mass eigenstates has no effect on the kinetic terms, nor on the interaction terms with the neutral gauge bosons. However, the diagonalisation matrices emerge in the charged current interaction Lagrangian, and are merged to one quark mixing matrix, the CKM matrix V_{CKM}, leading to a Lagrangian of the form

$$-\mathcal{L}_{W^{\pm}} = \frac{g}{\sqrt{2}} \left[\left(\bar{u}, \bar{c}, \bar{t}\right)_L \gamma^{\mu} W_{\mu}^{+} V_{\text{CKM}} \begin{pmatrix} d \\ s \\ b \end{pmatrix}_L + \left(\bar{d}, \bar{s}, \bar{b}\right)_L \gamma^{\mu} W_{\mu}^{-} V_{\text{CKM}}^{\dagger} \begin{pmatrix} u \\ c \\ t \end{pmatrix}_L \right]. \tag{1.2}$$

A CKM matrix element V_{ij} connects a left-handed up-type quark i of a family to a left-handed down-type quark j of the same or different family via the weak current. Hence, non-diagonal elements allow for transitions between the generations via the weak charged current with a probability proportional to $\left|V_{ij}\right|^2$. In contrast, flavour changing neutral currents are forbidden within the SM, and can therefore only be achieved by an even number of weak charged transitions.

By convention, the CKM matrix transforms the mass eigenstates of the down type quarks (d, s, b) to the electroweak eigenstates (d', s', b'),

$$\begin{pmatrix} d' \\ s' \\ b' \end{pmatrix}_L = \begin{pmatrix} V_{ud} & V_{us} & V_{ub} \\ V_{cd} & V_{cs} & V_{cb} \\ V_{td} & V_{ts} & V_{tb} \end{pmatrix} \begin{pmatrix} d \\ s \\ b \end{pmatrix}_L = V_{\text{CKM}} \begin{pmatrix} d \\ s \\ b \end{pmatrix}_L. \tag{1.3}$$

In general, any complex 3×3 matrix has 18 free parameters, but unitarity reduces the number of free parameters to three rotation angles and six complex phases. In the CKM matrix, five of these phases can be eliminated due to the freedom of choice of the relative phases of the six quark fields, leaving only one relevant complex phase. This single phase violates the *CP* symmetry of the Lagrangian in Eq. (1.2) and hereby gives rise to all *CP* violating effects in the Standard Model.

Several parametrisations of the CKM matrix exist. One of the standard parametrisations is the Chau-Keung parametrisation, which uses three rotation angles $\theta_{12}, \theta_{13}, \theta_{23} \in [0, \pi/2]$ and a phase $\delta \in (-\pi, \pi]$ [35]. Defining $s_{ij} = \sin \theta_{ij}$ and $c_{ij} = \cos \theta_{ij}$, the CKM matrix can then be exactly parameterised as

$$V_{\text{CKM}} = \begin{pmatrix} c_{12}c_{13} & s_{12}c_{13} & s_{13}e^{-i\delta} \\ -s_{12}c_{23} - c_{12}s_{23}s_{13}e^{i\delta} & c_{12}c_{23} - s_{12}s_{23}s_{13}e^{i\delta} & s_{23}c_{13} \\ s_{12}s_{23} - c_{12}c_{23}s_{13}e^{i\delta} & -c_{12}s_{23} - s_{12}c_{23}s_{13}e^{i\delta} & c_{23}c_{13} \end{pmatrix}. \tag{1.4}$$

Another parametrisation, the Wolfenstein parametrisation, is the most commonly used in experimental particle physics, although its original form only holds as an approximate parametrisation [36]. It follows the hierarchy of the off-diagonal CKM elements, i.e. $\left|V_{ub}\right|^2 \ll \left|V_{cb}\right|^2 \ll \left|V_{us}\right|^2 \ll 1$, and expresses the CKM matrix elements in terms of the expansion

parameter $\lambda = s_{12} = \sin(\theta_C) \approx 0.23$, where $\theta_C = \theta_{12}$ is the Cabibbo angle [6], and three parameters A, ρ, and η, of which all are of $\mathcal{O}(0.1)$. Using the definitions

$$s_{12} = \lambda = \frac{|V_{us}|}{\sqrt{|V_{ud}|^2 + |V_{us}|^2}}, \quad s_{23} = A\lambda^2 = \lambda \left| \frac{V_{cb}}{V_{us}} \right|, \quad s_{13}\mathrm{e}^{\mathrm{i}\delta} = V_{ub}^* = A\lambda^3(\rho + \mathrm{i}\eta), \quad (1.5)$$

the matrix can be written in terms of the parameters λ, A, $\bar{\rho}$, and $\bar{\eta}$, while achieving unitarity in all orders of λ. The Wolfenstein parametrisation up to $\mathcal{O}(\lambda^6)$ is then given by [37]

$$
V_{\mathrm{CKM}} = \begin{pmatrix} 1 - \frac{1}{2}\lambda^2 & \lambda & A\lambda^3(\rho - \mathrm{i}\eta) \\ -\lambda & 1 - \frac{1}{2}\lambda^2 & A\lambda^2 \\ A\lambda^3(1 - \rho - \mathrm{i}\eta) & -A\lambda^2 & 1 \end{pmatrix}
$$

$$
+ \begin{pmatrix} -\frac{1}{8}\lambda^4 & 0 & 0 \\ \frac{1}{2}A^2\lambda^5\,[1 - 2(\rho + \mathrm{i}\eta)] & -\frac{1}{8}\lambda^4(1 + 4A^2) & 0 \\ \frac{1}{2}A\lambda^5(\rho + \mathrm{i}\eta) & \frac{1}{2}A\lambda^4\,[1 - 2(\rho + \mathrm{i}\eta)] & -\frac{1}{2}A^2\lambda^4 \end{pmatrix} \quad (1.6)
$$

$$+ \mathcal{O}(\lambda^6).$$

The parameters $A \approx 0.82$, $\lambda \approx 0.22$, and $\rho \approx 0.13$ represent the three real parameters, and $\eta \approx 0.26$ the *CP*-violating phase of the CKM matrix.

In total, the flavour sector of the SM requires 10 parameters: six quark masses and the four parameters of the CKM matrix. Should the SM be correct, then the large variety of flavour violating processes, like meson mixing and decay, will be correctly described by this small set of parameters. This allows for a stringent test of this sector of the SM.

1.3 Unitarity triangles

The unitarity of the CKM matrix, $V_{\mathrm{CKM}}^{\dagger} V_{\mathrm{CKM}} = 1$, implies nine relations among the matrix elements. Three relations of the form

$$\sum_{i \in \{u,c,t\}} |V_{ij}|^2 = 1 \quad \text{for } j \in \{d, s, b\} \tag{1.7}$$

express the universality of the overall charged coupling strength of each up type quark to all down type quarks and vice versa. Each of the other six relations, the orthogonality conditions, can be interpreted as a triangle in the complex plane. Among the resulting six "unitarity triangles", the most frequently used triangle attributes to the condition

$$V_{ud}V_{ub}^* + V_{cd}V_{cb}^* + V_{td}V_{tb}^* = 0, \tag{1.8}$$

and is often referred to as the (*bd*) triangle, hereby emphasizing the quarks involved in each addend of the unitarity condition. This as well indicates that many of the CKM parameters in this triangle play a role in processes that involve neutral B^0 mesons, which have the valence quark content $|\bar{b}d\rangle$. In contrast to most of the other unitarity triangles, all its sides are of $\mathcal{O}(A\lambda^3)$.

Dividing the condition in Eq. (1.8) by $V_{cd}V_{cb}^*$, a new, rescaled triangle with an apex

$$\bar{\rho} + i\bar{\eta} = -\frac{V_{ud}V_{ub}^*}{V_{cd}V_{cb}^*} \tag{1.9}$$

is defined. The triangle in the $(\bar{\rho}, \bar{\eta})$-plane is depicted in Fig. 1.2. Its three angles

$$\alpha = \arg\left(-\frac{V_{td}V_{tb}^*}{V_{ud}V_{ub}^*}\right), \quad \beta = \arg\left(-\frac{V_{cd}V_{cb}^*}{V_{td}V_{tb}^*}\right), \quad \gamma = \arg\left(-\frac{V_{ud}V_{ub}^*}{V_{cd}V_{cb}^*}\right), \tag{1.10}$$

and three sides

$$R_t = \left|\frac{V_{td}V_{tb}^*}{V_{cd}V_{cb}^*}\right|, \quad R_u = \left|\frac{V_{ud}V_{ub}^*}{V_{cd}V_{cb}^*}\right|, \quad R_c = \left|\frac{V_{cd}V_{cb}^*}{V_{cd}V_{cb}^*}\right|, \tag{1.11}$$

are rephasing invariant parameters, and therefore independent of the chosen CKM parametrisation. Only R_t, R_u, β, and γ are non-trivial, as $R_c = 1$ and α can be defined as $\pi - \beta - \gamma$, so that the triangle can be expressed as

$$R_t e^{-i\beta} + R_u e^{i\gamma} = 1. \tag{1.12}$$
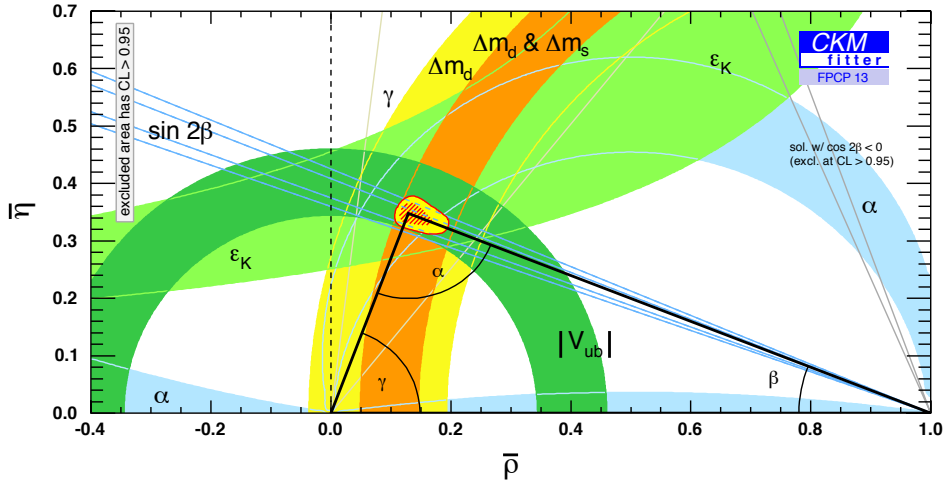
Fig. 1.2: The CKM (*bd*) triangle in the complex $(\bar{\rho}, \bar{\eta})$-plane [23, 38]. It corresponds to the unitarity relation $\sum_{q=u,c,t} V_{qd}V_{qb}^* = 0$, after dividing by $V_{cd}V_{cb}^*$, and is often referred to as "the unitarity triangle". Superimposed are the experimental constraints on the triangle's parameters. Hereby, the red hashed region represents the 68% CL (confidence level) of the result for the triangle apex from a global fit combining the experimental constraints.

Another angle of interest is β_s, which is defined as

$$\beta_s = \arg\left(-\frac{V_{ts}V_{tb}^*}{V_{cs}V_{cb}^*}\right), \tag{1.13}$$

and enters B_s^0 mixing diagrams. Thus, it is an important observable in the scope of CP violation measurements in the B_s^0 meson sector. While β_s itself is of high interest, its corresponding triangle,

$$V_{us}V_{ub}^* + V_{cs}V_{cb}^* + V_{ts}V_{tb}^* = 0\,, \tag{1.14}$$

has two sides of $\mathcal{O}(\lambda^2)$ and one of $\mathcal{O}(\lambda^4)$, and is therefore nearly degenerate, making it less attractive for rigorous tests of CKM unitarity.

While the shapes of the six triangles differ due to the hierarchy of the CKM elements, their areas all have the size of half the Jarlskog's parameter J [39],

$$J = \pm \operatorname{Im} V_{ik}V_{jl}V_{il}^*V_{jk}^* \quad \text{with } i \neq j,\ l \neq k, \tag{1.15}$$

which can be interpreted as the measure of CP violation in the electroweak sector of the Standard Model. In the Wolfenstein parametrisation, $|J| \approx \lambda^6 A^2 \eta \approx 3 \cdot 10^{-5}$.

However, even if some of the triangles' parameters are trivially connected with each other in case of a unitary CKM matrix, it is important to precisely measure them separately in as many different processes as possible. Testing the CKM sector means comparing precise, direct measurements of a parameter with the predictions obtained from other measurements under the assumption of a unitary CKM matrix. Deviations from the SM could lead to unitarity triangles with different areas, or even to non-closing triangles. A rich source of measurements with observables linked to the CKM sector is the system of neutral mesons, like the B^0 meson.

2 *CP* Violation in Neutral Mesons

In the valence quark model, meson states $|q\bar{q}'\rangle$ consist of a quark and an anti-quark. To form neutral mesons, both quarks need to be either up- or down-type quarks. Neutral mesons consisting of the same quark and anti-quark, e.g. $|\phi\rangle = |s\bar{s}\rangle$, decay dominantly via the strong and electromagnetic interaction. In contrast, ground-state mesons that consist of different quark and anti-quark type, e.g. $|B^0\rangle = |\bar{b}d\rangle$, can only decay via the weak interaction, hereby allowing for *CP* violation and mixing into their anti-particles. In this chapter, the formalism for the description of mixing and decay of such neutral mesons, further denoted as P^0, is developed, hereby closely following the description in Ref. [31, 40–42]. If not stated otherwise, *CPT* symmetry is assumed to be conserved.

2.1 Neutral meson decays

Neutral meson flavour eigenstates $|P^0\rangle$ and $|\bar{P}^0\rangle$, with common mass m but opposite flavour content, are eigenstates of the strong and the electromagnetic interaction. Here, P^0 may refer to the K^0, D^0, B^0, or B_s^0 mesons. As they can only reach other states through the weak interaction, both real and virtual transitions to common states of particle and anti-particle are possible. Hence, P^0 and $\bar{P}^0$ can mix, i.e. oscillate between each other, before decaying.

The decay into a final state $|f\rangle$ and its *CP*-conjugate state $|\bar{f}\rangle$ can be expressed by four possible decay amplitudes,

$$
\begin{aligned}
A_f &= \langle f|H|P^0\rangle \,, & \overline{A}_f &= \langle f|H|\bar{P}^0\rangle \,, \\
A_{\bar{f}} &= \langle \bar{f}|H|P^0\rangle \,, & \overline{A}_{\bar{f}} &= \langle \bar{f}|H|\bar{P}^0\rangle \,,
\end{aligned}
\tag{2.1}
$$

governed by the Hamiltonian H of the weak interaction. The phase convention for *CP* conjugation is chosen such, that $(CP)^2 = 1$, hence,

$$
\begin{aligned}
CP|P^0\rangle &= e^{+i\xi_{P^0}}|\bar{P}^0\rangle \,, & CP|f\rangle &= e^{+i\xi_f}|\bar{f}\rangle \,, \\
CP|\bar{P}^0\rangle &= e^{-i\xi_{P^0}}|P^0\rangle \,, & CP|\bar{f}\rangle &= e^{-i\xi_f}|f\rangle \,.
\end{aligned}
\tag{2.2}
$$

where the phases ξ_f and ξ_{P^0} depend on the parity of the wave functions and the flavour content. Conservation of *CP* would lead to $\overline{A}_{\bar{f}} = e^{i(\xi_f - \xi_{P^0})}A_f$, hence, $|\overline{A}_{\bar{f}}| = |A_f|$.

2.2 Mixing formalism

In the Wigner–Weisskopf approximation [43, 44], the oscillation and decay of a P^0 meson in its restframe is given by a time-dependent wave-function

$$
|\psi(t)\rangle = \psi_1(t)|P^0\rangle + \psi_2(t)|\bar{P}^0\rangle \,.
\tag{2.3}
$$

Its evolution with proper time t, which is assumed to be large compared to the typical time-scale of the strong interaction in which the meson is produced, is given by a Schrödinger-like differential equation

$$ i\frac{d}{dt}\begin{pmatrix}\psi_1\\\psi_2\end{pmatrix} = \boldsymbol{H}\begin{pmatrix}\psi_1\\\psi_2\end{pmatrix} = (\boldsymbol{M} - \tfrac{i}{2}\boldsymbol{\Gamma})\begin{pmatrix}\psi_1\\\psi_2\end{pmatrix}, \tag{2.4}$$

with the Hermitian 2×2 matrices $\boldsymbol{M}$ and $\boldsymbol{\Gamma}$. Hence, the Hamiltonian $\boldsymbol{H}$ is non-Hermitian and allows for P^0 meson decays. As CPT symmetry is assumed to hold, the masses and decay widths of the particle and anti-particle state are required to be identical, leading to $M_{11} = M_{22} \equiv m$, $M_{21} = M_{12}^*$, $\Gamma_{11} = \Gamma_{22} \equiv \Gamma$, and $\Gamma_{21} = \Gamma_{12}^*$, and hence

$$ \boldsymbol{H}\begin{pmatrix}\psi_1\\\psi_2\end{pmatrix} = \begin{pmatrix} m - \tfrac{i}{2}\Gamma & M_{12} - \tfrac{i}{2}\Gamma_{12} \\ M_{12}^* - \tfrac{i}{2}\Gamma_{12}^* & m - \tfrac{i}{2}\Gamma \end{pmatrix}\begin{pmatrix}\psi_1\\\psi_2\end{pmatrix}. \tag{2.5}$$

Virtual intermediate states contribute to the matrix $\boldsymbol{M}$ (dispersive transitions), while physical states that can be reached by both P^0 and $\bar{P}^0$ contribute to $\boldsymbol{\Gamma}$ (absorptive transitions). For both, the diagonal matrix elements describe flavour-conserving transitions. Flavour-changing processes are represented by the off-diagonal elements, where M_{12} quantifies short-distance contributions via off-shell states and Γ_{12} describes virtual intermediate decays to final (on-shell) states that can be reached by both P^0 and $\bar{P}^0$. A relative phase difference ϕ between these on-shell and off-shell transitions can be present and thus be written as

$$ \phi = \arg\left(\frac{M_{12}}{\Gamma_{12}}\right) = \arg\left(\frac{|M_{12}|\,e^{i\phi_M}}{|\Gamma_{12}|\,e^{i\phi_\Gamma}}\right) = \phi_M - \phi_\Gamma \tag{2.6}$$

The eigenvectors P_j of $\boldsymbol{H}$ have well defined masses and decay widths. Typically, they are chosen as the heavy mass eigenstate P_H and the light mass eigenstate P_L, which correspond to the complex eigenvalues of $\boldsymbol{H}$,

$$ \mu_H = m_H - \tfrac{i}{2}\Gamma_H = m + \operatorname{Re} F - \tfrac{i}{2}\left(\Gamma + 2\operatorname{Im} F\right), \tag{2.7a}$$

$$ \mu_L = m_L - \tfrac{i}{2}\Gamma_L = m - \operatorname{Re} F - \tfrac{i}{2}\left(\Gamma - 2\operatorname{Im} F\right), \tag{2.7b}$$

where the short-hand notation

$$ F = \sqrt{\left(M_{12} - \tfrac{i}{2}\Gamma_{12}\right)\left(M_{12}^* - \tfrac{i}{2}\Gamma_{12}^*\right)}, \tag{2.8}$$

has been used. The quantities that characterise the different meson systems are the average masses and decay widths, which are

$$ m = \frac{m_H + m_L}{2}, \qquad \Gamma = \frac{\Gamma_H + \Gamma_L}{2}, \tag{2.9}$$

and the mass and decay width differences, given as

$$ \Delta m = m_H - m_L = 2\operatorname{Re} F, \qquad \Delta\Gamma = \Gamma_H - \Gamma_L = 4\operatorname{Im} F, \tag{2.10}$$

where Δm is positive by definition while the sign of $\Delta\Gamma$ needs to be determined experimentally. Assuming CPT invariance, the states P^0 and $\bar{P}^0$ can be used to express the mass eigenstates in terms of the flavour eigenstates via

$$|P_H\rangle = p\,|P^0\rangle + q\,|\bar{P}^0\rangle\,, \qquad (2.11a)$$

$$|P_L\rangle = p\,|P^0\rangle - q\,|\bar{P}^0\rangle\,, \qquad (2.11b)$$

where the complex coefficients obey the normalisation condition $|q|^2 + |p|^2 = 1$. The ratio q/p is connected to the matrix elements of $\boldsymbol{M}$ and $\boldsymbol{\Gamma}$ via

$$\frac{q}{p} = \sqrt{\frac{M_{12}^* - \tfrac{i}{2}\Gamma_{12}^*}{M_{12} - \tfrac{i}{2}\Gamma_{12}}} = \frac{\Delta m - \tfrac{i}{2}\Delta\Gamma}{2(M_{12} - \tfrac{i}{2}\Gamma_{12})}\,. \qquad (2.12)$$

2.3 Time evolution

In contrast to the flavour eigenstates, the mass eigenstates have well-defined masses and decay widths. They follow exponential evolution laws,

$$|P_H(t)\rangle = \mathrm{e}^{-\mathrm{i}\mu_H t}\,|P_H\rangle = \mathrm{e}^{-\mathrm{i}m_H t}\mathrm{e}^{-\frac{\Gamma_H}{2}t}\,|P_H\rangle\,, \qquad (2.13a)$$

$$|P_L(t)\rangle = \mathrm{e}^{-\mathrm{i}\mu_L t}\,|P_L\rangle = \mathrm{e}^{-\mathrm{i}m_L t}\mathrm{e}^{-\frac{\Gamma_L}{2}t}\,|P_L\rangle\,, \qquad (2.13b)$$

where t always denotes the elapsed time in the particle's rest frame defined by the rest mass m of the flavour eigenstate, not by the (different) masses m_H and m_L of the two mass eigenstates.

Assuming a pure initial flavour state P^0 or $\bar{P}^0$ at proper time $t = 0$, the evolution with t, i.e. the evolution of states $|P^0(t)\rangle$ and $|\bar{P}^0(t)\rangle$, is given by combining Eq. (2.11) and Eq.(2.13), as

$$|P^0(t)\rangle = g_+(t)\,|P^0\rangle - \frac{q}{p}g_-(t)\,|\bar{P}^0\rangle\,, \qquad (2.14a)$$

$$|\bar{P}^0(t)\rangle = g_+(t)\,|\bar{P}^0\rangle - \frac{p}{q}g_-(t)\,|P^0\rangle\,, \qquad (2.14b)$$

with

$$g_\pm(t) = \frac{1}{2}\left(\mathrm{e}^{-\mathrm{i}\mu_H t} \pm \mathrm{e}^{-\mathrm{i}\mu_L t}\right) = \frac{1}{2}\left(\mathrm{e}^{-\mathrm{i}m_H t - \frac{\Gamma_H}{2}t} \pm \mathrm{e}^{-\mathrm{i}m_L t - \frac{\Gamma_L}{2}t}\right)\,. \qquad (2.15)$$

It is impossible to directly observe the time evolution of the states. However, using the strong or electromagnetic interaction, a pure initial $|P^0\rangle$ or $|\bar{P}^0\rangle$ state can be produced and its decay into a final state f or its CP conjugate $\bar{f}$ after a decay time t can be examined. Hence, experimentally one is interested in the time-dependent decay rates $\Gamma(t)$ of intial $|P^0\rangle$ or $|\bar{P}^0\rangle$ decaying at decay time t into final states $f/\bar{f}$. By defining the complex parameters

$$\lambda_f = \frac{1}{\bar{\lambda}_f} = \frac{q}{p}\frac{\overline{A}_f}{A_f}, \qquad \bar{\lambda}_{\bar{f}} = \frac{1}{\lambda_{\bar{f}}} = \frac{q}{p}\frac{A_{\bar{f}}}{\overline{A}_{\bar{f}}}. \qquad (2.16)$$

and assuming that terms of the form $|A_f|^2$, $|A_{\bar{f}}|^2$, $|\overline{A}_f|^2$, and $|\overline{A}_{\bar{f}}|^2$ include all phase-space factors and integrations, the differential decay rates

$$\Gamma(P^0(t) \to f) = \left|\langle f|H|P^0(t)\rangle\right|^2, \quad \Gamma(\bar{P}^0(t) \to f) = \left|\langle f|H|\bar{P}^0(t)\rangle\right|^2,$$

$$\Gamma(P^0(t) \to \bar{f}) = \left|\langle \bar{f}|H|P^0(t)\rangle\right|^2, \quad \Gamma(\bar{P}^0(t) \to \bar{f}) = \left|\langle \bar{f}|H|\bar{P}^0(t)\rangle\right|^2, \qquad (2.17)$$

can be expressed as

$$\Gamma(P^0(t) \to f) = |A_f|^2 \quad \left[|g_+(t)|^2 + |\lambda_f|^2 |g_-(t)|^2 + 2\,\mathrm{Re}\left(\lambda_f g_+^*(t) g_-(t) \right) \right],$$

$$\Gamma(\bar{P}^0(t) \to f) = |A_f|^2 \left|\frac{p}{q}\right|^2 \left[|g_-(t)|^2 + |\lambda_f|^2 |g_+(t)|^2 + 2\,\mathrm{Re}\left(\lambda_f g_+(t) g_-^*(t) \right) \right],$$

$$\Gamma(P^0(t) \to \bar{f}) = |\bar{A}_{\bar{f}}|^2 \left|\frac{q}{p}\right|^2 \left[|g_-(t)|^2 + |\bar{\lambda}_{\bar{f}}|^2 |g_+(t)|^2 + 2\,\mathrm{Re}\left(\bar{\lambda}_{\bar{f}} g_+(t) g_-^*(t) \right) \right],$$

$$\Gamma(\bar{P}^0(t) \to \bar{f}) = |\bar{A}_{\bar{f}}|^2 \quad \left[|g_+(t)|^2 + |\bar{\lambda}_{\bar{f}}|^2 |g_-(t)|^2 + 2\,\mathrm{Re}\left(\bar{\lambda}_{\bar{f}} g_+^*(t) g_-(t) \right) \right], \quad (2.18)$$

with

$$|g_\pm(t)|^2 = \frac{e^{-\Gamma t}}{2} \left[\cosh\left(\frac{\Delta\Gamma t}{2}\right) \pm \cos(\Delta m t) \right], \quad (2.19)$$

$$g_+^*(t) g_-(t) = \frac{e^{-\Gamma t}}{2} \left[\sinh\left(\frac{\Delta\Gamma t}{2}\right) + i\sin(\Delta m t) \right]. \quad (2.20)$$

The terms that are proportional to $|A|^2$ represent decays without any net oscillation, while decay rates proportional to $|p/q A|^2$, or $|q/p A|^2$ represent decays with a net oscillation. The terms proportional to $\left(g_\pm^*(t) g_\mp(t) \right)$ and hence to $\sin(\Delta m t)$ and $\sinh(\Delta\Gamma t/2)$ result from the interference of both.

The resulting full expressions can be significantly simplified by introducing the derived *CP* observables

$$D_f = \frac{2\,\mathrm{Re}\,\lambda_f}{1 + |\lambda_f|^2}, \qquad C_f = \frac{1 - |\lambda_f|^2}{1 + |\lambda_f|^2}, \qquad S_f = \frac{2\,\mathrm{Im}\,\lambda_f}{1 + |\lambda_f|^2}, \quad (2.21)$$

$$D_{\bar{f}} = \frac{2\,\mathrm{Re}\,\bar{\lambda}_{\bar{f}}}{1 + |\bar{\lambda}_{\bar{f}}|^2}, \qquad C_{\bar{f}} = \frac{1 - |\bar{\lambda}_{\bar{f}}|^2}{1 + |\bar{\lambda}_{\bar{f}}|^2}, \qquad S_{\bar{f}} = \frac{2\,\mathrm{Im}\,\bar{\lambda}_{\bar{f}}}{1 + |\bar{\lambda}_{\bar{f}}|^2}, \quad (2.22)$$

which satisfy

$$D_f^2 + C_f^2 + S_f^2 = 1 \qquad \text{and} \qquad D_{\bar{f}}^2 + C_{\bar{f}}^2 + S_{\bar{f}}^2 = 1. \quad (2.23)$$

Then, using Eq. (2.21) and (2.22), and the time-evolutions from Eq. (2.18), (2.19), and (2.20), the time-dependent decay rates can be parametrised as

$$
\frac{\Gamma(P^0(t) \to f)}{e^{-\Gamma t}} = \quad \frac{1}{2}|A_f|^2\left(1+|\lambda_f|^2\right)\Bigg[\quad \cosh\left(\frac{\Delta\Gamma}{2}t\right)+D_f\sinh\left(\frac{\Delta\Gamma}{2}t\right)
$$
$$
+C_f\cos\left(\Delta mt\right)-S_f\sin\left(\Delta mt\right) \quad \Bigg], \qquad (2.24a)
$$

$$
\frac{\Gamma(\overline{P}^0(t) \to f)}{e^{-\Gamma t}} = \frac{1}{2}|A_f|^2\left|\frac{p}{q}\right|^2\left(1+|\lambda_f|^2\right)\Bigg[\quad \cosh\left(\frac{\Delta\Gamma}{2}t\right)+D_f\sinh\left(\frac{\Delta\Gamma}{2}t\right)
$$
$$
-C_f\cos\left(\Delta mt\right)+S_f\sin\left(\Delta mt\right) \quad \Bigg], \qquad (2.24b)
$$

$$
\frac{\Gamma(P^0(t) \to \bar{f})}{e^{-\Gamma t}} = \frac{1}{2}|\overline{A}_{\bar{f}}|^2\left|\frac{q}{p}\right|^2\left(1+|\overline{\lambda}_{\bar{f}}|^2\right)\Bigg[\quad \cosh\left(\frac{\Delta\Gamma}{2}t\right)+D_{\bar{f}}\sinh\left(\frac{\Delta\Gamma}{2}t\right)
$$
$$
+C_{\bar{f}}\cos\left(\Delta mt\right)-S_{\bar{f}}\sin\left(\Delta mt\right) \quad \Bigg], \qquad (2.24c)
$$

$$
\frac{\Gamma(\overline{P}^0(t) \to \bar{f})}{e^{-\Gamma t}} = \quad \frac{1}{2}|\overline{A}_{\bar{f}}|^2\left(1+|\overline{\lambda}_{\bar{f}}|^2\right)\Bigg[\quad \cosh\left(\frac{\Delta\Gamma}{2}t\right)+D_{\bar{f}}\sinh\left(\frac{\Delta\Gamma}{2}t\right)
$$
$$
-C_{\bar{f}}\cos\left(\Delta mt\right)+S_{\bar{f}}\sin\left(\Delta mt\right) \quad \Bigg]. \qquad (2.24d)
$$

It is important to note, that the parameters are not necessarily constant in phase-space. For instance, in decays to multi-body final states, the parameters can strongly depend on different regions of phase-space, as the interference between different decay transitions is highly influenced by possible resonant substructures of the decay products.

2.4 Classes of *CP* violation

In the previous section, the formalism for meson decay and mixing has been developed. Assuming *CPT* invariance, all *CP* violating effects in a P^0–$\overline{P}^0$ meson system are governed by the Schrödinger-like equation developed in the last section. The resulting time-dependent decay rates can be expressed using the decay amplitudes A_f, $A_{\bar{f}}$, $\overline{A}_f$, $\overline{A}_{\bar{f}}$ and the mixing parameters q and p. However, to arrive at non-vanishing *CP* violating observables, specific conditions for the transition amplitudes and their phases need to be met.

In this context, three types of phases need to be distinguished: 'spurious', 'strong', and 'weak' phases. The spurious *CP* transformation phases, ξ_{P^0} and ξ_f, see Eq. (2.2), are global, convention-dependent phases and do not originate from any dynamics. Hence, these can be set to 0 for convenience. The strong phases arise in final-state interaction scattering from intermediate on-shell states, e.g. through strong or electromagnetic interactions. As these interactions are *CP* invariant, the strong phases are equal for two *CP* conjugate states. Weak phases originate from complex couplings in the Lagrangian. In the case of the Standard Model, these arise in the $W^\pm$ couplings to the quarks via the complex CKM matrix elements. Phases of this type change sign under *CP* conjugation. Accordingly, in the course of a further

investigation of the CKM mechanism, it is of highest interest to cleanly measure weak phases in meson decays.

It is important to note that although the existence of weak and strong phases is physically motivated, their absolute values are convention-dependent. In contrast, relative strong or weak phases between different terms in transition amplitudes are convention-independent, and hence are physically meaningful. Depending on the origin and interplay of the transitions that introduce weak phases, *CP* violating effects can be categorized as *CP* violation in the decay (direct *CP* violation), *CP* violation in the mixing (indirect *CP* violation), or *CP* violation in the interference of mixing and decay.

2.4.1 Direct *CP* violation

In the case of meson decays, multiple contributions a_i, each with different weak phases ϕ_i and strong phases δ_i, can contribute to the decay amplitudes. In the simple case of two possible transitions with amplitudes a_1 and a_2, the resulting decay amplitudes are

$$
\begin{aligned}
A_f &= \left|a_1\right| \mathrm{e}^{\mathrm{i}(\delta_1+\phi_1)} + \left|a_2\right| \mathrm{e}^{\mathrm{i}(\delta_2+\phi_2)}, \\
\overline{A}_{\bar{f}} &= \left|a_1\right| \mathrm{e}^{\mathrm{i}(\delta_1-\phi_1)} + \left|a_2\right| \mathrm{e}^{\mathrm{i}(\delta_2-\phi_2)}.
\end{aligned}
\tag{2.25}
$$

This directly implies

$$
\left|\frac{A_f}{\overline{A}_{\bar{f}}}\right| \neq 1,
\tag{2.26}
$$

leading to *CP* violation in the decay. This is the only type of *CP* violation, that can occur in charged meson systems P^+ and P^-. It leads to a time-independent asymmetry of the form

$$
A_{f\pm} = \frac{\Gamma(P^- \to f^-) - \Gamma(P^+ \to f^+)}{\Gamma(P^- \to f^-) + \Gamma(P^+ \to f^+)} = \frac{\left|\overline{A}_{\bar{f}^-}/A_{\bar{f}^+}\right|^2 - 1}{\left|\overline{A}_{\bar{f}^-}/A_{\bar{f}^+}\right|^2 + 1}.
\tag{2.27}
$$

Direct *CP* violation is well established in the B^0 system, e.g. in $B^0 \to K^+\pi^-$, and has furthermore been observed for the first time in the B_s^0 system in the decay $B_s^0 \to K^+\pi^-$ by the LHCb collaboration [45]. Using a dataset of $1\,\mathrm{fb}^{-1}$, the asymmetries are measured as

$$
\begin{aligned}
A_{K^\pm\pi^\mp}^d &= -0.080 \pm 0.007\,\text{(stat.)} \pm 0.003\,\text{(syst.)}, \\
A_{K^\pm\pi^\mp}^s &= 0.27 \pm 0.04 \,\text{(stat.)} \pm 0.01 \,\text{(syst.)},
\end{aligned}
$$

where $A_{K^\pm\pi^\mp}^d$ and $A_{K^\pm\pi^\mp}^s$ refer to the measurements in the $B^0 \to K^+\pi^-$ and $B_s^0 \to K^+\pi^-$ decays, respectively. The reconstructed mass distributions of the candidates can be seen in Fig. 2.1.

2.4.2 Indirect *CP* violation

Additional phases can arise in P^0–$\overline{P}^0$ transitions from the on-shell and off-shell contributions,

$$
M_{12} = \left|M_{12}\right| \mathrm{e}^{\mathrm{i}\phi_M}, \qquad \Gamma_{12} = \left|\Gamma_{12}\right| \mathrm{e}^{\mathrm{i}\phi_\Gamma}.
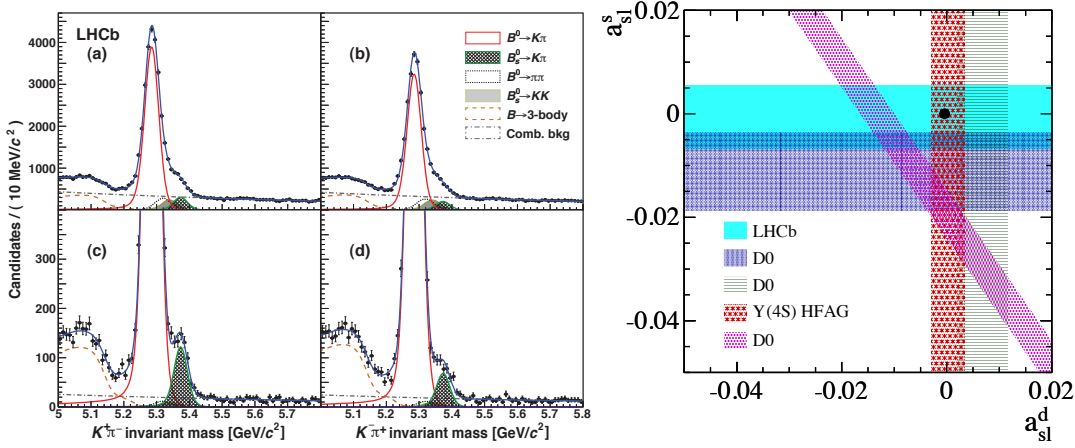\tag{2.28}
$$

Fig. 2.1: Examples of direct and indirect *CP* violation measurements by LHCb. Left: Invariant mass spectra of the $K^+\pi^-$ combinations (a,c) and the $K^-\pi^+$ combinations (b,d) [45]. In (a,b) the selection has been optimised for the B^0 channel, in (c,d) for the B_s^0 channel. The projections of the components of the unbinned maximum likelihood fit are overlaid. The raw asymmetries in the candidate yields are clearly visible. Right: Measurements of semileptonic decay asymmetries [46]. The bands correspond to the central values ±1 standard deviation of the combined statistical and systematic errors. The black dot represents the Standard Model expectation.

In case $\left|\Gamma_{12}/M_{12}\right| \neq 0$, the phase difference $\phi = \phi_M - \phi_\Gamma$ implies

$$|q/p| \neq 1, \tag{2.29}$$

hereby defining *CP* violation in the mixing. It would express itself in different mixing rates, $\Gamma(P^0 \to \bar{P}^0) \neq \Gamma(\bar{P}^0 \to P^0)$. This type of *CP* violation can be measured in semi-leptonic meson decays, where the P^0 meson exclusively decays into a final state l^+X, while $\bar{P}^0$ can only decay into l^-X. Hence, an initial P^0 ($\bar{P}^0$) meson can reach the l^-X (l^+X) final state only via mixing. Thus, *CP* violation in the mixing would then lead to an asymmetry between the time-dependent decay rates,

$$a_{sl}(t) = \frac{\Gamma(\bar{P}^0(t) \to l^+X) - \Gamma(P^0(t) \to l^-X)}{\Gamma(\bar{P}^0(t) \to l^+X) + \Gamma(P^0(t) \to l^-X)} = \frac{1 - |q/p|^2}{1 + |q/p|^2}, \tag{2.30}$$

which turns out to be independent of time.

Measurements of a_{sl}^d (a_{sl}^s) in the B^0 (B_s^0) system have been performed by several experiments, where the newest result for the B_s^0 system comes from LHCb [46, 47], and are summarised in Fig. 2.1. At the current precision, *CP* violation in the mixing of B mesons seems negligible, in good agreement with the Standard Model expectations.

2.4.3 *CP* violation in the interference of mixing and decay

Finally, *CP* violation can occur when the direct decay, $P^0 \to f$, interferes with the decay with mixing, $P^0 \to \bar{P}^0 \to f$, even if no indirect or direct *CP* violation is present. For instance, if

only one single weak phase contributes to the decay, $A_f = |a_f| e^{i(\delta_f + \phi_f)}$, and if $|\Gamma_{12}/M_{12}| = 0$, so that the mixing parameter is a pure phase, $q/p = e^{-i\phi_M}$, neither *CP* violation in the mixing nor in the decay occur separately and $|\lambda_f| = 1$. Though, the phase difference in mixing and decay leads to

$$\text{Im}\, \lambda_f \neq 0 \,, \qquad\qquad (2.31)$$

hereby defining the requirement for *CP* violation in the interference of mixing and decay. In case of decays into a final *CP* eigenstate f_{CP} with *CP* eigenvalue $\eta_f = \pm 1$, the *CP* violation leads to a time-dependent asymmetry

$$
\begin{aligned}
\mathcal{A}_{f_{CP}}(t) &= \frac{\Gamma(\overline{P}^0(t) \to f_{CP}) - \Gamma(P^0(t) \to f_{CP})}{\Gamma(\overline{P}^0(t) \to f_{CP}) + \Gamma(P^0(t) \to f_{CP})} \\
&= \frac{S_{f_{CP}} \sin(\Delta m t) - C_{f_{CP}} \cos(\Delta m t)}{\cosh\left(\frac{\Delta \Gamma t}{2}\right) + D_{f_{CP}} \sinh\left(\frac{\Delta \Gamma t}{2}\right)} \,,
\end{aligned}
\qquad (2.32)
$$

where $S_{f_{CP}} = \eta_f \sin(\phi_M + 2\phi_f) \neq 0$ (see Eq. (2.21)), if no additional direct or indirect *CP* violation is assumed, and so $C_{f_{CP}} = 0$. Additional direct or indirect *CP* violation, $|\lambda_{f_{CP}}| \neq 1$, would lead to $C_{f_{CP}} \neq 0$.

This third type of *CP* violation can be measured in the $B^0 \to J/\psi K_S^0$ decay channel and will be described more thoroughly in Ch. 3. In the B_s^0 meson system, it can be measured in the $B_s^0 \to J/\psi \phi$ channel. However, due to the two vector mesons in the final state, an angular analysis is needed to statistically disentangle the different *CP* odd and even components.

3 The $B^0 \to J/\psi K^0_S$ Decay Channel

The decay channel $B^0 \to J/\psi K^0_S$ is referred to as the golden decay for measurements of CP violation in the B^0 meson system. Here, CP violation in interference of mixing and decay allows a precise measurement of $\sin 2\beta$ at $\mathcal{O}(\%)$, as sub-leading doubly Cabibbo-suppressed contributions to the decay amplitudes are assumed to vanish. The CKM angle β can then be determined up to a four-fold ambiguity, which can be reduced to a two-fold ambiguity by measuring the sign of $\cos 2\beta$, e.g. in $B^0 \to J/\psi K^{*0}$.

First, general properties of the $B^0 \to J/\psi K^0_S$ mode and the involved mesons will be discussed, followed by a more detailed look into the mixing and decay topologies of this channel. This will partially clarify why this decay channel is one of the theoretically cleanest channels for measuring $\sin 2\beta$ in the B^0 sector. Deviations from the Standard Model expectations could be a hint at New Physics. Thus, with the new perspective of LHC experiments like LHCb and next-generation B-factories like Belle II, the expected increase in experimental precision in $\sin 2\beta$ measurements requires a revisit of the theoretical assumptions. The chapter closes with an overview of the status of $\sin 2\beta$ measurements, which are currently dominated by the results from the B factories, BaBar and Belle.

3.1 Properties of the $B^0 \to J/\psi K^0_S$ mode

The decay mode $B^0 \to J/\psi K^0_S$ involves the interference of B^0–$\bar{B}^0$ mixing and subsequent decay into the common CP eigenstate $f = J/\psi K^0_S$. In the latter and further discussion, "K^0_S" does not denote the undecayed K^0_S particle, but rather its $\pi\pi$ final state with CP eigenvalue $+1$. To reach the $J/\psi K^0_S$ final state, the B^0 meson decays into a J/ψ meson and a K^0 meson, with a branching ratio of $\mathcal{B}(B^0 \to J/\psi K^0) = (8.74 \pm 0.32) \cdot 10^{-4}$ [31]. As the $K^0/\bar{K}^0$ flavour eigenstates need to decay via the K^0_S mass eigenstate, the overall branching ratio is further reduced by 50%.

The B^0 meson is one of the four ground-state $J^P = 0^-$ b-flavoured mesons with masses $\mathcal{O}(5\,\mathrm{GeV}/c^2)$ and decay times $\mathcal{O}(1\,\mathrm{ps})$ [31]. A summary of the properties of the B mesons is given in Tab. 3.1. The J/ψ meson, which is a $c\bar{c}$ quarkonium state, has a mass of $(3096.916 \pm 0.011)\,\mathrm{MeV}/c^2$ and a large decay width of $(92.9 \pm 2.8)\,\mathrm{keV}$, which corresponds to a lifetime of $7 \cdot 10^{-9}\,\mathrm{ps}$. In contrast, the K^0 meson, with a valence quark content $(d, \bar{s})$, has a mass of only $(497.614 \pm 0.024)\,\mathrm{MeV}/c^2$ and its K^0_S mass eigenstate has a considerably large lifetime of $(89.54 \pm 0.04)\,\mathrm{ps}$.

The CP eigenvalue $\eta_f = \eta_{J/\psi K^0_S}$ of the final state is given by the interplay of intrinsic CP eigenvalues of the decay products, their spins, and relative angular momenta. The B^0 meson decays into the vector meson J/ψ, which is CP even, and the K^0_S, which has spin zero and is almost CP-even. As the B^0 is a pseudoscalar meson, the $J/\psi K^0_S$ system must carry a

Tab. 3.1: Properties of the ground-state B mesons [31], where m is the mass and τ is the lifetime. For the neutral mesons, Δm is the mass difference of the high and low mass eigenstates and $\Delta\Gamma/\Gamma$ is their decay width difference with respect to the total decay width $\Gamma = \hbar/\tau$.

B meson	quarks	m [MeV/c^2]	τ [ps]	Δm [$\hbar$ps^{-1}]	$\Delta\Gamma/\Gamma$
B^0	$(d, \bar{b})$	5279.58 ± 0.17	1.519 ± 0.007	0.507 ± 0.04	0.015 ± 0.018
B^0_s	$(d, \bar{b})$	5366.77 ± 0.24	1.497 ± 0.015	17.69 ± 0.08	0.150 ± 0.020
B^+	$(u, \bar{b})$	5279.25 ± 0.17	1.641 ± 0.008	—	—
B^+_c	$(c, \bar{b})$	6277 ± 6	0.453 ± 0.041	—	—

relative angular momentum of $l = 1$. Hence, the $J/\psi K^0_S$ final state is *CP*-odd, $\eta_{J/\psi K^0_S} = -1$. Interference *CP* violation in the $B^0 \to J/\psi K^0_S$ mode is characterised by the parameter

$$\lambda_{J/\psi K^0_S} = \frac{q}{p} \frac{\overline{A}_{J/\psi K^0_S}}{A_{J/\psi K^0_S}} . \tag{3.1}$$

In the following sections, expressions for q/p and $\overline{A}_{J/\psi K^0_S}/A_{J/\psi K^0_S}$ will be developed.

3.2 B^0–$\bar{B}^0$ mixing

As described in Ch. 2, the time-dependent mixing of the flavour eigenstates $|B^0\rangle$ and $|\bar{B}^0\rangle$ is determined by the mass difference Δm and the decay width difference $\Delta\Gamma$ of the mass eigenstates, here $|B^0_H\rangle$ and $|B^0_L\rangle$, and by the mixing parameter q/p. All of these quantities are related to the off-diagonal matrix element $M_{12} - \frac{i}{2}\Gamma_{12}$, see Eqs. (2.10) and (2.12). Consequently, a Standard Model description of mixing phenomena and interference *CP* violation in the B^0 system requires the calculation of M_{12} and Γ_{12}, which describe the dispersive and absorptive mixing transitions, respectively.

The B^0–$\bar{B}^0$ mixing is mediated through transitions that change the beauty quantum number by 2. In the Standard Model, these transitions must be – at lowest order – second order weak interactions. In general, both quark-level ("short distance") and hadron-level ("long distance") transitions contribute to mixing. However, in the B^0 system, mixing is dominated by short-distance box-diagram transitions [40, 48], with exchange of two W bosons and two up-type quarks.

The main contributions to M_{12}, which describes the "mass mixing" [49, 50], are the short-distance box-diagrams depicted in Fig. 3.1, and include loops with all up-type quarks. Using an effective Hamiltonian for the quark transition $\bar{b}d \to b\bar{d}$, the matrix element can be calculated as

$$M_{12} = -\frac{G_F^2 m_W^2}{12\pi^2} mBf^2 \mathcal{F}^* , \tag{3.2}$$

where G_F is the Fermi constant, m_W is the W boson mass, and m is the B^0 meson mass. The parameters f and B are the weak decay constant and the bag parameter, respectively, which describe corrections from non-perturbative QCD that take into account the transition from
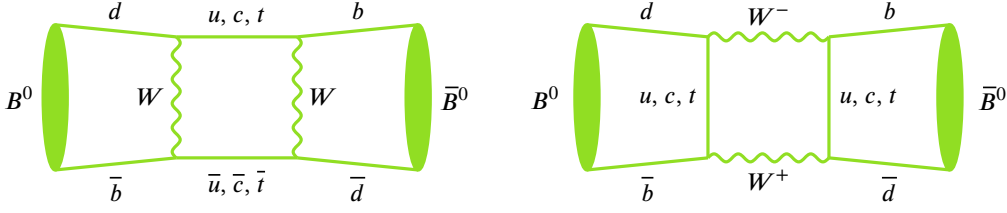
Fig. 3.1: The box diagrams mediate $|\Delta B| = 2$ transitions and represent the dominant Feynman diagrams for B^0–$\bar{B}^0$ mixing that contribute to M_{12}.

bound to free quarks. Furthermore, $\mathcal{F}$ is a factor which subsumes the different box diagrams and involved CKM matrix elements $V_{qq'}$,

$$
\begin{aligned}
\mathcal{F} = {} & \eta_1 (V_{cb}^* V_{cd})^2 S_0\left(x_c^2\right) + \eta_2 (V_{tb}^* V_{td})^2 S_0\left(x_t^2\right) \\
& + 2\eta_3 (V_{cb}^* V_{cd})(V_{tb}^* V_{td}) S_0\left(x_c^2, x_t^2\right) .
\end{aligned}
\tag{3.3}
$$

Here, η_i are perturbative QCD corrections of $\mathcal{O}(1)$, and $S_0(x_q)$ are the Inami-Lim functions [51], which depend on the ratio x_q of the quark mass m_q to the W boson mass m_W in the loop with quark q. Both the top quark and the charm quark loop enter with CKM matrix elements of comparable magnitude, $\left|V_{td}V_{tb}\right| \approx \left|V_{cd}V_{cb}\right| \approx \lambda^3$, while the up quark loop is suppressed. Though, the fact that the values of the Inami-Lim functions obey

$$
S_0\left(x_t^2\right) \gg S_0\left(x_c^2, x_t^2\right) > S_0\left(x_c^2\right) ,
\tag{3.4}
$$

makes the top loop contribution dominant. Thus, M_{12} simplifies to

$$
M_{12} = -\frac{G_F^2 m_W^2}{12\pi^2} m B f^2 \eta_{\text{QCD}} S_0(x_t^2)(V_{td}^* V_{tb})^2 ,
\tag{3.5}
$$

with $\eta_{\text{QCD}} = \eta_2$.

For the second relevant matrix element, Γ_{12}, which describes the "width mixing" [50], the sum of all B^0–$\bar{B}^0$ transitions via real intermediate states f, common to both B^0 and $\bar{B}^0$, needs to be calculated,

$$
\Gamma_{12} = \sum_f \langle f|T|B^0\rangle^* \langle f|T|\bar{B}^0\rangle .
\tag{3.6}
$$

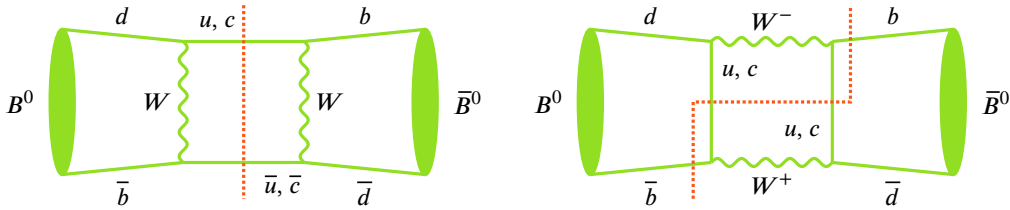These are represented by the box-diagrams shown in Fig. 3.2. Here, the loop with a t quark

Fig. 3.2: The diagrams contributing to Γ_{12} in B^0–$\bar{B}^0$ mixing. The dotted line denotes the presence of a real, intermediate state.

does not contribute, as the top quark's mass is much larger than the B^0 meson mass, and so no decays into 'top quark hadrons' are possible. Thus, both the box diagrams with intermediate u and c quarks need to be evaluated. An explicit calculation, as performed in Refs. [49, 52] and as summarised in Ref. [31], yields

$$\Gamma_{12} \approx \frac{G_F^2 m_b^2 m^2}{8\pi} \eta'_{\text{QCD}} B f^2 \left[(V_{td}^* V_{tb})^2 + V_{td}^* V_{tb} V_{cd}^* V_{cb} \, \mathcal{O} \left(m_c^2/m_b^2 \right) + (V_{cd}^* V_{cb})^2 \, \mathcal{O} \left(m_c^4/m_b^4 \right) \right], \qquad (3.7)$$

where m_q is the mass of the quark q, and η'_{QCD} is another QCD correction factor and the other parameters correspond to the ones in Eq. (3.2). Thus,

$$|\Gamma_{12}/M_{12}| \approx \frac{3\pi}{2} \frac{m_b^2}{m_W^2} \frac{1}{S_0(m_t^2/m_W^2)} \sim \mathcal{O} \left(\frac{m_b^2}{m_t^2} \right) \approx 10^{-3} \, . \qquad (3.8)$$

This estimate is supported by experimental arguments: Transitions to final states common to B^0 and $\bar{B}^0$ are either Cabibbo suppressed for both B^0 and $\bar{B}^0$, or Cabibbo favoured for one of them but doubly Cabibbo suppressed for the other. As these represent the major contributions to Γ_{12}, the measured branching ratios as well imply $|\Gamma_{12}| \ll |M_{12}|$.

Now, as $|\Gamma_{12}| \ll |M_{12}|$, the equations for the differences in mass Δm and decay width $\Delta\Gamma$ can be developed in taylor series, leading to the approximations

$$\Delta m = 2 |M_{12}| \qquad \left(1 - \frac{1}{8} \frac{|\Gamma_{12}|^2}{|M_{12}|^2} \sin^2\phi \right) \approx 2 |M_{12}| ,$$

$$\Delta\Gamma = 2 |\Gamma_{12}| \cos\phi \quad \left(1 + \frac{1}{8} \frac{|\Gamma_{12}|^2}{|M_{12}|^2} \sin^2\phi \right) \approx 2 |\Gamma_{12}| \cos\phi, \qquad (3.9)$$

where $\phi = \arg(-M_{12}/\Gamma_{12})$. Though, as both $|M_{12}|$ and $|\Gamma_{12}|$ depend on bag parameters and the weak decay constant which cannot be reliably calculated, measurements of Δm only weakly constrain the CKM matrix elements $V_{td}^* V_{tb}$. However, one learns that

$$|\Delta\Gamma| \sim \mathcal{O}(10^{-3}) \, |\Delta m| \ll \Delta m \, . \qquad (3.10)$$

Plugging in the experimental value for $\Delta m \approx 0.5 \, \hbar/\text{ps}$, a partial decay width difference of $|\Delta\Gamma/\Gamma| \sim \mathcal{O}(10^{-3})$, where values of $\approx 4 \cdot 10^{-3}$ are found in more detailed calculations [53, 54].

Another implication of $|\Gamma_{12}| \ll |M_{12}|$ follows for q/p, as it turns out to be dominated by M_{12}. All hadronic parameters cancel, and hence

$$\frac{q}{p} = \sqrt{\frac{M_{12}^* - \frac{i}{2}\Gamma_{12}^*}{M_{12} - \frac{i}{2}\Gamma_{12}}} \approx \frac{M_{12}^*}{M_{12}} = \frac{V_{tb}^* V_{td}}{V_{tb} V_{td}^*} \, . \qquad (3.11)$$

Thus, q/p is a pure phase. This finding is in good agreement with the experimental results for indirect *CP* violation in the mixing, $|q/p| \approx 1$, see Sec. 2.4.2.

3.3 $B^0 \to J/\psi K_S^0$ decay topologies

The decay of B^0 and $\overline{B}^0$ mesons into the $J/\psi K_S^0$ final state is characterised by the decay amplitudes

$$\overline{A}_{J/\psi K_S^0} = \langle J/\psi K_S^0 | \mathcal{T} | \overline{B}^0 \rangle , \quad A_{J/\psi K_S^0} = \langle J/\psi K_S^0 | \mathcal{T} | B^0 \rangle , \tag{3.12}$$

where $\mathcal{T}$ is the transition matrix of the decay. Although the final state $J/\psi K_S^0$ is common to both B^0 and $\overline{B}^0$, it can only be reached by a decay of the B^0 ($\overline{B}^0$) meson into the $J/\psi K^0$ ($J/\psi \overline{K}^0$) final state and the subsequent transition of the flavour eigenstate K^0 ($\overline{K}^0$) into the mass eigenstate K_S^0. The K_S^0 state is a superposition of K^0 and $\overline{K}^0$,

$$|K_S^0\rangle = p_K |K^0\rangle - q_K |\overline{K}^0\rangle . \tag{3.13}$$

The K^0–$\overline{K}^0$ mixing parameters q_K/p_K can be expressed through the involved CKM matrix elements of the box diagrams of $\overline{s}d \to s\overline{d}$ transitions. The interplay of CKM matrix elements and Inami-Lim functions leads to a dominant charm contribution, so that the mixing parameters for the neutral kaon system are given as

$$\frac{q_K}{p_K} = -\frac{V_{cs}^* V_{cd}}{V_{cs} V_{cd}^*} , \tag{3.14}$$

while neglecting CP violation in the mixing, as it is expected to be small, $|q_K/p_K| - 1 = \mathcal{O}(10^{-3})$. The decay amplitudes can be rewritten as

$$\langle J/\psi K_S^0 | \mathcal{T} | B^0 \rangle = +\frac{1}{2p_K} \langle J/\psi K^0 | \mathcal{T} | B^0 \rangle , \tag{3.15a}$$

$$\langle J/\psi K_S^0 | \mathcal{T} | \overline{B}^0 \rangle = -\frac{1}{2q_K} \langle J/\psi \overline{K}^0 | \mathcal{T} | \overline{B}^0 \rangle . \tag{3.15b}$$

Decays of B^0 mesons into the $J/\psi K^0$ final state are mediated through the quark transition $b \to c\overline{c}s$. Contributions from both tree level and penguin diagrams are expected, as shown in Fig. 3.3. Taking care of these contributions leads to a decay amplitude of

$$A(B^0 \to J/\psi K^0) = V_{cs} V_{cb}^* T_c + V_{us} V_{ub}^* P_u + V_{cs} V_{cb}^* P_c + V_{ts} V_{tb}^* P_t, \tag{3.16}$$

where T_c and P_q denote the CP conserving amplitudes of the tree process and the penguin topologies with internal q quarks in the loop, respectively [55–57]. By using the CKM unitarity relations, the definitions of the CKM angle γ and the triangle side R_u, and after defining $P_{q_1 q_2} = P_{q_1} - P_{q_2}$, the amplitude can be rewritten as

$$\begin{aligned}
A(B^0 \to J/\psi K^0) &= V_{cs} V_{cb}^* \left[T_c + P_c - P_t \right] + V_{us} V_{ub}^* \left[P_u - P_t \right] \\
&= V_{cs} V_{cb}^* \left[T_c + P_c - P_t \right] \left(1 + \frac{V_{us} V_{ub}^*}{V_{cs} V_{cb}^*} \left[\frac{P_u - P_t}{T_c + P_c - P_t} \right] \right) \\
&= V_{cs} V_{cb}^* \left[T_c + P_{ct} \right] \left(1 - \frac{V_{us} V_{cd}}{V_{cs} V_{ud}} R_u e^{i\gamma} \left[\frac{P_{ut}}{T_c + P_{ct}} \right] \right) \\
&\overset{\text{W.-st.}}{\approx} \left(1 - \frac{\lambda^2}{2} \right) A\lambda^2 \left[T_c + P_{ct} \right] \left(1 + \frac{\lambda^2}{1 - \lambda^2} R_u e^{i\gamma} \left[\frac{P_{ut}}{T_c + P_{ct}} \right] \right),
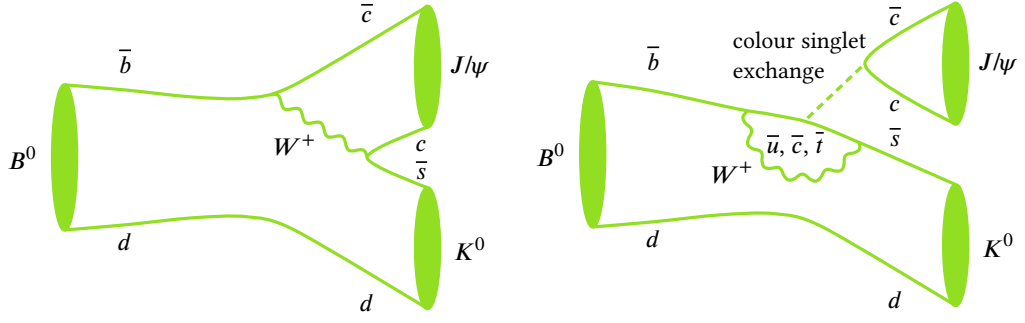\end{aligned} \tag{3.17}$$

Fig. 3.3: Relevant decay topologies of $B^0 \to J/\psi K_S^0$ decays at lowest order. The left diagram represents the dominant, colour-supressed tree diagram, the right diagrams represent the loop suppressed penguin diagrams.

where the Wolfenstein parametrisation up to terms of $\mathcal{O}(\lambda^2)$ is used in the last step. Defining the short-hand notations

$$\mathcal{A} = \lambda^2 A \left[T_c + P_{ct} \right] , \quad \epsilon = \frac{\lambda^2}{1 - \lambda^2} , \quad a \mathrm{e}^{\mathrm{i}\theta} = R_u \left[\frac{P_{ut}}{T_c + P_{ct}} \right] , \tag{3.18}$$

the amplitudes can be simply rewritten as

$$A(B^0 \to J/\psi K^0) = \left(1 - \frac{\lambda^2}{2} \right) \mathcal{A}(1 + \epsilon a \mathrm{e}^{\mathrm{i}\theta} \mathrm{e}^{+\mathrm{i}\gamma}) ,$$
$$A(\bar{B}^0 \to J/\psi \bar{K}^0) = \left(1 - \frac{\lambda^2}{2} \right) \mathcal{A}(1 + \epsilon a \mathrm{e}^{\mathrm{i}\theta} \mathrm{e}^{-\mathrm{i}\gamma}) , \tag{3.19}$$

where a CP transformation is used to arrive at $A(\bar{B}^0 \to J/\psi \bar{K}^0)$ and resulting spurious CP phases have been omitted.

For the further discussion of CP violation, it is important to examine the resulting decay amplitude ratio, which enters $\lambda_{J/\psi K_S^0}$,

$$\frac{\overline{A}_{J/\psi K_S^0}}{A_{J/\psi K_S^0}} = (-1)^l \frac{\langle J/\psi K_S^0 | \mathcal{T} | \bar{B}^0 \rangle}{\langle J/\psi K_S^0 | \mathcal{T} | B^0 \rangle} = \frac{p_K}{q_K} \frac{A(\bar{B}^0 \to J/\psi \bar{K}^0)}{A(B^0 \to J/\psi K^0)} . \tag{3.20}$$

As stated before, the decay of the B^0 meson (pseudoscalar) into a J/ψ meson (vector) and a K_S^0 meson (pseudoscalar) requires an additional angular momentum $l = 1$ in the final state. This has been used in the last transformation. Inserting the findings from Eqs. (3.14), (3.17) and (3.19), the ratio of decay amplitudes can now be written as

$$\frac{\overline{A}_{J/\psi K_S^0}}{A_{J/\psi K_S^0}} = -\frac{V_{cs} V_{cd}^*}{V_{cs}^* V_{cd}} \frac{V_{cb} V_{cs}^*}{V_{cb}^* V_{cs}} \frac{1 + \epsilon a \mathrm{e}^{\mathrm{i}\theta} \mathrm{e}^{-\mathrm{i}\gamma}}{1 + \epsilon a \mathrm{e}^{\mathrm{i}\theta} \mathrm{e}^{+\mathrm{i}\gamma}} . \tag{3.21}$$

It is important to stress that $a \mathrm{e}^{\mathrm{i}\theta}$ is a CP conserving, hadronic term, while $\mathrm{e}^{\mathrm{i}\gamma}$ introduces a weak phase, and therefore give rise to direct CP violation. In particular, the term $a \mathrm{e}^{\mathrm{i}\theta}$ contains

hadronic components which are only weakly constrained by theory and could in principle lead to a considerable enhancement of *CP* violation in the decay. The degree of enhancement is associated to the amount of "penguin pollution", i.e. the ratio of the loop-suppressed penguin diagrams that introduce additional weak phases to the colour-suppressed tree diagram.

Theoretical estimates of the ratio of the dominant penguin diagram P_t to the tree diagram T_c lead to values of $\mathcal{O}(\lambda^2)$, while other calculations find values much closer to $\mathcal{O}(\lambda)$ [58, 59]. However, looking at the CKM related parameters in the decay amplitudes, with values of $\lambda \approx 0.225$, $A \approx 0.8$, $R_u = 0.42$, and especially $\epsilon \approx 0.05$ [31], the additional weak phase from the penguin diagrams is strongly suppressed and can usually be neglected.

3.4 *CP* violation in $B^0 \to J/\psi K_S^0$ decays

As shown in the previous sections, various types of *CP* violation could in principle arise in the interplay of decay and mixing in $B^0 \to J/\psi K_S^0$ transitions. However, indirect *CP* violation in B^0–$\overline{B}^0$ mixing is experimentally excluded at a high precision, and thus $|q/p| = 1$. Penguin pollution could lead to direct *CP* violation in the decay, but is expected to be small, as $|\overline{A}_{J/\psi K_S^0}/A_{J/\psi K_S^0}| \approx 1$. In contrast, a large *CP* violation in the interference of mixing and decay is expected, leading to a measurable decay time dependent asymmetry, as explained in Ch. 2. This type of *CP* violation is characterised by $\mathrm{Im}\,\lambda_{J/\psi K_S^0} \neq 0$. Hence, the relevant parameter for this type of *CP* violation is

$$\lambda_{J/\psi K_S^0} = \frac{q}{p} \frac{\overline{A}_{J/\psi K_S^0}}{A_{J/\psi K_S^0}} = -\frac{V_{tb}^* V_{td}}{V_{tb} V_{td}^*} \frac{V_{cs} V_{cd}^*}{V_{cs}^* V_{cd}} \frac{V_{cb} V_{cs}^*}{V_{cb}^* V_{cs}} \frac{1 + \epsilon a e^{i\theta} e^{-i\gamma}}{1 + \epsilon a e^{i\theta} e^{+i\gamma}}. \tag{3.22}$$

Penguin contributions can be neglected to an approximation that is better than 1% [31], leading to

$$\lambda_{J/\psi K_S^0} \approx -\frac{V_{tb}^* V_{td}}{V_{tb} V_{td}^*} \frac{V_{cs} V_{cd}^*}{V_{cs}^* V_{cd}} \frac{V_{cb} V_{cs}^*}{V_{cb}^* V_{cs}} = -\frac{V_{tb}^* V_{td}}{V_{tb} V_{td}^*} \frac{V_{cb} V_{cd}^*}{V_{cb}^* V_{cd}}, \tag{3.23}$$

and

$$\mathrm{Im}\,\lambda_{J/\psi K_S^0} = \sin\left[\arg\left(-\frac{V_{tb}^* V_{td}}{V_{tb} V_{td}^*} \frac{V_{cb} V_{cd}^*}{V_{cb}^* V_{cd}}\right)\right] = \sin\left[2\arg\left(-\frac{V_{cb}^* V_{cd}}{V_{tb} V_{td}^*}\right)\right] = \sin 2\beta, \tag{3.24}$$

with the CKM angle β as defined in Ch. 1, Eq. (1.10). In the B^0 system, the decay width difference is found to be small, $\Delta\Gamma/\Gamma < 1\%$ [60, 61], and hence, the time-dependent decay rates defined in Ch. 2, Eq. (2.24) simplify to

$$\Gamma(B^0(t) \to J/\psi K_S^0) = \frac{\tilde{A}}{2} e^{-\Gamma t}\left(1 + C_{J/\psi K_S^0} \cos \Delta m t - S_{J/\psi K_S^0} \sin \Delta m t\right), \tag{3.25a}$$

$$\Gamma(\overline{B}^0(t) \to J/\psi K_S^0) = \frac{\tilde{A}}{2} e^{-\Gamma t}\left(1 - C_{J/\psi K_S^0} \cos \Delta m t + S_{J/\psi K_S^0} \sin \Delta m t\right), \tag{3.25b}$$

with the parameter $\tilde{A} = |A_{J/\psi K_S^0}|^2 (1 + |\lambda_{J/\psi K_S^0}|^2)$ and the *CP* observables

$$C_{J/\psi K_S^0} = \frac{1 - |\lambda_{J/\psi K_S^0}|^2}{1 + |\lambda_{J/\psi K_S^0}|^2} = 0, \qquad S_{J/\psi K_S^0} = \frac{2\,\mathrm{Im}\,\lambda_{J/\psi K_S^0}}{1 + |\lambda_{J/\psi K_S^0}|^2} = \sin 2\beta. \tag{3.26}$$

As $\Delta \Gamma = 0$ has been assumed, the third *CP* parameter, $D_{J/\psi K_S^0} = \cos 2\beta$, is ignored in the description of the time dependent rates. Thus, one arrives at the time-dependent asymmetry

$$\mathcal{A}_{J/\psi K_S^0} = \frac{\Gamma(\overline{B}^0(t) \rightarrow J/\psi K_S^0) - \Gamma(B^0(t) \rightarrow J/\psi K_S^0)}{\Gamma(\overline{B}^0(t) \rightarrow J/\psi K_S^0) + \Gamma(B^0(t) \rightarrow J/\psi K_S^0)} \tag{3.27}$$
$$= S_{J/\psi K_S^0} \sin \Delta mt - C_{J/\psi K_S^0} \cos \Delta mt = \sin 2\beta \, \sin \Delta mt \,.$$

Hence, to a very high precision, the extent of the decay rate asymmetry in the $B^0 \rightarrow J/\psi K_S^0$ channel gives direct access to the CKM angle β of the Standard Model. Its quark level $b \rightarrow c\overline{c}s$ transition provide a clean measurement of the CKM angle, as penguin contributions are expected to be negligible. Moreover, its decay products, J/ψ and K_S^0, are easy to reconstruct through the $J/\psi \rightarrow \mu^+ \mu^-$ and the $K_S^0 \rightarrow \pi^+ \pi^-$ decays, each with two charged daughters in the final state. For all of these reasons, $B^0 \rightarrow J/\psi K_S^0$ has been termed the gold-plated decay channel for *CP* violation in the B^0 meson system.

3.5 New Physics vs. theoretical uncertainties

By measuring $S_{J/\psi K_S^0}$ and comparing it to the expectations for $\sin 2\beta$, using the constraints of the CKM mechanism and other measurements, the validity of the Standard Model description of weak quark transitions and *CP* violation can be examined. Discrepancies in the CKM picture could either be a hint for New Physics, or indicate a lack of understanding for higher order Standard Model effects.

New Physics, i.e. particles and couplings not described by the Standard Model of particle physics, could contribute to the loops of the mixing and penguin diagrams. By introducing additional complex couplings, it could lead to *CP* asymmetries that differ from the Standard Model expectations. In the presence of New Physics in the $B^0 \rightarrow J/\psi K_S^0$ mode, the largest effects would be expected from the mixing diagrams, leading to an additional phase ϕ_{NP} and hence to

$$S_{J/\psi K_S^0} = \sin(\phi_d + \phi_{\mathrm{NP}}), \tag{3.28}$$

where $\phi_d = 2\beta$ represents the SM expectation for negligible indirect and direct *CP* violation.

In view of the search for New Physics, and with the increasing experimental precision of *CP* measurements in $B^0 \rightarrow J/\psi K_S^0$, a stronger effort in controlling higher order Standard Model effects from a theoretical point of view is needed. Ignoring such effects could lead to an under- or overestimation of the mixing phase and hereby fake a consistency or inconsistency of the Standard Model's CKM picture.

In the former sections, some simplifying assumptions have been made. First, it was assumed that *CP* violation in the mixing can be ignored. In the SM, this holds true at a level of 10^{-4}. Second, penguin pollution leading to direct *CP* violation has been declared small. In fact, enhancements in $S_{J/\psi K_S^0}$ of up to 0.02 can be expected [57, 62], which is just slightly below the experimental uncertainties. Third, terms that arise for $\Delta \Gamma \neq 0$ have been ignored, although $\Delta \Gamma \approx \mathcal{O}(10^{-3})$. Including $\Delta \Gamma$ would lead to additional terms in the time dependent decay rates, one of them proportional to $\cos 2\beta$. Fourth, *CP* violation in neutral kaon mixing has been ignored as well. Hence, when the experimental precision for $S_{J/\psi K_S^0}$ reaches ≈ 0.005,

most of these effects need to be better understood and included. Otherwise, they would contribute as major systematic uncertainties to the evaluation of $\sin 2\beta$.

3.6 Experimental status

The decay $B^0 \to J/\psi K_S^0$ has been extensively used for the measurement of $\sin 2\beta$, or more precisely, of $S_{J/\psi K_S^0}$ and $C_{J/\psi K_S^0}$. Although $B^0 \to J/\psi K_S^0$ is theoretically and experimentally clean, other B^0 decay channels with $b \to c\bar{c}s$ transitions to CP eigenstates, like $B^0 \to J/\psi K_L^0$, $B^0 \to \chi_{c,0} K_S^0$, or $B^0 \to \psi(2S) K_S^0$, give access to $S_{b\to c\bar{c}s} = -\eta_f \sin(2\beta)$ and $C_{b\to c\bar{c}s}$ as well, where η_f is the CP eigenvalue of the final state.

The resulting world averages [12] of all measurements are

$$S_{b\to c\bar{c}s} = 0.679 \pm 0.020 \,, \qquad C_{b\to c\bar{c}s} = 0.005 \pm 0.017 \,,$$

where the most precise inputs are obtained from the averaged results of measurements in the $B^0 \to J/\psi K_S^0$ decay mode,

$$S_{J/\psi K_S^0} = 0.665 \pm 0.024 \,, \qquad C_{J/\psi K_S^0} = 0.024 \pm 0.026 \,.$$

As mentioned before, these averages are dominated by the measurements of the Belle [63] and BaBar [64] experiments, which find

$$S_{J/\psi K_S^0}^{\mathrm{BaBar}} = 0.657 \pm 0.036 \,(\mathrm{stat.}) \pm 0.012 \,(\mathrm{syst.}) \,,$$
$$S_{J/\psi K_S^0}^{\mathrm{Belle}} = 0.670 \pm 0.029 \,(\mathrm{stat.}) \pm 0.013 \,(\mathrm{syst.}) \,,$$

for the parameter of interference CP violation and

$$C_{J/\psi K_S^0}^{\mathrm{BaBar}} = 0.026 \pm 0.025 \,(\mathrm{stat.}) \pm 0.016 \,(\mathrm{syst.}) \,,$$
$$C_{J/\psi K_S^0}^{\mathrm{Belle}} = 0.015 \pm 0.021 \,(\mathrm{stat.}) \pm_{0.045}^{0.023} \,(\mathrm{syst.}) \,,$$

for the parameter of CP violation in mixing or decay. Other measurements in this decay channel have been performed by the ALEPH, OPAL, and CDF collaborations, and are in good agreement with the world average.

These results constrain the CKM $(\bar{\rho}, \bar{\eta})$-plane at a high precision. Adding them into the overall CKM picture, and using various other measurements and inputs, as done in the global fits by the CKMFitter [38] and UTFit [65] groups, a remarkable overall agreement is observed. Yet, a small tension between the measured branching ratio of $B \to \tau\nu_\tau$ and the measured $\sin 2\beta$ value remains, see Fig. 3.4, however well within statistical expectations. Even with further increase of experimental precision, this tiny tension leaves only little room for large New Physics effects in quark transitions. Until now, no obvious signs of New Physics effects beyond the physics described by the Standard Model have been observed in direct measurements either. Hence, if New Physics is present, its effects seem to be small, and even more precise measurements are needed to pin it down. With forthcoming luminosity
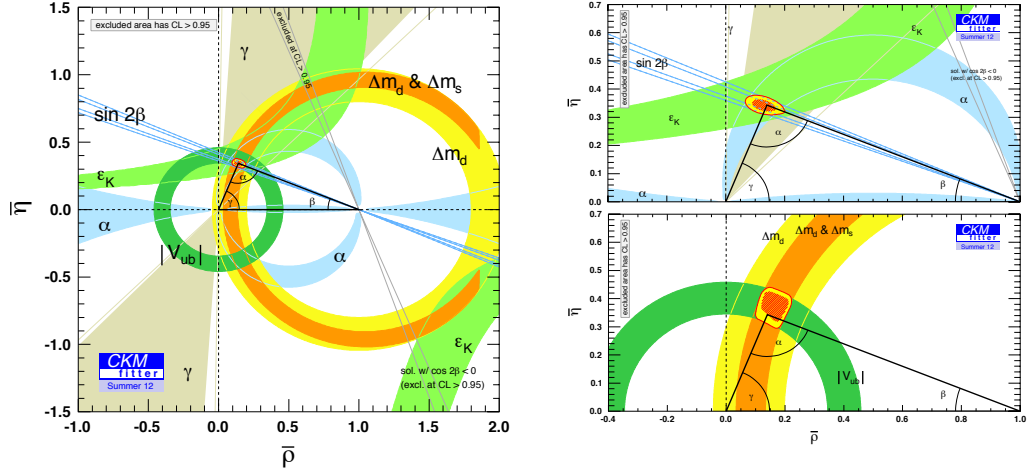
Fig. 3.4: Left: Result of a global fit to measured observables of the CKM sector, as provided by the CKMfitter group [38]. The coloured bands show the various constraints in the $(\bar{\rho}, \bar{\eta})$-plane. The red hashed region corresponds to 68% CL. Right: The upper plot shows constraints from *CP* violating quantities ($\sin 2\beta$, α, γ, and ε_K), while the lower plot shows the constraints from *CP* conserving quantities ($|V_{ub}/V_{cb}|$, Δm_d, Δm_s, and $B^+ \to \tau^+ \nu_\tau$). While the depicted triangle is the result of the global fit, the red hashed region is gained by only including the particular constraints. A small tension between the world averages for $\sin 2\beta$ and $\mathcal{B}(B^+ \to \tau^+ \nu_\tau)$ is observed at the level of approximately 1.5σ.

gains, LHCb should be able to compete with the most precise measurements of $S_{J/\psi K^0_S}$ and contribute to this search.

Apart from that, $S_{J/\psi K^0_S}$ right now is the most precisely determined *CP* violating observable in the *B* system, with theoretical uncertainties that are still negligible at the current experimental precision. Hereby, it represents the benchmark channel for measurements of time-dependent *CP* violation in the *B* meson sector. This holds especially for the physics program of the LHCb experiment, where key analyses are concerned with measurements of time-dependent *CP* violation in the B^0_s sector.

4 The LHCb Experiment

The Large Hadron Collider beauty (LHCb) experiment is one of the experiments at the Large Hadron Collider (LHC) at the European Organization for Nuclear Science, CERN, in Geneva, Switzerland. In contrast to the two large multi-purpose LHC experiments – ATLAS and CMS – LHCb seeks for New Physics effects through indirect searches, i.e. high precision measurements in decays of *b* and *c* hadrons. Hereby, LHCb's main focus lies on measurements of potentially *CP* violating or rare decay modes of *b* and *c* hadrons, in which small New Physics contributions could lead to major deviations from the Standard Model expectations.

LHCb's physics program requires a high-yield sample of *b* and *c* hadrons, provided by the proton collisions of the LHC, as well as a detector that can reconstruct the hadrons' decays and distinguish between different final states, especially between kaons, pions, and muons. Further, many of LHCb's physics analyses depend on the knowledge of the decay time of each reconstructed *b* hadron. This demands for excellent spatial measurements of the meson's production and decay vertices.

After a short introduction to the LHC and its other experiments, this chapter focuses on the description of the LHCb experiment, and more specifically its detector, trigger systems, software, and running conditions in 2011.

4.1 The Large Hadron Collider

The Large Hadron Collider (LHC) is the world's largest and highest-energy particle accelerator and collider [66]. It is installed in a 26.7 km long circular tunnel located 50 to 175 m below ground, near the Franco-Swiss border in the vicinity of Geneva. It reuses the tunnel of its predecessor LEP – the Large Electron–Positron Collider – which was dedicated to high precision measurements of electroweak processes, and stopped service in 2000. In contrast to LEP, LHC is designed as a discovery machine. It collides two oppositely travelling beams of protons at a centre-of-mass energy of up to $\sqrt{s} = 14\,\mathrm{TeV}$ at four interaction points, each instrumented with large detectors. The choice of proton beams allows for a vast field of possible measurements at an unprecedented energy, while keeping synchrotron losses to a minimum. On the downside, it comes with high particle multiplicities, which are a result of the hadronic nature of the collisions, hereby challenging the experimental setups.

4.1.1 The accelerator and collider

In the LHC, oppositely running beams of protons are accelerated from 450 GeV up to 7 TeV energy, while being held in the LHC beam pipes by 1232 superconducting NbTi dipole magnets and additional support magnets. The superconducting magnets are cooled with liquid helium,

requiring a huge cryogenics system and an advanced protection system against magnet quenches.

To arrive at the initial beam energy of 450 GeV, LHC relies on a chain of pre-accelerators: the Linear Accelerator 2 (LINAC2), the PS Booster (PSB), the Proton Synchrotron (PS), and the Super Proton Synchrotron (SPS), as shown in Fig. 4.1. In nominal running conditions, SPS
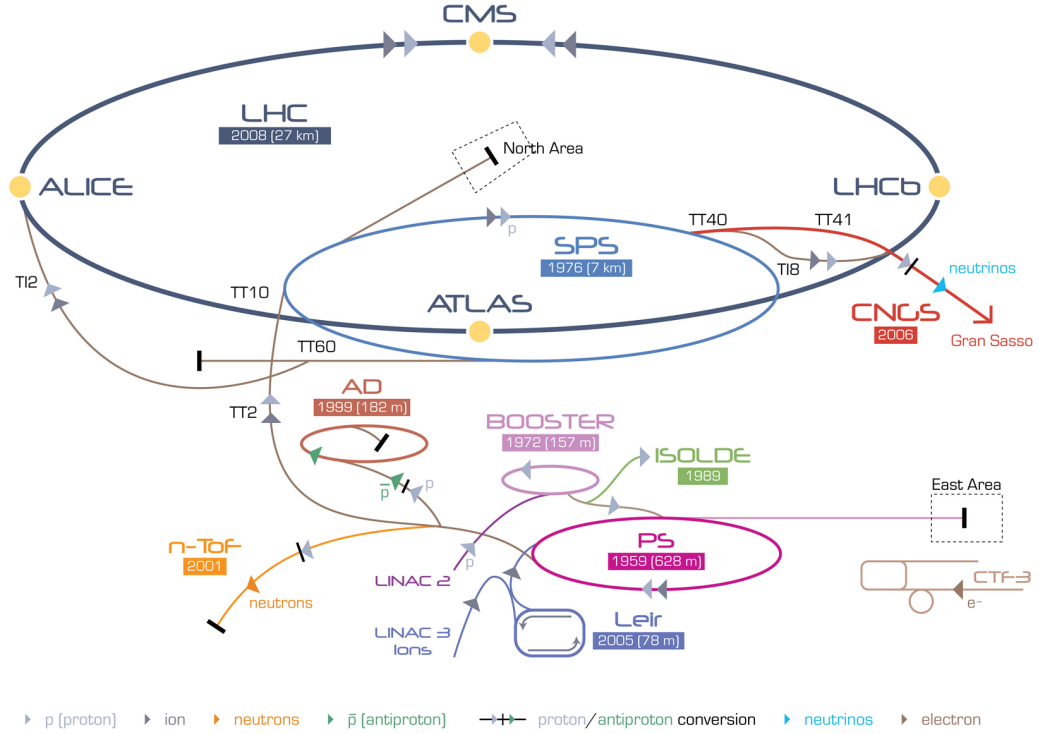

Fig. 4.1: Schematic view of CERN's accelerator complex [67]. The pre-accelerator chain for the LHC consists of the Linear Accelerator 2 (LINAC2), the Proton Synchrotron Booster (PSB), the Proton Synchrotron (PS), and the Super Proton Synchrotron (SPS). For ion-ion fills, LINAC2 and PSB are substituted by LINAC3 and the Low Energy Ion Ring (LEIR). Other CERN facilities that use parts of the LHC pre-accelerator chain are the Antiproton Decelerator (AD), the CLIC Test Facility (CTF3), the Cern Neutrinos for Gran Sasso (CNGS), the Isotope Separator Online Device (ISOLDE), and the Neutrons Time of Flight (n-ToF).

provides the LHC with proton beams with an energy of 450 GeV. These beams are delivered in several bunch trains, each with up to 4 batches of 72 bunches at a bunch spacing of 25 ns and with a bunch intensity of $1.15 \cdot 10^{11}$ protons. In the LHC, these sum up to proton beams with up to 2808 bunches per beam, that collide at four interaction points at a rate of 40 MHz, and lead to a design luminosity of up to 10^{34} cm^{-2} s^{-1} and a mean *pp* interaction rate of about 20 per bunch-crossing.

In September 2008, the LHC circulated proton beams for the first time at the injection energy of 450 GeV. Shortly after this success, in preparation of the nominal magnet conditions for 7 TeV beam energy, a major construction fault in the bus bar interconnects between the dipole magnets led to a failure of the quench protection system. It caused severe damages

in a number of magnets, and operation could not be continued until late 2009. After an assessment of the construction fault, it was decided to limit the beam energy to 4 TeV until a long shutdown period in 2012–2014 would allow for an exchange of the faulty connectors.

Following the recovery, first proton collisions at $\sqrt{s} = 7$ TeV were recorded in March 2010. This centre-of-mass energy was chosen throughout the 2010 and 2011 runs, and was raised to 8 TeV in 2012. It was decided to use a 50 ns bunch spacing to improve beam stability instead of the design 25 ns spacing [68]. To compensate for the resulting effective loss in luminosity, the bunch intensities were raised to $1.5 \cdot 10^{11}$ protons in June 2012, about 30% above the nominal design. This lead to a peak instantaneous luminosity of $6.8 \cdot 10^{33}$ cm^{-2} s^{-1}, in good agreement with the target design luminosity at 7 TeV centre-of-mass energy.

4.1.2 The experiments

The LHCb experiment is one of the four major experiments, out of a total of seven experiments at the LHC. The largest of these experiments are ATLAS (A Toroidal LHC Apparatus) [69] and CMS (Compact Muon Solenoid) [70], two general-purpose detectors. Both of them target a large research field, where the search for and investigation of the last missing Standard Model particle, the Higgs boson, and the search for dark matter candidates, extra dimensions, and supersymmetric partners of the Standard Model particles account for the largest share of the physics program. As both experiments, to a large extent, cover the same physics program, results of each can be easily cross-checked by the other.

ALICE (A Large Ion Collider Experiment) [71] makes use of LHC's capabilities to collide bunches of heavy ions, either in Pb-Pb or Pb-*p* runs. Its aim is the study of strongly interacting matter at extreme energy densities. Especially the quark-gluon plasma, a state of matter that could form at high temperatures and densities, is in the focus of the ALICE group.

The smallest experiments at the LHC, TOTEM (Total elastic and diffractive cross-section measurement) [72] and LHCf (Large Hadron Collider forward) [73], operate in the extreme forward region of collisions, and hereby complement the general-purpose detectors. The TOTEM detectors are installed around the CMS interaction point and are used to measure the *pp* interaction cross-section. LHCf, which is installed near the beam-pipe, 140 m on either side of the ATLAS detector, uses the forward particle remnants of the LHC collisions in ATLAS as cosmic ray simulations. Its goal is the development of better models for the interaction of cosmic rays with the atmosphere.

MoEDAL (Monopole and Exotics Detector at the LHC) [74] is dedicated to the direct search for magnetic monopoles, i.e. particles with a magnetic charge, and for highly ionizing stable massive particles. It consists of an array of 400 modules of plastic nuclear-track detectors, installed around the LHCb interaction point, without interfering with the LHCb detector.

4.2 Production of *b* hadrons at the LHC

The unprecedented collision energies and rates of the LHC make it a high-yield factory for *b* hadrons. At a centre-of-mass energy of $\sqrt{s} = 7$ TeV, the production cross-section for $b\bar{b}$-pairs has been measured as $\sigma(pp \rightarrow b\bar{b}X) = 284 \pm 20 \pm 49\,\mu$b by LHCb, which corresponds to

$\mathcal{O}(3‰)$ of the total *pp* cross-section [75]. At $\sqrt{s} = 14\,\text{TeV}$, the $b\bar{b}$ production cross-section is expected to rise to approximately $500\,\mu\text{b}$.

Multiple processes account for the production of *b* quarks, where gluon fusion is the most dominant process at the LHC. Here, two gluons create a $b\bar{b}$ pair. At the energies of *pp* collisions at the LHC, a high momentum asymmetry between the two gluons is probable, leading to a large momentum of the $b\bar{b}$ pair system and therefore to a strong boost along the beam axis. Hence, both quarks of the $b\bar{b}$ pair have a high probability of being produced along the beam axis, as shown in Fig. 4.2. Single *b* quark production, e.g. via flavour excitation processes, represents a much smaller fraction of the *b* cross-section [31].
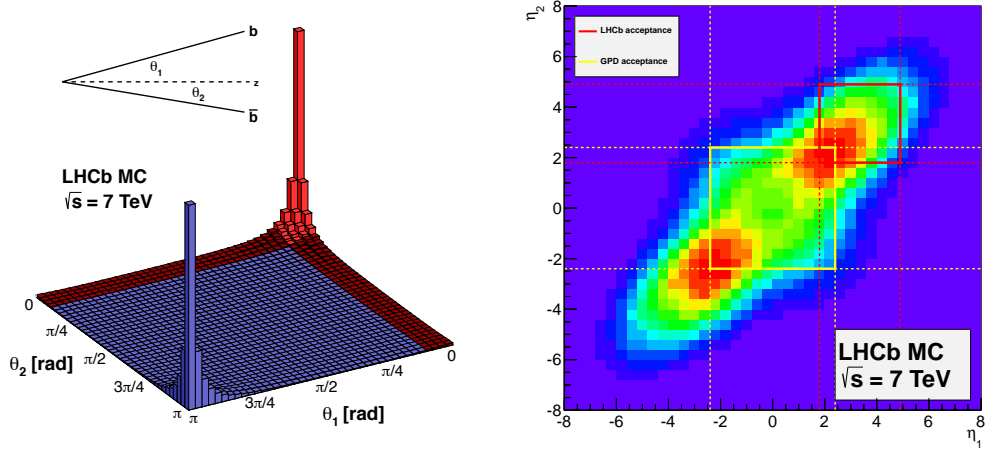

Fig. 4.2: Kinematically correlated production of $b\bar{b}$ quark pairs, as expected from simulations. Left: Plot of the correlation of polar angles of each of the two *b* quarks in *pp* collisions at $\sqrt{s} = 7\,\text{TeV}$. The red region represents the LHCb geometric acceptance. Right: Correlation of pseudo-rapidities of the two *b* quarks. The colour code represents the frequency of a certain pseudo-rapidity occurrence, reaching from blue (low frequency) to red (high frequency) in arbitrary units. The red box represents LHCb's geomteric acceptance, while the yellow box shows the coverage of general purpose detectors like ATLAS and CMS.

Although being produced as a pair, each quark of the $b\bar{b}$ quark pair hadronises separately and incoherently. As LHC's collision energies exceed the typical *b* hadron masses, the full spectrum of *b* hadrons is accessible. The *b* quarks hadronise dominantly into the lightest *b*-flavoured mesons, i.e. B^+/B^- ($\approx 40\%$), $B^0/\bar{B}^0$ ($\approx 40\%$), $B_s^0/\bar{B}_s^0$ ($\approx 10\%$), and in the remaining 10% to heavier *b* mesons and baryons [31]. Though, a measurement by LHCb has found a dependence of the production ratio of the lightest *b*-flavoured baryon, the Λ_b, on its transverse momentum [77], leading to a production ratio of up to 40% with respect to the combined production rates of B^0 and B^+ mesons.

In the former discussion of the production rates of the various *b* flavoured mesons, the inclusion of charge conjugate hadrons has been implied, as the production diagrams for $b/\bar{b}$ quarks are flavour symmetric. Though, as the colliding protons do present an initial state
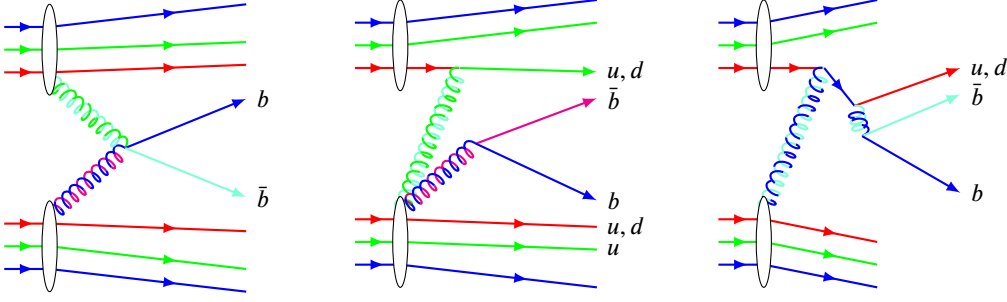
Fig. 4.3: Production processes for *b* hadrons in which the interaction with the proton beams can result in a production asymmetry for *B* mesons. For illustration, quark colour charges are chosen as red, green, and blue, while their respective anti-colours are chosen as cyan, magenta, and yellow. Left: Colour connections between the *b* quark and di-quark remnants of the beam drag it towards the beam, while the $\bar{b}$ quark has colour connections with the quark remnants, also leading to a drag towards the beam. Middle: At low transverse momenta, the $\bar{b}$ quarks can directly hadronise with the beam remnants, favouring production of B^0, B^+, and *b*-Baryons. Right: At high transverse momenta, a scattered valence quark produces a $b\bar{b}$ quark pair through gluon splitting. Thus, the formation of a *b* meson from a $\bar{b}$ and the scattered valence quark is favoured. Figures based on Ref. [76].

with charge and baryon number +2, the hadronisation rates into a hadron and into its charge conjugate are not necessarily the same.

Mainly three effects can lead to a *B* meson production rate asymmetry [78–80]. At low transverse momenta, *b* quarks can combine with the proton valence *u* and *d* quarks to form beauty baryons, hereby lowering the production rate of $\bar{B}^0$, B^-, and $\bar{B}_s^0$ mesons. At the same time, low momentum $\bar{b}$ quarks can form B^0 and B^+ mesons with the valence quarks. Both of these effects lead to an excess of B^0 over $\bar{B}^0$ meson production. At high transverse momenta, $b\bar{b}$ pairs can form hadrons with scattered valence quarks, consequently enhancing the production rate of B^+ and B^0 mesons. The third effect is a result of colour connections of the $b\bar{b}$ quarks with the beam remnants. Colour connections of the $\bar{b}$ quark with quark remnants and colour connections of the *b* quark to di-quark remnants lead to a drag towards the beam. This effect reshuffles *b* and $\bar{b}$ quarks depending on their rapidity (y) and transverse momentum (p_{T}), and can therefore lead to p_{T} and y dependent asymmetries. All three effects are illustrated in Fig. 4.3.

The $B^0/\bar{B}^0$ production asymmetry

$$A_{\mathrm{P}} = \frac{R_{\bar{B}^0} - R_{B^0}}{R_{\bar{B}^0} + R_{B^0}}, \tag{4.1}$$

is described by the relative difference of the production rate $R_{\bar{B}^0}$ for $\bar{B}^0$ mesons and the production rate R_{B^0} for B^0 mesons. Studies with the Lund fragmentation model and the intrinsic heavy quark model predict negligible asymmetries of $< 1\%$ for central rapidities and high transverse momenta [80]. However, in certain regions of phase-space, especially at rapidities $y > 3$ and transverse momenta between 5 and 10 GeV/c, asymmetries of up to 2% can be accommodated for in the models. As these regions overlap with LHCb's acceptance,

the production asymmetries for *b* meson production need to be considered in view of a *CP* asymmetry measurement in $B^0 \rightarrow J/\psi K_S^0$ decays.

4.3 The LHCb spectrometer

The LHCb detector is a single-arm forward spectrometer dedicated to the study of *b*- and *c*-hadron decays. The hadrons originate from the hadronisation of the heavy *c*- and *b*-quarks produced in the *pp* collisions. As these are typically emitted in the high-rapidity range, see Fig. 4.2, a forward spectrometer design allows for the best instrumentation in the region of interest. The LHCb detector is installed in the DELPHI cavern [81] at LHC's IP8 (Interaction Point 8). To optimally exploit the limited space, the LHCb detector instruments the full cavern length of 20 m. A thorough description of the LHCb detector can be found in Ref. [82].
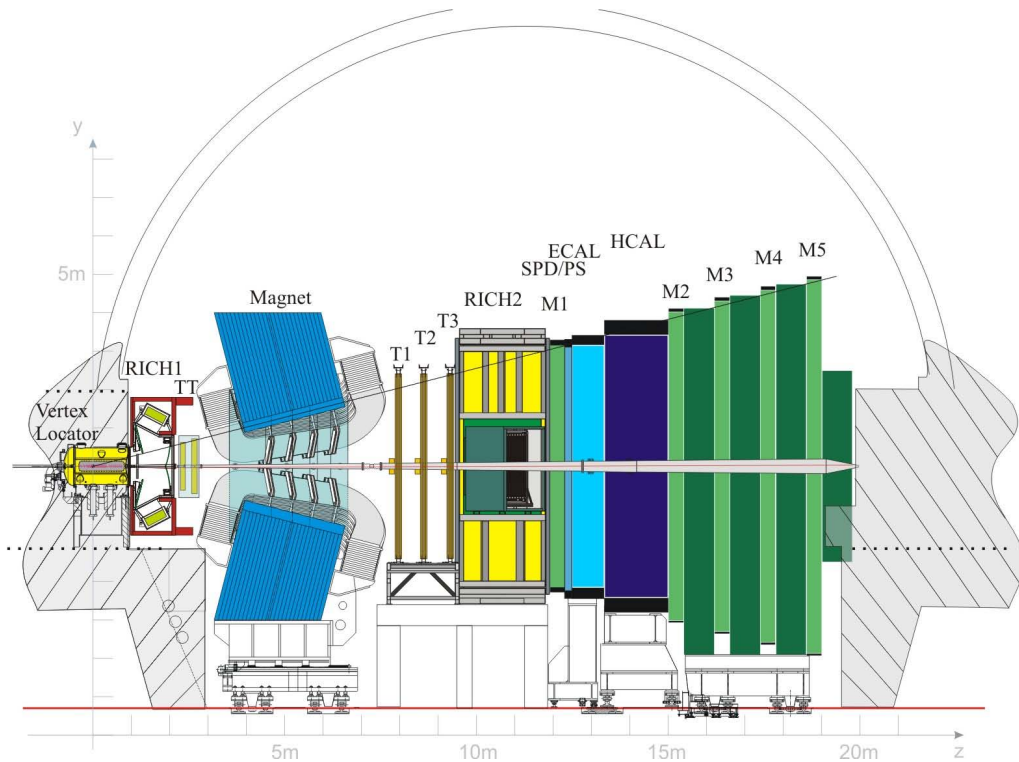
Fig. 4.4: Schematic side-view of the LHCb detector [82]. Starting from the interaction point and proceeding downstream, along the positive *z*-axis, the detector consists of the Vertex Locator (VELO), the Ring Imaging Cherenkov detector (RICH1) for particles with low momenta, the Tracker Turicensis (TT), the dipole magnet, the three tracking stations T1–T3, each consisting of an inner silicon tracker (IT) near the beam axis and an outer tracker (OT), which uses drift-tubes, the second Ring Imaging Cherenkov detector (RICH2) for particles with high momenta, the first muon station (M1), the calorimetry system consisting of a scintillating pad detector (SPD), a Preshower (PS), an electromagnetic calorimeter (ECAL), and a hadronic calorimeter (HCAL), and, at last, the other four muon stations M2–M5.

A schematic side view in Fig. 4.4 shows the experimental layout of LHCb. The right handed coordinate system's z-axis points from the interaction point (IP) at $x = y = z = 0$ into the direction of the detector (downstream), along the travel direction of LHC's beam 1, while the y-axis points upwards and the x-axis points to the centre of the LHC ring. LHCb covers an angular acceptance of 10 to 300 mrad (250 mrad) in the horizontal (vertical) plane. This corresponds to an acceptance of particles with pseudorapidities in the range of 2 to 5. As LHCb is dedicated to the study of particles that are produced with high rapidities, the material budget around the IP is kept to a minimum, hereby reducing the rate of secondary interactions. This design strategy reflects as well in the choice of materials for the beam pipe, which holds the vacuum through which the LHC beams travel within the detector. A beryllium beam pipe is used starting at the Vertex Locator up to the calorimeters, where it is continued by a beam pipe of stainless steel.

For the safety of the detector, several systems monitor the beam losses and related background levels in the LHCb detector. Especially in the beam injection and acceleration phases of LHC, beam instabilities need to be detected as early as possible. The main background detector and beam protection device of LHCb is the Beam Condition Monitor (BCM) [83]. It automatically requests a beam dump if the measured charged particle density in the vicinity of the beam pipe reaches a level that may damage the detector components. An additional system, the Beam Loss Scintillators (BLS), monitors at a high time resolution and is more sensitive at low background rates than the BCM. This allows for additional insight on the source and build-up of background rates even before they reach the BCM dump threshold.

4.3.1 The tracking system

To achieve precision measurements of b hadron decays, LHCb must provide excellent vertexing, tracking, and momentum information in the high-multiplicity environment of a hadron collider. These tasks are fulfilled through the interplay of the Vertex Locator (VELO), a silicon-strip vertex detector surrounding the pp interaction point, the Tracker Turicensis (TT), a large-area silicon-strip detector, LHCb's warm dipole magnet, which offers an integrated magnetic field of 4 T m, and the three downstream tracking stations (T1–T3), consisting of an Inner Tracker (IT) of silicon-strip detectors and an Outer Tracker (OT) of drift-tubes.

Charged particles passing through the sensitive material of the tracking detectors deposit charges which are measured by the sensors. The resulting signals are merged into (x, y, z) positions, the so-called hits, which are used by the reconstruction software to form tracks, representing the best knowledge of the particles' trajectories through the detector. A brief description of the tracking algorithms will be given in Sec. 4.5.1. The track momenta can be deduced from the track curvatures and the magnetic field map. LHCb's tracking system achieves a relative momentum resolution of $\Delta p/p$ that varies from 0.4% for 5 GeV/c tracks to 0.6% for 100 GeV/c tracks. Besides the momentum measurement, tracks are used to extrapolate particle paths to clusters in the calorimeters and Cherenkov rings in the RICH detectors. An example of an LHCb event with reconstructed tracks, Cherenkov cones, and calorimeter clusters is shown in Fig. 4.5.

LHCb's dipole magnet leads to a left-right detection asymmetry for charged particles. As this can bias *CP* measurements, the dipole magnet can be operated with a flipped magnetic field. Hence, throughout the data taking period, the magnet polarity is regularly switched.
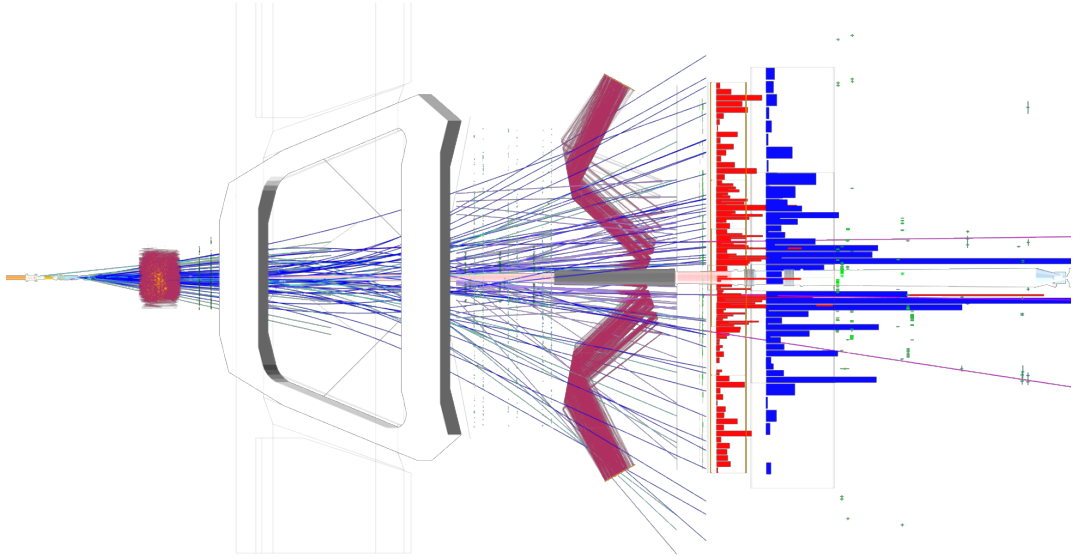

Fig. 4.5: Event display in the xz-plane of an LHCb event with a reconstructed $B_s^0 \to \mu^+\mu^-$ decay. The lines represent the reconstructed tracks, the histograms represent the deposited energy in the calorimeters (ECAL in red, HCAL in blue), and the burgundy lines in the RICH detectors are the extrapolated Cherenkov cones [84].

The Vertex Locator

The Vertex Locator (VELO) surrounds the interaction point and allows tracking within the full detector acceptance. As b hadrons produced in LHCb cover typical flight distances of $\mathcal{O}(\text{mm})$ before decaying, the VELO plays a substantial role in precise measurements of decay times by reconstructing the production and decay vertices. In 2011, the VELO achieved impact parameter resolutions of 20 μm for high transverse momentum tracks (the impact parameter is the perpendicular distance of a track to a vertex).

The VELO follows a cylindrical symmetry: 21 silicon disc stations are installed perpendicular to the beam axis, where 6 of them are located upstream and 15 downstream of the nominal interaction point, as shown in Fig. 4.6. Each disc has a radius of 42 mm and consists of two module halves placed left and right of the beam axis. Each half is instrumented with two types of silicon strip sensors: The r sensors consist of 512 concentric, semicircular strips, with a decreasing strip pitch to smaller radii, and thus allowing for a constant relative impact parameter resolution. The ϕ sensors have quasi-radial strips, which are skewed by 10° in the inner and by 20° in the outer region. The skew angles are reversed in alternating ϕ sensors and thus give a small sensitivity on the r position of the crossing tracks.

The innermost radius of the sensitive area reaches down to 8 mm in extreme proximity to the beam. A radio frequency box separates the VELO modules from the LHC beams. The box is kept in vacuum, making the choice of a thin radio frequency foil possible and hereby significantly reducing the material budget. To reduce any risk of damaging the VELO sensors in unstable LHC phases, e.g. beam injection and acceleration, the VELO half-modules can be retracted to a safe position 3 cm away from the beams. In stable beam conditions, the VELO halves are moved back into an optimal, symmetric position around the beam spot.

The Silicon Trackers and the Outer Tracker

The TT is installed right behind the RICH1 detector, upstream of the magnet, and covers an area of $130 \cdot 160\,\text{cm}^2$ with silicon micro-strip detectors. The silicon wavers are $500\,\mu\text{m}$ thick with a strip pitch of $183\,\mu\text{m}$. It shares its silicon strip technology with the IT, the inner detector of the downstream tracking stations T1–T3. Silicon strips offer a good hit resolution and fast response time in spite of being installed in regions of high track density and radiation levels. The strips are read out by readout hybrids, which are connected by wire-bonded cables to the silicon sensor.

Each of the silicon trackers, IT and TT, consists of four stations, with vertical strips in the first and last "x" layer, and layers rotated by a stereo angle of $+5°$ ($-5°$) degrees in the second (third) "u" ("v") layer. To improve spatial resolution, the TT has a 27 cm gap between the u and v layers, while the IT layers are separated by 4 cm gaps.

The Outer Tracker (OT) is a drift detector that extends the T1–T3 stations to the full LHCb acceptance. The lower track multiplicity in the OT region allows for the use of straw drift tubes. Like TT and IT, the OT consists of four layers in an x-u-v-x configuration to enable tracking information in y. Each layer is composed of densely packed planes of straw drift tubes. The tubes are filled with a gas mixture of 70% Argon, 28.5% CO_2, and 1.5% O_2, allowing for drift-times below 50 ns.

4.3.2 The particle identification system

Decays of b hadrons offer access to a variety of observables, which differ between final states. Hence, an excellent particle identification is mandatory to reconstruct decays into specific final states while keeping the rate of mis-identified particles to a minimum. For instance, reconstructed decays of $B^0 \rightarrow D^- K^+$ could be massively polluted by $B^0 \rightarrow D^- \pi^+$ decays due to poor K-π separation. In LHCb, particle identification is achieved by using two Ring Imaging Cherenkov (RICH) detectors to distinguish charged kaons, pions, and protons, a calorimetry system to identify photons, electrons, and hadrons, and a muon system to identify muons.

The RICH detectors

LHCb is instrumented with two Ring Imaging Cherenkov (RICH) detectors that make use of three different radiators covering the full detector acceptance and a large range of particle momenta. The RICH detectors exploit the Cherenkov effect [85, 86]: A charged particle traversing a dielectric with refractive index n at a speed v larger than the phase speed c' of

light in the medium, $c' = c/n$, creates a net dipole which continuously radiates photons in a cone along the particle's path. The photon emission angle, the Cherenkov angle θ_C, is given by

$$\cos\theta_C = \frac{1}{n\beta} \quad \text{with } \beta = v/c. \tag{4.2}$$

In the RICH detectors, spherical mirrors image the Cherenkov photons into a single ring at the mirror's characteristic focal length. To reduce the material budget within the detector acceptance, additional flat mirrors guide the radiated photons onto hybrid photon detectors (HPDs), where they are detected. By measuring the ring radius, the Cherenkov angle θ_C, and hence β, can be determined. Combined with the momentum measurement from the tracking, different mass hypotheses can be tested. An example of reconstructed Cherenkov rings in RICH1 is shown in Fig. 4.6.
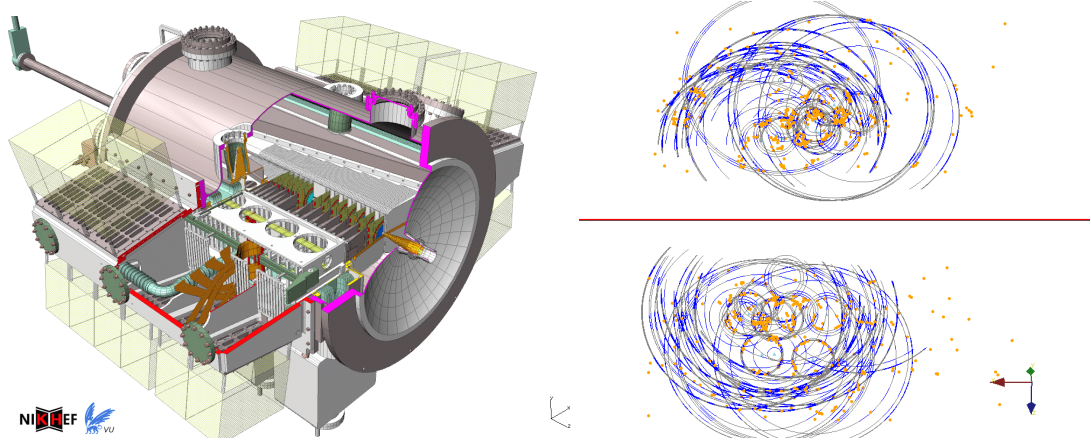
Fig. 4.6: Left: CAD drawing of the VELO detector, showing the VELO disks and support structures [87]. Right: Reconstructed Cherenkov rings in the RICH1 detector [88].

RICH1 is located between VELO and TT, upstream of the magnet. It covers the acceptance for particles with low to medium momenta, i.e. between 1 and 65 GeV/c. It employs an aerogel ($n = 1.03$) allowing for a kaon identification above 2 GeV/c and a π-K-separation up to 10 GeV/c, as well as a C_4F_{10} radiator for π-K-separation up to 60 GeV/c. RICH2 is installed downstream of the magnet, between the tracking station T3 and the M1 muon chamber. It uses CF_4, providing a π-K-separation in the medium and high momentum range of 20 to 60 GeV/c.

The calorimeters

Besides providing particle identification for electrons, photons, and hadrons, the calorimeter system offers additional energy and position measurements, that serve as an important input to the L0 hardware trigger. The calorimeter system is installed between the muon stations M1 and M2. The Electromagnetic Calorimeter (ECAL), which is supplemented by the Scintillating Pad Detector (SPD) and the Preshower (PS), is followed by the Hadronic Calorimeter (HCAL). All calorimeter sub-detectors use scintillating material to measure the energy deposition

of the showers. The produced scintillation light is picked up by wavelength-shifting fibres (WLS) and passed on to photon detectors. To ensure a nearly constant angular resolution, the detectors are segmented in the xy-plane with an increase of granularity towards the beam axis.

The SPD is the first calorimeter unit and consists of 15 mm thick scintillating tiles. It is sensitive to charged particles and allows for distinction of photons and electrons: Electrons leave clusters in SPD and ECAL, while photons only shower in the ECAL. The PS consists of a layer of scintillating tiles separated from the SPD by a 12 mm thick lead layer. As electrons have a high probability of showering up in the lead plate, this allows for the distinction of electrons and charged hadrons, like pions. Both SPD and PS use multi-anode photomultipliers in the readout. The ECAL sampling calorimeter design follows the "Shashlik" technology using 4 mm thick scintillator plates which are inter-spaced with 66 lead absorber sheets of 2 mm thickness. Hereby, it fully contains showers from high energy photons. The HCAL is a sampling calorimeter using 4 mm thick scintillating plates inter-spaced with 16 mm thick iron tiles, adding up to a total thickness of 1.2 m.

The muon system

A large number of b decays involve final states with muons, e.g. b decays into $J/\psi X$, with a subsequent $J/\psi \rightarrow \mu^+\mu^-$ decay, or the rare $B_s^0 \rightarrow \mu^+\mu^-$ decay, and are therefore preferably used to trigger potentially interesting events. Hence, an efficient and reliable muon detection and identification is indispensable for LHCb's physics goals.

The muon system consists of five stations, M1–M5, located upstream (M1) and downstream (M2–M5) of the calorimeters. The latter stations are separated by 80 cm thick iron filters. A minimum momentum of 5 GeV/c is required for a particle to traverse all five stations. Each station is divided into four regions of different readout granularities that increase towards the beam axis. The M2 and M3 stations have a higher horizontal granularity to enhance the momentum measurement, while M4 and M5 only serve the identification of more penetrating particles. The M1 inner region is equipped with TripleGEM (Gas-electron Multipliers), while the rest of M1 as well as M2–M5 have active areas consisting of a total of 1380 chambers of Multi Wire Proportional Chambers (MWPCs) with 2 mm wire spacing and 5 mm gas gaps. The gas mixture of Ar/CO$_2$/CF$_4$ allows for detection efficiencies > 95%.

4.4 The LHCb Trigger and readout system

Reducing the amount of output data, while maximising the ratio of physically interesting events, is the duty of LHCb's two successive trigger stages. The first, the Level 0 trigger (L0), is a hardware trigger with the task to reduce the nominal event rate, given by the bunch crossing rate of 40 MHz, to 1 MHz of events. In L0 triggered events, all sub-detectors are readout and the data is further processed by the second trigger stage, the High Level Trigger (HLT). This software trigger further reduces the output rate to 5 kHz of events, which are then written to disk for further analysis. A schematic representation of the trigger and readout system is shown in Fig. 4.7. The following description is based on Ref. [89].
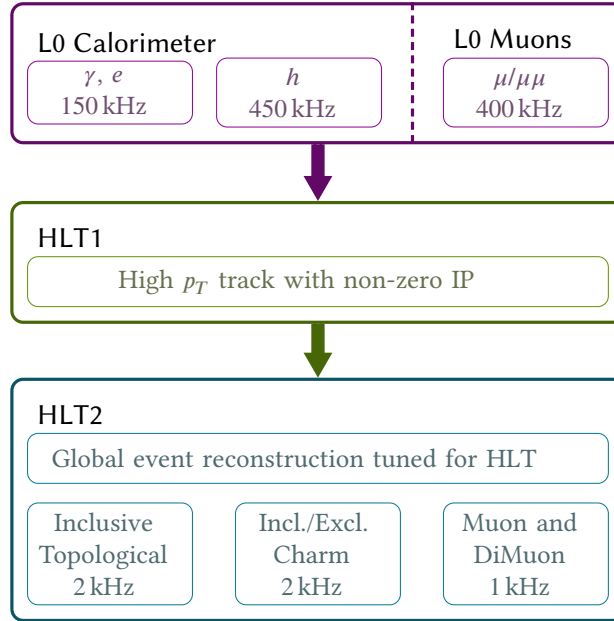
Fig. 4.7: LHCb trigger architecture as used in 2011. Based on Ref. [89].

4.4.1 The L0 triggers

The ultimate L0 trigger decision comes from the L0 decision unit (L0DU) which collects information from the L0 Calorimeter triggers, the L0 Muon triggers, and the L0 Pile-Up system at a rate of 40 MHz.

The L0 calorimeter triggers identify events with particles that leave high transverse energies, E_T, in the calorimetry system. For this, E_T sums in cell clusters in each the ECAL and the HCAL are computed. The cluster information from the calorimeter sub-detectors are then merged to perform an identification of the shower type. ECAL cluster information is merged with the PS and SPD information to identify γ and e showers and correctly sum up their E_T. A photon candidate (L0Photon) is built from the highest E_T cluster in the ECAL with hits in the PS but not in the SPD. A potential electron candidate (L0Electron) has the same requirements as a photon candidate, but additionally requires a suitable SPD hit. Similarly, the HCAL and ECAL information are merged to arrive at E_T information for hadron candidates (L0Hadron). Only the highest E_T candidate per particle type is passed on to the L0 decision unit, together with the cluster multiplicity in the SPD.

The L0 Muon trigger searches for the two muon candidates with the highest transverse momentum p_T in each quadrant of the muon stations, resulting in a maximum of 8 muon candidates being considered for a trigger decision. Hits in M3 are seeds for tracks that are then extrapolated into M2, M4, and M5 as a straight line to the nominal interaction point. If hits in M2, M4, and M5 lie in the proximity of the track extrapolation, they are attributed to the track, which is subsequently flagged as a muon track. The transverse momentum is estimated by using a straight-line extrapolation from M2 and M3 into M1.

The two highest transverse momenta of the muon candidates are passed to the L0 decision unit. A positive trigger decision either requires a minimum value for the highest p_T (L0Muon) or for the product of the transverse momenta (L0DiMuon) of the two selected muon candidates.

The L0 Pile-Up system consists of two stations of pure r sensor modules upstream of the VELO. The r sensor strips are subdivided into 45° sectors which allow for a coarse sensitivity in ϕ. In each event, all pairs of hits in the two modules that share an octant are used to estimate the z position of their particle's origin. A straight-line extrapolation onto the beam axis is performed and the resulting z positions are histogrammed. The number of peaks in the histogram corresponds to the number of pp interaction points, and is passed to the L0 decision unit. In the 2011 run, the L0 PU has not been used for trigger selection.

The L0 decision unit combines the information of the L0 subsystems in an algorithm to arrive at a final L0 decision. A Trigger Configuration Key (TCK) is chosen prior to data taking, and defines the threshold configuration. The choice of the TCK depends on the beam and running conditions. One of the thresholds, the maximum allowed SPD multiplicity, avoids disproportionate computing time in the HLT. Other configuration parameters are the E_T thresholds for the L0 Calorimeter trigger information, the L0 Muon p_T thresholds, and the information on pile-up.

The final decision is passed to the readout supervisor, which sends additional calibration and luminosity triggers for monitoring purposes. The readout supervisor forwards the L0 decision depending on the availability of the sub-detectors, prescales, and the status of the buffers.

4.4.2 The High Level Trigger

The HLT is a software application, which runs on the Event Filter Farm (EFF) consisting of 50 sub-farms and 15000 processors. The HLT uses the L0 triggered events to further reduce the output rate to 5 kHz. These are then stored to disk for further processing and analysis. To allow for an even higher effective write out rate, the HLT uses the node storages to temporarily store events that were accepted by L0 but could not be processed in parallel to data taking, due to limited computing resources. After a run, in the inter-fill time, the deferred HLT is started, which processes the events from the local storage.

The HLT has two stages, the HLT1 and HLT2. Its implementation in the 2010–2012 data taking period significantly differs from the design, where a 25 ns bunch spacing and a maximum number of visible pp-interactions per bunch-crossing of $\mu = 0.4$ was assumed. Instead, a bunch spacing of 50 ns was used and the LHCb detector performance was shown to be stable up to $\mu = 2.5$. Both HLTs consist of configurable trigger lines, each covering a certain class of events. The lines can be configured by a Trigger Configuration Key, just like the L0 trigger. In 2011, a typical TCK contained settings for $\approx$ 20 L0 lines, $\approx$ 40 HLT1 lines, and $\approx$ 130 HLT2 lines [89].

The HLT1 heavily relies on track segments formed from hits in the VELO. Vertices are constructed from at least five of these tracks. The vertices are assumed to be primary vertices if they lie within a radius of 300 μm of the mean pp-interaction region, which is determined at the beginning of a run. HLT1 lines that do not require muons base their trigger decisions on

the properties of the VELO tracks with the smallest impact parameter to any primary vertex and with a minimum number of hits in the VELO. In contrast, HLT1 lines that require muons only use events triggered by L0 Muon.

The HLT2 uses events triggered by HLT1. As this event rate is sufficiently low, forward tracking for all VELO tracks is performed. Forward tracking will be explained in Sec. 4.5.1. Only tracks with $p > 5\,\text{GeV}/c$ and $p_\text{T} > 0.5\,\text{GeV}/c$ are reconstructed, limiting the size of the search windows in the T stations. For muons, the standard offline muon identification is used. The largest share of the HLT2 output rate is allocated to the topological lines, which attempt an inclusive, partial reconstruction of b hadron decays. They require at least two charged particles in the final state and a displaced decay vertex. A smaller share of the output rate is taken by the trigger lines for events with displaced $J/\psi \rightarrow \mu^+\mu^-$ decays, which are most important for the triggering of $B^0 \rightarrow J/\psi\,K_S^0$ decays and other $B \rightarrow J/\psi\,X$ channels. Other lines are dedicated to the triggering of charm decays by requiring an exclusive reconstruction of the decay products.

4.5 The LHCb Software

Data recorded by the LHCb detector can be processed and analysed with the LHCb software. The LHCb software framework is based on GAUDI [90], an open project with special interfaces and services for high energy physics experiments. GAUDI is used by both the LHCb and the ATLAS collaboration. It is organised in several software packages with dedicated tasks and fields of application. In the following sections, only the most important packages will be described, except for the MOORE package, which holds the code of the High Level Trigger and has been implicitly described in Sec. 4.4.2. Thus, the discussion will be limited to LHCb's reconstruction software package BRUNEL, the main end-user analysis software package DAVINCI, and the packages GAUSS and BOOLE for the production of simulated data samples.

4.5.1 Reconstruction

The BRUNEL software project [91] provides interfaces to the algorithms and tools for the event reconstruction. These tools take care of tracking, i.e. the reconstruction of charged particle tracks from the hits in the tracking system, the reconstruction of neutral particles using the calorimeter information, and particle identification (PID), where calorimeter clusters, RICH rings, and hits in the muon stations are evaluated. By combining these inputs, the event reconstruction creates protoparticle objects, which carry the information from tracking and particle identification, and can be used in the further reconstruction of specific decays and processes. BRUNEL can process both the output of LHCb's data acquisition system and of simulated data, where the latter will be described in Sec. 4.5.3.

As the decay $B^0 \rightarrow J/\psi\,K_S^0$ is reconstructed using the subsequent $J/\psi \rightarrow \mu^+\mu^-$ and $K_S^0 \rightarrow \pi^+\pi^-$ decays, the following discussion will be limited to the track reconstruction and particle identification of charged particles.
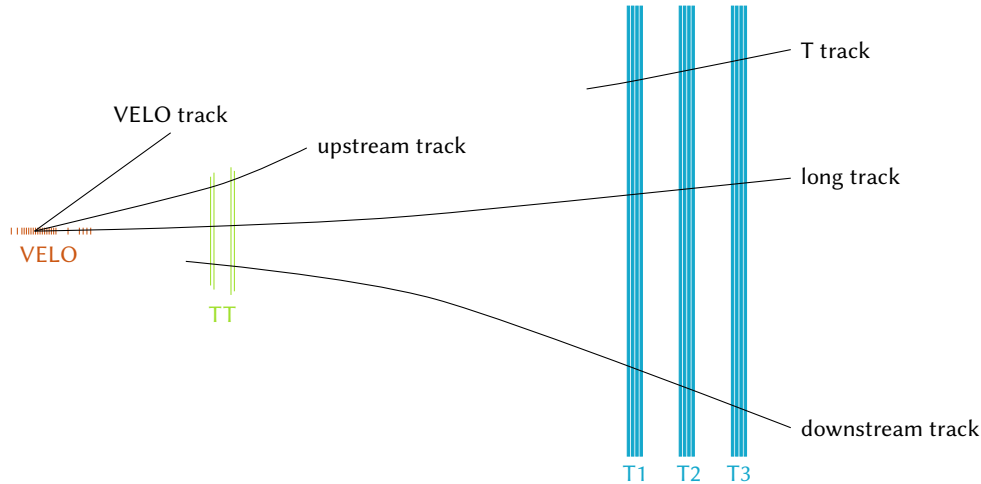
Fig. 4.8: Schematic view of LHCb's xz-plane, illustrating the tracking stations and the different track types.

Tracking

A track is represented by state vectors at z_i positions along the track. Each state vector consists of the x and y position, the slopes in the xz and xy projections, and the charge divided by the momentum at that position. Additionally, the covariance matrices add the information on the uncertainty of the track into the representation. The nominal track reconstruction applies different tracking strategies to construct tracks from sub-detector hits. Pattern recognition and tracking algorithms search for specific patterns in the sub-detectors and use them to form multiple track types, which are illustrated in Fig. 4.8.

The reconstruction process starts by using hits in the VELO r and ϕ sensors to form *VELO tracks*. These tracks are formed by a pattern recognition algorithm that searches for straight lines [92, 93]. These are the starting points for two algorithms that attempt the reconstruction of tracks that traverse the full tracking system, so-called *long tracks*. The first, the forward tracking algorithm, extrapolates each VELO track to each hit in the T stations, while taking into account the magnetic field map. Each of these combinations is extrapolated onto a Hough plane [94], which does not match any of the real detector planes. Extrapolated tracks with T hits that belong to the same particle will cluster in the Hough plane, while a more random distribution is expected otherwise. Using these clusters together with compatible TT hits leads to the reconstruction of the long tracks. The second method, the track matching algorithm, combines VELO tracks with *T tracks*, which are formed from hits in the T stations. Adding compatible TT hits again leads to the creation of long tracks.

The other important type of tracks are the *downstream tracks*, which are formed by using T tracks and matching them to hits in the TT. Tracks of this type are typically produced by the charged decay products of long-lived particles, e.g. K_S^0 or Λ, which often decay outside the VELO acceptance. Downstream tracking is followed by the construction of *upstream tracks*. These are formed from VELO tracks and TT hits. Tracks of this type can be produced by low

momentum particles which are swept out of the detector acceptance by the magnetic field behind the TT. However, they are useful for vertex reconstruction in the VELO.

Duplicate tracks formed by different tracking algorithms are removed by a Clone Killer algorithm. If two tracks share more hits than a certain threshold, the shorter track is omitted. A track fit using a Kalman filter estimates the trajectory of the particle [95]. It takes energy losses and multiple scattering effects into account and allows for a momentum measurement. This step takes the largest share of computing time in the track reconstruction and is therefore performed after applying the Clone Killer.

For *B* physics analysis, the most useful tracks are long tracks, as these provide the most precise information on the trajectories and momenta. However, for physics analyses with long-lived particles in the final state, such as $B^0 \to J/\psi K_S^0$, the number of reconstructed decays can be significantly increased by including downstream tracks, with the drawback of a slightly worse momentum and space resolution.

Particle identification

The identification of charged particles, in particular e, μ, π, K, and p particles, is based on a combination of information from the RICH detectors, the calorimeters, and the muon system [82].

The PID information of the RICH system, which is most important for charged hadron identification, is obtained by extrapolating all tracks into the RICH detectors and calculating a global likelihood for all combinations of tracks and pixel hits while varying the particle hypotheses for each track. The result is a likelihood value for each track and each hypothesis. Muon identification is obtained by searching for hits in the muon stations that lie in the vicinity of the extrapolated particle trajectories. For each track, a likelihood for the muon and the non-muon hypotheses is calculated based on the distance of muon hits to the track extrapolation. The calorimetry system is mainly used for the identification of electrons and neutral pions, and helps in the recovery of bremsstrahlung photons [96]. Additionally, it gives some input to the identification of charged hadrons through matching of calorimeter clusters to extrapolated tracks. For charged particles, the information from all PID systems, in particular the likelihood ratios for different particle hypotheses, are combined into a global likelihood using neural nets. Differences of the logarithmic likelihood between different hypotheses can then be used to minimise misidentification in the offline data selection.

4.5.2 Data selection and Stripping

The final step of data analysis within the LHCb software framework is performed using the DaVinci project [97]. It uses the protoparticles created in the reconstruction together with a particle hypothesis to form particle objects, which can then be combined to intermediate states and ultimately lead to the reconstruction of a full decay chain.

DaVinci has access to a variety of algorithms that produce observables relevant for the broad spectrum of LHCb analyses, e.g. algorithms to reconstruct and fit particle decay chains, to estimate kinematic observables of all intermediate particles, to determine the output of the particle identification system, to analyse the trigger response, or, in case of simulated

datasets, to match the reconstructed particles to their simulated partners. The output of the algorithms can be used to define minimum requirements on the quality of the reconstructed and combined particles, allowing for a reduction of background candidates and computing time.

As the amount of data produced by LHCb is large, computing resources would be inefficiently used if every analyst had access to the full datasets for reconstructing the relevant decays, in particular, as many decays which are under study share the same type of intermediate particles, e.g. the group of $B_{u,d,s} \rightarrow J/\psi X$ decays. Instead, a collaboration wide selection effort called *Stripping* is organised and performed centrally. Exclusive and inclusive selections of decays are applied, where the selection requirements are defined by the analysts but computing constraints per event must be met. Typically, looser requirements than in the final analyses are applied to allow for additional studies, e.g. involving more background candidates. Stripped data is made accessible to the analysts and can be processed with DaVinci to create ROOT tuples [98] that contain the relevant event and candidate information, which are then used as input to the analyses. Restripping of the data is performed to allow the analyses to profit from enhancements in the reconstruction software.

4.5.3 Simulation

In the great majority of physics analyses, it is inevitable to prove the sanity of the analysis strategy, as well as to estimate and understand the influence of data taking, reconstruction, and physics effects on the analysis goal. An indispensable input are simulated datasets which are as similar to real data as possible and take into account the data taking conditions, e.g. the specific beam setup, as well as the configuration of the trigger and the reconstruction. In LHCb, simulated datasets are produced with the help of the software projects Gauss [99, 100] and Boole [101], followed by the "standard" chain of Moore for the trigger simulation, Brunel for the reconstruction, and DaVinci for the stripping selection.

The Gauss project simulates the LHC bunch crossings, the production and decay of intermediate resonances in the *pp* interactions, and the interaction of the resulting particles with the detector. In the generation phase, *pp* collisions and the resulting production of particles are simulated with the PYTHIA event generator [102, 103]. The decay of the particles is simulated using EvtGen, a Monte Carlo generator developed for the accurate description of *b* hadron decays, including *CP* violation and mixing [104]. EvtGen uses the PHOTOS library to handle radiative corrections [105]. Additionally, various interfaces to other MC generators [106], like HERWIG++ [107] and SHERPA [108, 109], exist. The generation phase is followed by a simulation phase, in which the passage of the particles and their interaction with the detector material is simulated using GEANT4 [110, 111].

The Boole digitization project [101] takes care of the final simulation stage. It uses the datasets simulated by Gauss and translates the particle interactions with the detector material, e.g. deposited charges in the silicon modules or particle showers in the calorimeters, into detector signals as seen in real data. It simulates the detector response, the readout electronics, and the L0 trigger hardware including noise and cross-talk, and can add spillover events from previous or subsequent beam crossings.

The DaVinci project can run on the simulated data and access the MC information, to match reconstructed tracks or particles with their MC partners. This is especially helpful for evaluation of background components, e.g. from misidentified *B* decays.

4.6 Running conditions

LHC was designed to run at a centre-of-mass energy of 14 TeV, an instantaneous luminosity of $10^{34}\,\mathrm{cm^{-2}\,s^{-1}}$, a bunch spacing of 25 ns, and a large number of proton interactions per bunch-crossing (pile-up). Though, the physics goal of LHCb, which is focussed on precision measurements of heavy flavour hadrons, relies on a clean determination of primary and secondary vertices. Hence, LHCb was designed to run at an instantaneous luminosity of $2\cdot10^{32}\,\mathrm{cm^{-2}\,s^{-1}}$, a factor 50 below LHC's design luminosity, and at an average number of interactions per bunch-crossing of 0.4. To arrive at such a lower instantaneous luminosity, it was planned to use a weaker focussing of the beams at the LHCb interaction point. After the LHC start and the subsequent accident, it was clear that the design luminosity could not be met before a long shutdown phase. The resulting decisions for the LHC beam configurations in the data taking period 2010–2012 have been briefly discussed in Sec. 4.1. An overview of the evolution of the LHCb running conditions along the developments of LHC from 2010 to 2012 is shown in Fig. 4.9. A more thorough description can be found in Ref. [112].
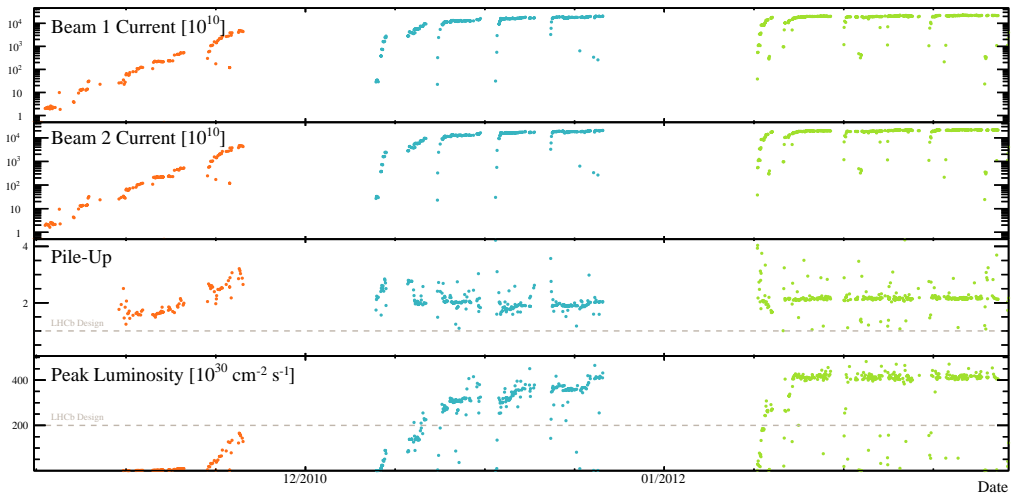
Fig. 4.9: Development of the data taking conditions at LHCb in 2010 (orange), 2011 (blue), and 2012 (green), in terms of the beam currents, the average pile-up, and the peak instantaneous luminosity. The grey lines in the pile-up and luminosity plots represent the LHCb design goals for these quantities. Adapted from Ref. [112]

In 2011, LHC collided proton bunches at a rate of 20 MHz and a centre-of-mass energy of $\sqrt{s}=7$ TeV. In LHCb, a maximum instantaneous luminosity of $4\cdot10^{32}\,\mathrm{cm^{-2}\,s^{-1}}$ at a visible bunch crossing rate of approximately 12 MHz and a visible pile-up per visible bunch crossing of up to 2.4 was found to be optimal, clearly beyond LHCb's design specifications. A constant instantaneous luminosity at a constant pile-up throughout a fill could be achieved

by introducing luminosity leveling. For this, LHC displaces the two colliding beams in LHCb, hereby reducing the effective interaction region and lowering the *pp* interaction probability per bunch crossing. Furthermore, the decrease of the beam intensity within a fill allows for a constant luminosity within LHCb by adjusting the displacement of the beams, while allowing the other experiments to make use of the maximally available instantaneous luminosity, as can be seen in Fig. 4.10.

Throughout the 2011 data taking, LHCb collected a dataset corresponding to an integrated luminosity of $1\,\text{fb}^{-1}$ at an operational efficiency of 91%. More than 99% of the collected data was found to be usable for offline data analysis. Of this data, 61% was recorded with one magnet polarity, and the rest of the data with the opposite polarity.
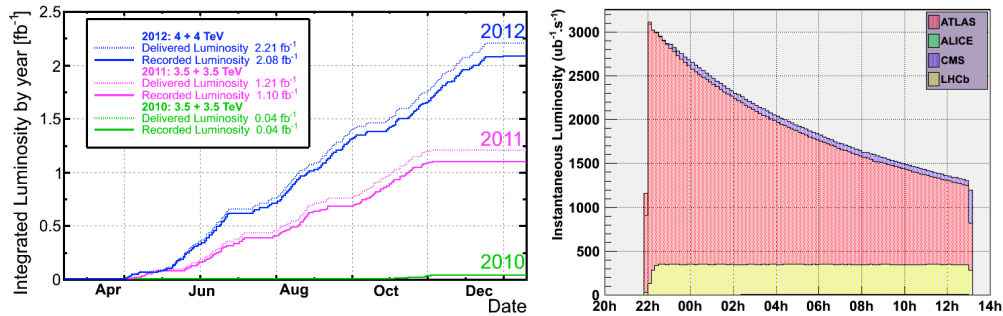
Fig. 4.10: Left: Evolution of the integrated luminosity throughout each of the years of data taking. Right: Development of the instantaneous luminosity throughout an LHC fill, as measured at the experiments' interaction points. While ATLAS and CMS make use of the maximally available luminosity, which decreases throughout a fill due to beam losses, LHCb's luminosity leveling allows for a lower, but constant instantaneous luminosity throughout the fill.

47

5 Analysis Strategy and Tools

The measurement of CP violation in transitions of $B^0/\bar{B}^0$ mesons to their common CP eigenstate $J/\psi K_S^0$ requires the analysis of the time-dependent differential decay rates

$$\Gamma(B^0(t) \to J/\psi K_S^0) = \frac{\tilde{A}}{2}\mathrm{e}^{-t/\tau}\left(1 + C\cos\Delta m\,t - S\sin\Delta m\,t\right), \tag{5.1a}$$

$$\Gamma(\bar{B}^0(t) \to J/\psi K_S^0) = \frac{\tilde{A}}{2}\mathrm{e}^{-t/\tau}\left(1 - C\cos\Delta m\,t + S\sin\Delta m\,t\right), \tag{5.1b}$$

where $\tilde{A}$ is a normalisation factor, τ is the B^0 meson lifetime, Δm is the mass difference of the heavy and light mass eigenstates of the B^0 meson, and S and C are the short-hand notations for the CP parameters $S_{J/\psi K_S^0}$ and $C_{J/\psi K_S^0}$, respectively. Similarly to the derivation of the time-dependent decay rates in Ch. 3, CP violation in the mixing has been neglected, $|q/p| = 1$, and the decay width difference is assumed to vanish, $\Delta\Gamma = 0$. The CP violating effects lead to a time-dependent decay rate asymmetry,

$$\mathcal{A}(t) = \frac{\Gamma(\bar{B}^0(t) \to J/\psi K_S^0) - \Gamma(B^0(t) \to J/\psi K_S^0)}{\Gamma(\bar{B}^0(t) \to J/\psi K_S^0) + \Gamma(B^0(t) \to J/\psi K_S^0)} = S\sin\Delta m\,t - C\cos\Delta m\,t, \tag{5.2}$$

as well as to a time-integrated asymmetry,

$$\mathcal{A} = \frac{\int_0^\infty \mathrm{d}t\,\Gamma(\bar{B}^0(t) \to J/\psi K_S^0) - \int_0^\infty \mathrm{d}t\,\Gamma(B^0(t) \to J/\psi K_S^0)(t)}{\int_0^\infty \mathrm{d}t\,\Gamma(\bar{B}^0(t) \to J/\psi K_S^0) + \int_0^\infty \mathrm{d}t\,\Gamma(B^0(t) \to J/\psi K_S^0)(t)} = \frac{xS - C}{1 + x^2}, \tag{5.3}$$

where $x = \Delta m\,\tau$ has been used. To simultaneously exploit the decay rate distributions as well as both time-dependent and time-independent asymmetries for a measurement of S and C, four main steps are required:

- The $B^0 \to J/\psi K_S^0$ decays are reconstructed and selection requirements are imposed, aiming for a a data sample with a reasonably high signal-to-background ratio.

- For each B^0 candidate, its initial production flavour is identified using flavour tagging methods.

- An accurate determination of the decay time t is required, i.e. the time passing between production and decay of the reconstructed B^0 candidate as measured in its restframe.

- The resulting data sample is analysed statistically through a maximum likelihood fit to arrive at estimates for the parameters S and C. This step requires a suitable description in terms of probability density functions (PDFs).

Unfortunately, none of these steps can be executed perfectly. For instance, detector acceptances, as well as selection and trigger requirements, which aim for a reduction of erroneously reconstructed candidates, i.e. background, lead to reconstruction inefficiencies that could non-trivially affect the measurable asymmetries, e.g. when they depend on the decay time. Additionally, it is necessary to control the ratio of produced B^0 and $\bar{B}^0$ mesons in the sample. Ignoring a non-vanishing production asymmetry that enhances the observed relative decay rate of either B^0 or $\bar{B}^0$ would bias the measured asymmetries. Inaccuracies in the flavour tagging need to be understood, as these change the measurable asymmetry. Furthermore, uncertainties from track reconstruction and momentum measurements, as well as inadequately reconstructed coordinates of primary and decay vertices, lead to a non-vanishing resolution, which can distort the measured decay time distribution. As neutral B^0 mesons oscillate between their flavour and anti-flavour states with a frequency of $\mathcal{O}(0.1\,\mathrm{ps}^{-1})$, large decay time uncertainties can as well distort the experimentally accessible time-dependent asymmetry.

Hence, before shortly describing the individual steps of the analysis, it is important to understand how experimental realities can change the resulting observable distributions and asymmetries.

5.1 Dilutions, intrinsic asymmetries, and efficiencies

In contrast to the true, theoretically motivated asymmetry $\mathcal{A}(t)$, which is defined by the time-dependent decay rates $\Gamma(t)$ of B^0 and $\bar{B}^0$ mesons, the observed asymmetry $\mathcal{A}_{\mathrm{obs}}(t)$ is given by the asymmetry between $N_{B^0}(t)$ and $N_{\bar{B}^0}(t)$, the numbers of reconstructed candidates which have been tagged as B^0 or $\bar{B}^0$, respectively, and have decayed at a measured decay time t,

$$\mathcal{A}_{\mathrm{obs}}(t) = \frac{N_{\bar{B}^0}(t) - N_{B^0}(t)}{N_{\bar{B}^0}(t) + N_{B^0}(t)}\,. \tag{5.4}$$

To correctly determine the *CP* violation parameters S and C, it is necessary to express the observed asymmetry $\mathcal{A}_{\mathrm{obs}}(t)$ in terms of the true asymmetry $\mathcal{A}(t)$. Under perfect experimental conditions, both are equal. However, experimental effects can dilute the true asymmetry or/and add intrinsic asymmetries to the observable asymmetry. Thus, the relationship between the two asymmetries can be expressed, up to $\mathcal{O}(\mathcal{A}(t))$, as

$$\mathcal{A}_{\mathrm{obs}}(t) \approx \mathcal{D}\mathcal{A}(t) + I\,, \tag{5.5}$$

where I represents the intrinsic asymmetry and $\mathcal{D}$ is the dilution factor, which can take values between 0 and 1. A large dilution factor is equivalent to a vanishing dilution, and hence leads to a higher statistical sensitivity of the experiment, as will be shown below. An example of the difference between true and observed time-dependent asymmetry is shown in Fig. 5.1. Typically, as many different contributions are involved, the global dilution factor $\mathcal{D}$ is a product of several dilution factors, while the intrinsic asymmetry I is a sum of several asymmetries, each from a different source. It is further important to note, that both, I and $\mathcal{D}$, can depend on the decay time t.
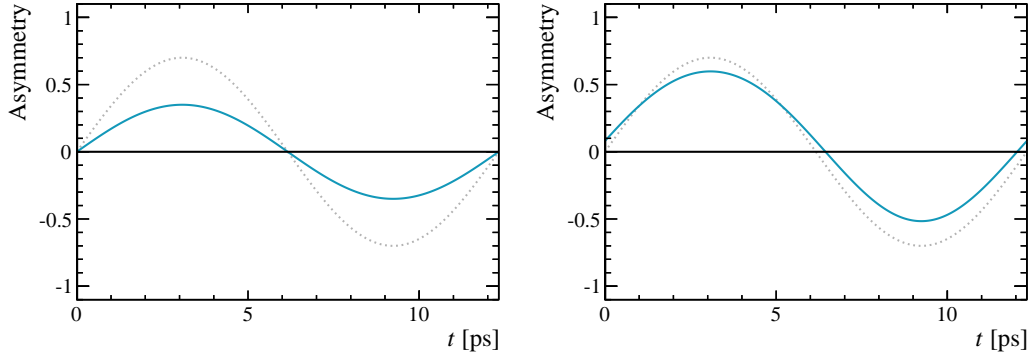
Fig. 5.1: Effect of intrinsic asymmetries and dilutions on the observed asymmetry, assuming $S = 0.7$ and $C = 0$. Left: Observed asymmetry with a dilution factor $\mathcal{D} = 0.5$ and an intrinsic asymmetry of $I = 0$. Right: Observed asymmetry with $\mathcal{D} = 0.8$ and $I = 0.1$. In both plots, the true asymmetry is depicted by the dotted, gray line.

To simplify the further discussion, all above quantities are treated as time-independent quantities, including observed and true asymmetries, dilution factors, as well as intrinsic asymmetries. Then, the true asymmetry $\mathcal{A}$ is given by

$$\mathcal{A} = \frac{1}{\mathcal{D}}\left(\mathcal{A}_{\text{obs}} - I\right) = \frac{1}{\mathcal{D}}\left(\frac{N_{\bar{B}^0} - N_{B^0}}{N_{\bar{B}^0} + N_{B^0}} - I\right). \tag{5.6}$$

In the Gaussian approximation, the uncertainty on the true asymmetry is given by

$$
\begin{aligned}
\sigma_{\mathcal{A}}^2 &= \left(\frac{\partial \mathcal{A}}{\partial N_{\bar{B}^0}}\right)^2 \sigma_{N_{\bar{B}^0}}^2 + \left(\frac{\partial \mathcal{A}}{\partial N_{B^0}}\right)^2 \sigma_{N_{B^0}}^2 + \left(\frac{\partial \mathcal{A}}{\partial I}\right)^2 \sigma_I^2 + \left(\frac{\partial \mathcal{A}}{\partial \mathcal{D}}\right)^2 \sigma_{\mathcal{D}}^2 \\
&= \frac{1}{\mathcal{D}^2}\frac{1}{N_{\bar{B}^0} + N_{B^0}} \cdot (1 - \mathcal{A}_{\text{obs}}^2) + \frac{1}{\mathcal{D}^2}\sigma_I^2 + \left(\frac{\mathcal{A}}{\mathcal{D}}\right)^2 \sigma_{\mathcal{D}}^2.
\end{aligned}
\tag{5.7}
$$

This expression can be significantly reduced by assuming a small dilution factor and a small intrinsic asymmetry, both with negligible uncertainties, hereby implying $\mathcal{A}_{\text{obs}}^2 \ll 1$, and therefore

$$\sigma_{\mathcal{A}}^2 \approx \frac{1}{\mathcal{D}^2}\frac{1}{N_{\bar{B}^0} + N_{B^0}}. \tag{5.8}$$

Further, it is useful to express the number of reconstructed and tagged candidates, $N_{\bar{B}^0} + N_{B^0}$, in terms of the original number of decays N that are available in the sample,

$$N_{\bar{B}^0} + N_{B^0} = \varepsilon N, \tag{5.9}$$

where ε is the product of the efficiencies of each step applied in the analysis, e.g. event triggering, reconstruction, candidate selection, and tagging. Again, ε can depend on the reconstructed decay time t and on the initial flavour of the meson.

Taking all these simplifications into account, the uncertainty on the asymmetry is given by

$$\sigma_{\mathcal{A}} \approx \frac{1}{\sqrt{\varepsilon \mathcal{D}^2 N}}. \tag{5.10}$$

The factor $\varepsilon \mathcal{D}^2$ is called the effective efficiency, and represents the statistical power of the applied experimental methods. An $\varepsilon \mathcal{D}^2$ of 1 is equivalent to a perfect experimental setup that exploits all produced $B^0/\bar{B}^0$ mesons that decay into $J/\psi K_S^0$ final states without any efficiency losses or background contributions.

Clearly, the above considerations are oversimplified. Hence, they are not directly applicable to the full analysis pursued in the measurement. However, they are essential for a basic understanding of the impact of experimental issues on the analysis. In addition, this discussion underlines the importance of maximising $\varepsilon \mathcal{D}^2$. A more thorough and quantitative discussion can be found in Refs. [113, 114].

5.2 Selection and reconstruction

The $B^0 \rightarrow J/\psi K_S^0$ decays are reconstructed through the secondary $J/\psi \rightarrow \mu^+\mu^-$ and $K_S^0 \rightarrow \pi^+\pi^-$ decays. Although the former decay has a branching fraction of only $\approx 6\%$, it is much cleaner than a reconstruction of the equally probable decay $J/\psi \rightarrow e^+e^-$ or the dominant decays into hadronic final states, as both electrons and hadrons are more frequently produced in other processes, leading to a lower signal-to-background ratio. In addition, muons are reliably detected by the muon system and are used in all steps of the trigger, as explained in Ch. 4, so that a higher overall reconstruction efficiency can be expected. In contrast, limiting the reconstruction of K_S^0 to the $\pi^+\pi^-$ decay, which corresponds to a branching fraction of $\approx 69\%$, does not significantly reduce the number of candidates. This holds true all the more, considering that the second most probable decay, $K_S^0 \rightarrow \pi^0\pi^0$ with a branching fraction of $\approx 31\%$, would require the reconstruction of $\pi^0 \rightarrow \gamma\gamma$, where a low reconstruction efficiency and signal-to-background ratio is expected in LHCb. Hence, the branching fraction of the full $B^0 \rightarrow J/\psi K_S^0 \rightarrow \mu^+\mu^-\pi^+\pi^-$ decay chain used in the selection is

$$\mathcal{B}_{\text{sel}} = \mathcal{B}(B^0 \rightarrow J/\psi K_S^0 \rightarrow \mu^+\mu^-\pi^+\pi^-) = (1.79 \pm 0.07) \cdot 10^{-5}. \tag{5.11}$$

Now, the expected signal event yield N prior to selection and reconstruction can be expressed as

$$N = \mathcal{L}_{\text{int}} \cdot \sigma_{b\bar{b}} \cdot 2 \cdot f_d \cdot \mathcal{B}_{\text{sel}}. \tag{5.12}$$

For the data sample collected by LHCb in 2011 at a centre-of-mass energy of 7 TeV, which corresponds to an integrated luminosity of $\mathcal{L}_{\text{int}} = 1\,\text{fb}^{-1}$, a production cross-section for $b\bar{b}$ quark pairs has been measured by LHCb as $\sigma_{b\bar{b}} = \sigma(pp \rightarrow b\bar{b}X) = (284 \pm 53)\,\mu\text{b}$ [75]. The factor of 2 in Eq. (5.12) accounts for the pair production, as each of the quarks can hadronise into a B^0. Assuming a fragmentation fraction of $f_d \approx 34\%$ into B^0 mesons [77, 115], allows to estimate the number of produced $B^0/\bar{B}^0$ as approximately $193 \cdot 10^9$. Of these, 3.4 million decay into the $\mu^+\mu^-\pi^+\pi^-$ final state via an intermediate $J/\psi K_S^0$ state.

To further estimate the number of expected reconstructed decays N_{rec} that are available for an analysis, it is necessary to assess the total reconstruction efficiency ϵ_{tot},

$$\varepsilon_{\text{tot}} = \varepsilon_{J/\psi,\text{acc}} \cdot \varepsilon_{\text{trig}} \cdot \varepsilon_{\text{rec}} \cdot \varepsilon_{\text{sel}} \tag{5.13}$$

which combines LHCb's geometric acceptance $\varepsilon_{J/\psi,\text{acc}}$ for the di-muon pair, the efficiency $\varepsilon_{\text{trig}}$ to trigger an event containing a $B^0 \rightarrow J/\psi K_S^0$ decay with both muons in the detector

acceptance, and the efficiency $\varepsilon_{\text{rec}} \cdot \varepsilon_{\text{sel}}$ to reconstruct and select the full decay chain within a triggered event. Simulations suggest that only about 25% of the $b\bar{b}$ pairs are accessible to LHCb due to its reduced angular acceptance. Accordingly, only 18% of the $B^0 \rightarrow J/\psi K^0_S$ decays exhibit muons within the geometric acceptance, so that roughly 600 000 signal events could, in principle, be triggered by the muon triggers. Requiring L0, HLT1, and HLT2 trigger lines to trigger on muons in the event leads to a trigger efficiency $\varepsilon_{\text{trig}} \approx 65\%$, as supported by simulation and studies in other $B \rightarrow J/\psi X$ channels [89]. For the selection and reconstruction efficiency ε_{sel}, studies in the $B^0 \rightarrow J/\psi K^{*0}$ channel find values of $\approx 10\%$ [115]. In total, this would lead to a total efficiency of roughly 1%. However, as the K^0_S meson has a large lifetime and can therefore leave the detector acceptance before decaying, an even lower reconstruction efficiency can be expected for $B^0 \rightarrow J/\psi K^0_S$ decays, which is estimated from MC as $\approx 7\%$. Plugging all the above assumptions and numbers together leads to an expected signal yield of roughly 30 000 reconstructed $B^0 \rightarrow J/\psi K^0_S$ decays. A thorough description of the actual trigger and selection requirements will be given in Ch. 6.

5.3 Flavour tagging

In general, flavour tagging describes the procedure of inferring the initial flavour of a meson, i.e. whether it was produced as its particle or its anti-particle state. The choice of strategies depends on the particles that need to be tagged, e.g. the B^0 and B^0_s mesons, and on the experimental setup, e.g. an experiment like LHCb, which uses pp collisions and related $b\bar{b}$ pair production, requires other strategies than an experiment like Belle, which operates at the $\Upsilon(4S)$ resonance of the e^+e^- collider KEK.

LHCb's flavour tagging procedure for B mesons relies on a small variety of specialized algorithms, of which each gathers and evaluates information within an event to infer the initial flavour of a reconstructed B meson candidate. Thus, for each reconstructed B meson, each flavour tagging algorithm deduces a tag decision d. This tag decision takes a value of $+1$ (-1), whenever the reconstructed signal decay is tagged as an initial meson containing a $\bar{b}$ (b), e.g. the meson is tagged as B^0/B^0_s ($\bar{B}^0/\bar{B}^0_s$). If an algorithm fails to infer the production flavour, i.e. if the event does not offer the required characteristic signature, the algorithm returns a tag of $d = 0$. Besides assigning tags, each algorithm uses a neural network to estimate a probability η for a given tag to be correct, based on the properties of the tagging particles.

All algorithms base their tagging decision on the charge of particles – the tagging particles. By requiring special kinematic properties or particle identification information, the charge can be related to the initial flavour of the B meson. The requirements for the tagging particles are different among the tagging algorithms, which are developed using simulated events, while being tuned and optimised using suitable decay channels (control channels) in data. Depending on the exploited event topology, the flavour tagging algorithms in LHCb can be either classified as opposite-side or same-side taggers, see Fig. 5.2.

5.3.1 Opposite-side flavour tagging

The opposite-side taggers make use of the production process of b quarks [116]. At LHCb, b quarks are predominantly produced as $b\bar{b}$ pairs, see Sec. 4.2. Hence, besides the reconstructed
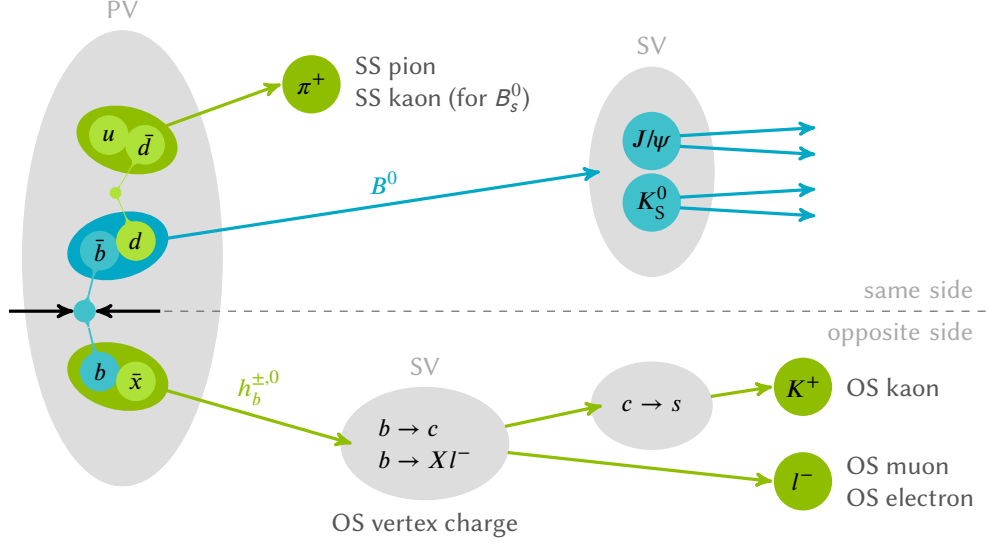
Fig. 5.2: Principle strategies of the flavour tagging algorithms used at LHCb. The algorithms exploit the by-products of the hadronisation of the signal B mesons (same-side tagging) and the decay products of the associated tagging b hadron $h_b^{\pm,0}$ (opposite-side tagging).

B meson (signal B), decay remnants of the associated b quark or rather of the b hadron (tagging B) should be present in the event. By reconstructing decay particles of the tagging B, the opposite-side tagging algorithms (OS taggers) identify its production flavour and by this infer the signal B flavour. This allows the use of all opposite-side flavour tagging algorithms for all B meson flavours (B^0, B_s^0, B^+). At the same time, all of these taggers have intrinsic mistag rates from flavour oscillations of the tagging B, in addition to the effects from mis-reconstructed and wrongly assigned tracks.

All taggers base their decision on the kinematic properties of charged particles with well reconstructed tracks. A good track fit quality, a minimum polar angle of 12 mrad with respect to the beam line, and a momentum larger than 2 GeV/c are required. To avoid the selection of track duplicates of the signal decay tracks, tagging particle tracks need to lie outside a cone of 5 mrad around any of the signal B daughters. Moreover, particle candidates are ignored by the taggers if they have a non-negligible chance to originate from a primary vertex that has not been associated to the B candidate.

The majority of opposite-side tagging algorithms – namely the electron, muon, and kaon tagger – are single particle taggers. These taggers base their tag decision on the charge of either electron, muon, or kaon candidates. If multiple tagging particles are found, the one with the highest transverse momentum is chosen for the determination of the tag decision.

The electron and the muon tagger exploit the leptons from semi-leptonic b decays, $b \to cl^-\bar{\nu}_l$, of the tagging B. The muon tagger uses tracks with $p_T > 1.2$ GeV/c, that are consistent with a muon hypothesis and do not share hits in the muon chambers with other tracks. The electron tagger searches for electron candidates that do not originate from photon conversions near the interaction point, have $p_T > 1.0$ GeV/c, and where the ratio of the energy E, as measured in the calorimeters, to the momentum p, as measured in the tracking system, exceeds $0.6\,c^{-1}$.

Additional intrinsic mistag rates of the lepton taggers can result from selecting tagging leptons from a $b \rightarrow c \rightarrow s l^+ \nu_l$ decay, leading to an incorrect tag.

The kaon tagger takes advantage of $b \rightarrow c \rightarrow s$ transitions of the tagging B by identifying kaon candidates with $p > 5.9\,\text{GeV}/c$, $p_{\text{T}} > 0.8\,\text{GeV}/c$, and RICH information that clearly supports a kaon hypothesis and disclaims proton and pion hypotheses. Additionally, a good separation from all primary vertices is required. Incorrect tags of the kaon tagger are often a result of selecting wrong sign kaons from fragmentation processes. Furthermore, charged kaons are known to interact differently with the detector material depending on their charge. Hence, small performance differences that depend on the initial flavour of the signal B meson can be expected.

The vertex charge tagger attempts an inclusive reconstruction of a secondary vertex that corresponds to the decay vertex of the tagging B. As many of the B hadron decays involve final states with neutral particles, which have a low reconstruction efficiency in LHCb, this method still allows for a meaningful tagging decision by determining the effective charge of the B hadron decay vertex. On the downside, this tagger can suffer from reconstructing decay vertices of D mesons originating from the decay of the tagging B, resulting in a converse tagging response, or from erroneously reconstructing decay products from a pile-up vertex. The first step of the vertex reconstruction involves the creation of composite particles from pairs of tracks with $p_{\text{T}} > 0.15\,\text{GeV}/c$ and good separation from the primary vertices. For each track combination with an invariant mass incompatible with the K_{S}^0 meson mass, a probability to originate from a tagging B decay is assessed based on vertex quality criteria together with kinematic and geomtric properties. The candidate with the highest probability is then used as a seed to the vertex reconstruction. Other tracks that are compatible with a creation at this vertex and do not originate from any primary vertex are added to the composite particle candidate. The resulting candidate is required to have $p > 10\,\text{GeV}/c$, $p_{\text{T}} > 1.5\,\text{GeV}/c$, and a total invariant mass $> 0.5\,\text{GeV}/c^2$. The charge Q_{vtx} of the secondary vertex candidate is calculated as the sum of the charges Q_i of its tracks weighted with their transverse momenta $p_{\text{T}i}$ to the power of $\kappa = 0.4$,

$$Q_{\text{vtx}} = \frac{\sum_i Q_i p_{\text{T}i}^{\kappa}}{\sum_i p_{\text{T}i}^{\kappa}}. \tag{5.14}$$

A positive charge, for instance from a reconstructed B^+ decay, results in a tag of $d = -1$, while a negative charge leads to a tag of $d = +1$. Vertices with $|Q_{\text{vtx}}| < 0.275$ are rejected, resulting in a tag of $d = 0$.

5.3.2 Same-side flavour tagging

The other class of flavour tagging algorithms consists of the same-side flavour taggers, which reconstruct charged hadronisation remnants of the signal B meson. In the case of a signal B_s^0 meson, an additional $\bar{s}$ quark can form a charged kaon, which allows to identify the initial flavour of the B_s^0 meson. This is exploited by the same-side kaon tagger. The selection of a suitable tagging kaon requires a high momentum charged track with a significant impact parameter with respect to the primary vertex and a good identification as a kaon. Further, the kaon's pseudorapidity and flight angle must lie around the signal B_s^0 candidate's flight direction [117].

Similarly, the additional $\bar{d}$ quark from the hadronisation process of the B^0 meson can form charged pions. Together with charged pions that originate from decays of excited B mesons, like $B^{**+} \rightarrow B^{(*)0}\pi^+X$, these serve as input to the same-side pion tagger. Again, requirements on the minimum momentum and the particle identification information are applied. In events with multiple pion candidates that pass the selection, the one with the highest transverse momentum is used. However, as pions cause the largest share of charged tracks in LHCb events, the overall performance of the same-side pion tagger is expected to lie below the performance of the same-side kaon tagger.

Unfortunately, the same-side pion tagger has not been checked and calibrated in the preparation of this $B^0 \rightarrow J/\psi K_S^0$ analysis. Thus, it will be excluded from the further discussion.

5.3.3 Tagging performance

Of N reconstructed decays, N_R are correctly tagged, N_W are incorrectly tagged, and for N_U candidates no tagging information can be deduced. This allows to define the tagging efficiency ε_{tag} as the ratio of tagged candidates to all candidates,

$$\varepsilon_{\text{tag}} = \frac{N_R + N_W}{N_U + N_R + N_W}, \tag{5.15}$$

and the mistag fraction ω as the fraction of incorrectly tagged over all tagged candidates,

$$\omega = \frac{N_W}{N_R + N_W}. \tag{5.16}$$

As the measured decay rates of candidates tagged as $\bar{B}^0/B^0$ are then given by

$$N_{\bar{B}^0}(t) = (1 - \omega)N_{\bar{B}^0}^{\text{true}}(t) + \omega N_{B^0}^{\text{true}}(t), \tag{5.17a}$$

$$N_{B^0}(t) = (1 - \omega)N_{B^0}^{\text{true}}(t) + \omega N_{\bar{B}^0}^{\text{true}}(t), \tag{5.17b}$$

where $N_{B^0}^{\text{true}}(t)$ $(N_{\bar{B}^0}^{\text{true}}(t))$ is the true decay-time dependent rate of B^0 $(\bar{B}^0)$ decays, a non-vanishing mistag fraction leads to a diluted observed asymmetry,

$$\mathcal{A}_{\text{obs}}(t) = (1 - 2\omega)\mathcal{A}(t) = \mathcal{D}_\omega \mathcal{A}(t). \tag{5.18}$$

Hence, the dilution factor from tagging is given by $\mathcal{D}_\omega = (1 - 2\omega)$. Following the discussion in Sec. 5.1, the effective tagging efficiency ε_{eff} can then be defined as

$$\varepsilon_{\text{eff}} = \varepsilon_{\text{tag}}(1 - 2\omega)^2. \tag{5.19}$$

A perfect tagging procedure implies $\varepsilon_{\text{tag}} = 1$ and $\omega = 0$, and hence $\varepsilon_{\text{eff}} = 1$. While a tagging efficiency $\varepsilon_{\text{tag}} < 1$ only reduces the overall size of the sample that can be used for the *CP* asymmetry measurement, a mistag fraction $\omega > 0$ dilutes the asymmetry by a dilution factor $\mathcal{D}_\omega = 1 - 2\omega$. Therefore, it is necessary to correctly assess and measure the mistag fraction. Additionally, it is important to keep the uncertainty of the mistag fraction as low as possible,

as the uncertainty on the dilution directly propagates to an additional uncertainty on the asymmetry parameters, as has been shown in Sec. 5.1.

Another complication arises from different interaction probabilities of tagging particles and anti-particles with the detector. Hence, both the tagging efficiency and the mistag fraction can depend on the flavour of the signal *B* meson, leading to a further distortion of the measurable *CP* asymmetries. All of this needs to be taken into account in the calibration and performance measurements, which will be presented in Sec. 6.3.

5.3.4 Combination of flavour taggers

As described earlier, each tagging algorithm i provides a tag d_i and a mistag probability estimate η_i of the decision, which depends on the algorithm's neural network response. The neural networks of the opposite-side taggers use several inputs: The signal *B* transverse momentum, the number of pile-up vertices, the number of preselected tagging particle tracks, and geometric and kinematic properties of the tagging particle or of the secondary primary vertex. As the same-side flavour tagging algorithms were not calibrated in preparation of the analysis, they are not used in the combination.

If more than one tagger provides a non-zero tag decision, the tagging decisions are combined into one decision d and one mistag probability estimate η. The combined probability $P(b)$ ($P(\bar{b})$) that the reconstructed signal meson contained a b quark ($\bar{b}$ quark) at production is given by

$$P(b) = \frac{p(b)}{p(b) + p(\bar{b})}, \quad P(\bar{b}) = 1 - P(b), \tag{5.20}$$

where

$$p(b) = \prod_i \left(\frac{1 + d_i}{2} - d_i(1 - \eta_i) \right), \quad p(\bar{b}) = \prod_i \left(\frac{1 - d_i}{2} + d_i(1 - \eta_i) \right). \tag{5.21}$$

Whenever the probability for a $\bar{b}$ quark is higher, i.e. $P(\bar{b}) > P(b)$, the combined tag is $d = +1$ and the mistag probability is $\eta = 1 - P(\bar{b})$, otherwise the combined decision is $d = -1$ with $\eta = 1 - P(b)$. To limit the contribution of tags with poor tagging power, the mistag probabilities of the kaon and the vertex charge tagger must be below 0.46 to be considered in the combination. The performance of the single opposite-side taggers, as well as the performance of the combination is summarised in Tab. 5.1.

Although efforts are expanded to reduce the correlation between taggers, a small correlation leading to a small overestimation of the combined probabilities remains, and needs to be corrected for in the calibration on data. The calibration of the flavour tagging algorithms with the data collected in 2011 will be described in Sec. 6.3.

Tab. 5.1: Flavour tagging performance in terms of the tagging efficiency ε_{tag}, the mistag fraction ω, and the effective tagging efficiency ε_{eff}, for each opposite-side tagger and their combination, as measured in the control channel $B^+ \to J/\psi K^+$ [118].

Tagger	ε_{tag} [%]	ω [%]	ε_{eff} [%]
Muon	5.20 ± 0.04	30.8 ± 0.4	0.77 ± 0.04
Electron	2.46 ± 0.03	30.9 ± 0.6	0.36 ± 0.03
Kaon	17.67 ± 0.08	39.33 ± 0.24	0.81 ± 0.04
Vertex Charge	18.46 ± 0.08	40.31 ± 0.24	0.70 ± 0.04
Combination	33.20 ± 0.09	36.7 ± 0.2	2.35 ± 0.06

5.4 Decay time reconstruction

The decay time t of a particle in its rest frame is given by

$$ t = l/\beta\gamma c = lm/p, \tag{5.22} $$

where m is the particle mass, p is the momentum, and l is the decay length of the particle in the laboratory frame. All of these quantities need to be measured and therefore suffer from experimental uncertainties. In first order, the resolution of the decay length depends on the vertex resolution of the production and the decay vertex of the candidate. Furthermore, the resolution of the reconstructed mass and of the momentum depend on the momentum resolution of the daughter particles. Consequently, the decay time resolution is a complicated function of phase-space, and can depend on the decay time.

5.4.1 Dilution from decay time resolution

For a time-dependent measurement of *CP* asymmetries in oscillating meson systems, decay time resolutions lead to a dilution of the amplitude, which is independent of the additional dilution from incorrectly tagged events [113, 119, 120]. Often, the resolution can be described in terms of a Gaussian function

$$ \mathcal{R}(t - t') = \frac{1}{\sqrt{2\pi\sigma_t^2}} \exp\left(-\frac{(t-t')^2}{2\sigma_t^2}\right) \tag{5.23} $$

where t is the measured decay time, t' is the true decay time, and σ_t is the width of the Gaussian function. A perfect decay time reconstruction implies $\sigma_t \to 0$. Hence, ignoring other experimental effects, like tagging or production asymmetries, and further ignoring that t' can only take positive values, the decay rate distributions $N_{\pm}$, where $+ (-)$ denotes an initial B^0 ($\bar{B}^0$) flavour, are given by

$$
\begin{aligned}
N_{\pm}(t) &\sim \int_{-\infty}^{\infty} e^{-t'/\tau}\left[1 \mp S \sin(\Delta m\, t') \pm C \cos(\Delta m\, t')\right] \cdot \mathcal{R}(t - t')\, dt' \\
&= e^{\frac{\sigma_t^2}{2\tau^2}} e^{-t/\tau}\left(1 \pm e^{-\frac{\Delta m^2 \sigma_t^2}{2}}\left[S \sin\left(\Delta m(t - \sigma_t^2/\tau)\right) - C \cos\left(\Delta m(t - \sigma_t^2/\tau)\right)\right]\right).
\end{aligned}
\tag{5.24}
$$

Then, the resulting observed decay rate asymmetry can be written as

$$
\begin{aligned}
\mathcal{A}_{\text{obs}}(t) &= \frac{N_-(t) - N_+(t)}{N_-(t) + N_+(t)} \\
&= e^{-\frac{\Delta m^2 \sigma_t^2}{2}} \left[S \sin\left(\Delta m (t - \sigma_t^2/\tau) \right) - C \cos\left(\Delta m (t - \sigma_t^2/\tau) \right) \right]
\end{aligned}
\tag{5.25}
$$

Hence, the observed asymmetry is diluted by $\mathcal{D}_{\sigma_t} = e^{-\frac{\Delta m^2 \sigma_t^2}{2}}$ and biased to positive t with an offset σ_t^2/τ. For the typical resolutions at LHCb of $\sigma_t \approx 50\,\text{fs}$, the resulting dilution in the B^0 system lies above 99.9%, while the offset lies in the region of 2 fs. In contrast, a dilution of approximately 65% can be expected in the B_s^0 system, due to its high $\Delta m \approx 17.7\,\hbar/\text{ps}$.

5.4.2 Decay tree fitter

The standard approach for reconstructing decay chains follows a bottom-up strategy, and starts from combining final state candidates to intermediate particles, which are then combined to other intermediate particles of the decay chain. At each vertex, the parameters of the intermediate particles are determined from a χ^2 fit under the constraint that the daughters originate from a common point, hereby only taking into account properties of the daughter particles. Other constraints upstream of the decay vertex do not contribute. Hence, although this 'leaf-by-leaf' fitting is necessary for reconstructing a decay chain, it is not the optimal approach for determining observables needed in the final analysis. The decay tree fitter, which will be presented in this section, offers an alternative approach that overcomes these drawbacks and is therefore often used in the scope of decay time dependent analyses like the CP measurement in $B^0 \to J/\psi K_S^0$.

The decay tree fitter, or decay chain fitter [121], is a method to perform a fit of a complete decay tree with multiple vertices, e.g. $B^0 \to J/\psi K_S^0$ with the subsequent decays of $J/\psi \to \mu^+ \mu^-$ and $K_S^0 \to \pi^+ \pi^-$. It simultaneously determines the decay time, position and momentum parameters and their uncertainties for all intermediate and final particles of the decay chain while fully respecting the correlations among the parameters.

A decay tree, as depicted in Fig. 5.3 for a $B^0 \to J/\psi K_S^0$ decay, is defined by the vertex positions and the momenta of all particles, which represent the degrees-of-freedom, internal constraints, like momentum conservation at each vertex, relations to external reconstruction objects, like tracks and primary vertices, and additional external constraints, like mass hypotheses or constraints on the reconstructed mass of the intermediate particles. Each final state particle is represented by its momentum vector and the mass, which is assigned based on the particle hypothesis of the decay. Each intermediate particle is represented by a four-momentum vector, a decay vertex position, and a decay time parameter $\theta = l/p$. If the intermediate particle is a resonance, like the J/ψ meson, and its expected decay length is much smaller than the vertex resolution of the detector, no decay time is assigned. The global fit to the particle parameters is performed in terms of a Kalman filter or progressive fit [95] rather than a classical χ^2 fit to reduce computational costs.

In the scope of the $B^0 \to J/\psi K_S^0$ analysis, the decay tree fitter is used in different configurations. The decay time of the B^0 candidate, t, results from a decay tree fit where the
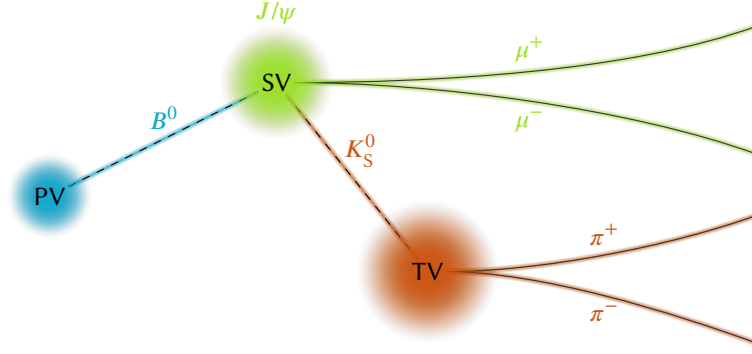
Fig. 5.3: Schematic view of a decay tree for a $B^0 \to J/\psi K_S^0$ decay. Reconstructed tracks of the final state particles ($\pi^\pm, \mu^\pm$) are represented by solid lines, while flight trajectories of the intermediate particles (K_S^0, B^0) are represented by dashed lines. The shaded regions around the primary, secondary, and tertiary vertices (PV, SV, TV) and the flight trajectories illustrate the experimental uncertainties.

momentum vector of the B^0 candidate is constrained to point back to its production vertex. The uncertainty, σ_t, evaluated for each candidate is used as an estimate of the decay time resolution. The reconstructed mass, $m_{J/\psi K_S^0}$, is determined from a decay tree fit where the intermediate J/ψ and K_S^0 particles are constrained to their known masses, in addition to the constraint that the B^0 candidate's momentum vector points back to its production vertex.

5.5 Maximum likelihood method

A data sample consists of n data points $\{x_1, x_2, \ldots, x_n\}$ in the multidimensional observables x. Here, each data point represents a reconstructed $B^0 \to J/\psi K_S^0$ decay candidate that fulfils the selection requirements. Assuming that the distribution corresponds to a probability density function (PDF) $\mathcal{P}(x; \lambda)$, which depends on the vector of parameters λ, the likelihood function $\mathcal{L}(\lambda)$ can be defined as [122–124]

$$\mathcal{L}(\lambda) = \prod_{i=1}^{n} \mathcal{P}(x_i; \lambda).$$ (5.26)

It represents the probability to observe the data at hand when assuming that the PDF $\mathcal{P}(x; \lambda)$ describes the underlying distribution. The maximum likelihood estimators of the parameters $\lambda = (\lambda_1, \lambda_2, \ldots, \lambda_m)$ maximise the likelihood function, and are therefore solutions to the equations

$$\nabla \mathcal{L} = 0.$$ (5.27)

In the presence of multiple local maxima, the highest one is taken. The resulting parameter estimators of the maximum likelihood method are unbiased, and the resulting $\mathcal{P}(x_i, \lambda_f)$ represents a fit of the PDF to the data.

For most problems, the maximum condition cannot be solved analytically, and therefore numerical iterative procedures are needed. Though, as the probability $\mathcal{P}(\boldsymbol{x}_i; \lambda)$ of individual events can be small, most numerical methods use the logarithm of the likelihood

$$\ln \mathcal{L}(\lambda) = \sum_i^n \ln \left(\mathcal{P}(\boldsymbol{x}_i; \lambda) \right) . \tag{5.28}$$

This does not affect the properties of the parameter estimation, as the logarithm is a strictly monotonically increasing function. In practice, the minimisation of the negative log-likelihood (NLL) is preferred, to allow the usage of commonly used and thoroughly tested algorithms for function minimisation, e.g. that are provided in the MINUIT minimisation package [125, 126]. Besides function minimisation, the MINUIT package permits the calculation of parameter uncertainties by estimating the curvature of the likelihood minimum [127].

While the maximum likelihood method itself offers many advantages, its usage requires a detailed modelling of the dataset in terms of PDFs. These need to accurately describe the distributions of the different species in the dataset, like signal and background components. For instance, the signal component, which describes the true $B^0 \to J/\psi K^0_S$ decays, needs to account for experimental influences on the measured distributions, like tagging, decay time resolution effects, or the production asymmetry, thus allowing for an unbiased estimation of the parameters.

5.6 Initial results with 2010 data

In a first attempt to measure $S_{J/\psi K^0_S}$ with the LHCb experiment, the dataset collected in 2010, which corresponds to $35\,\mathrm{pb}^{-1}$ of pp collisions at $\sqrt{s} = 7\,\mathrm{TeV}$, is analysed. A total of $28\,000$ $B^0 \to J/\psi K^0_S$ candidates are reconstructed from J/ψ and K^0_S candidates. The former are formed from pairs of oppositely charged tracks that have a transverse momentum of more than $500\,\mathrm{MeV}/c$ and are consistent with the muon hypothesis, while the latter are a result of combining two oppositely charged tracks, where both are either long or downstream tracks and are compatible with the pion hypothesis. Furthermore, the decay length of the K^0_S with respect to the B^0 decay vertex must be more significant than five standard deviations.

The statistical analysis of the sample is implemented via an unbinned maximum-likelihood fit to the distributions of the reconstructed mass m, the decay time t, the tag d, and the mistag estimate η of the candidates. Both, η and d, are derived from the combination of the opposite-side taggers only, and the calibration is performed with the $B^+ \to J/\psi K^+$ channel [128]. Additionally, a cross-check using the $B^0 \to J/\psi K^{*0}$ channel is performed. In the fit, $C_{J/\psi K^0_S}$ is fixed to 0 and Δm_d to its value as measured by other experiments. Distributions of the reconstructed mass and decay time are shown in Fig. 5.4.

Using 280 tagged and 1046 untagged signal candidates, the analysis yields

$$S_{J/\psi K^0_S} = 0.53 \pm^{0.28}_{0.29} \,(\text{stat.}) \pm 0.05\,(\text{syst.}) ,$$

where the systematic uncertainty is dominated by the uncertainty on the tagging calibration. The result is compatible with the world average, and dominated by the statistical uncertainty.
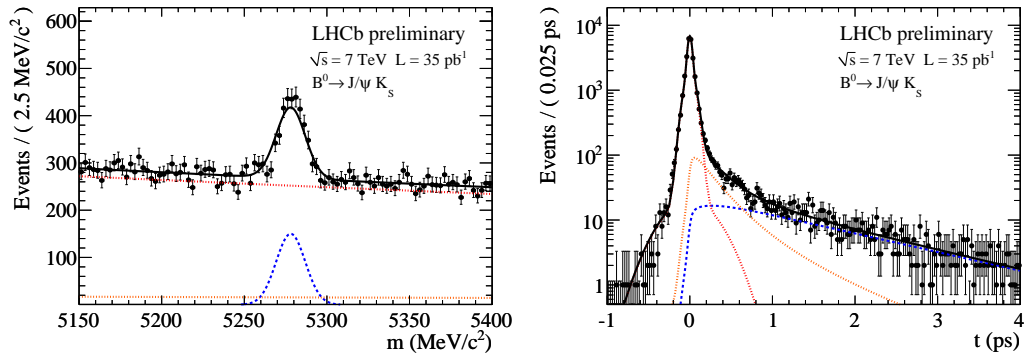
Fig. 5.4: Distribution of the reconstructed mass (left) and the decay time (right) of $B^0 \to J/\psi K_S^0$ candidates [129]. The solid curve (black) is the projection of the full PDF, which is overlayed onto the data points together with the signal component (dashed, blue), the prompt background (dash-dotted, red), and the long-lived background (dotted, orange).

In Fig. 5.5, the resulting decay time dependent raw asymmetry is shown, which describes all fit components. As the raw asymmetry is diluted by $S/(S + B)$, where S denotes the signal and B the background yield, an additional dilution of the amplitude can be observed at small decay times, where the background component dominates. This first attempt to a measurement of CP violation in $B^0 \to J/\psi K_S^0$ by LHCb is more thoroughly documented in Ref. [129].

Although the result is only significant at the 1.8σ level, it represents the first step to a measurement of $S_{J/\psi K_S^0}$ with LHCb and gives insight for the following iterations of this analysis with larger datasets. Naively extrapolating the result to the 2011 dataset of $1\,\text{fb}^{-1}$, a statistical uncertainty of approximately 0.06 can be estimated, which would still exceed the systematic uncertainties quoted for the 2010 measurement. Furthermore, to reduce inefficient computing and storage usage, it is sensible to reduce the portion of obvious backgrounds. For instance, by requiring a minimum decay time of 0.2 ps, most of the prompt background can be removed, as can be seen in the decay time distribution shown in Fig. 5.4. The same argument holds for the trigger lines, as the data taking conditions in 2011 require the use of decay time biasing trigger lines, e.g. which require a minimal flight distance between the J/ψ candidate and the primary vertices. Still, decay time unbiased trigger lines and selections, at a reduced rate, remain crucial for studies of the decay time resolution and especially for studies of the decay time dependent selection effects, so-called decay time acceptances, which are introduced by the biased trigger lines.
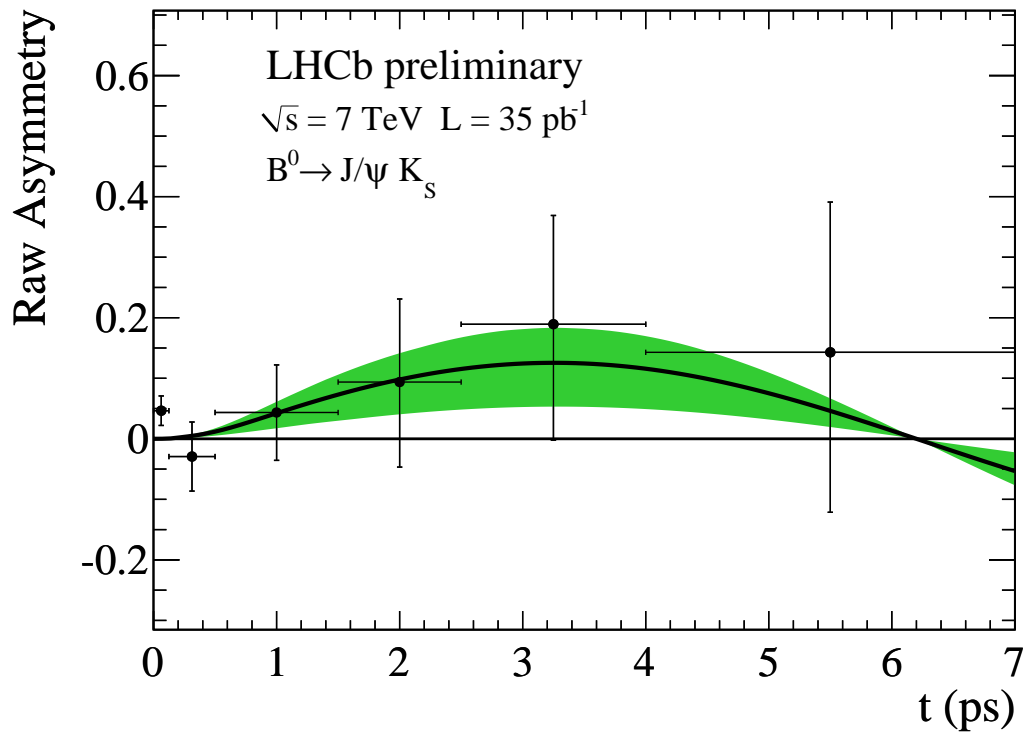
Fig. 5.5: Raw asymmetry between the decay time distributions of $B^0 \rightarrow J/\psi K_S^0$ candidates tagged as $\bar{B}^0$ and the ones tagged as B^0 [129]. The solid curve is the projection of the full PDF, the green band corresponds to the one standard deviation statistical error.

6 Preparatory Studies

In the previous chapter, the different steps required for a measurement of *CP* violation in $B^0 \rightarrow J/\psi K_S^0$ decays have been presented, together with some of the most relevant tools and methods used in this analysis: the flavour tagging algorithms, the decay tree fitter, and the maximum likelihood method. In this chapter, the focus lies on a more detailed description of each relevant step performed in preparation of the measurement, starting from the choice of datasets and the corresponding reconstruction, selection, and trigger requirements. Next, the calibration of the flavour tagging algorithms is presented, followed by a brief description of the production asymmetry measurement. Then, the composition of the background is analysed. The chapter closes with a discussion of the selection efficiencies as a function of decay time and the measurement of the decay time resolution of reconstructed $B^0 \rightarrow J/\psi K_S^0$ candidates.

6.1 Datasets

The analysis is performed using a dataset recorded in 2011 by the LHCb detector at a centre-of-mass energy of $\sqrt{s} = 7\,\text{TeV}$. Several data subsamples as well as simulated samples are used in the scope of the analysis for preparatory studies and the verification of the analysis strategy.

6.1.1 LHCb data of 2011

The full dataset recorded by LHCb in 2011 consists of the LHCb runs 87666 to 104263 and equates to an integrated luminosity of $1.025\,\text{fb}^{-1}$, of which $0.590\,\text{fb}^{-1}$ were recorded with positive magnet polarity (magnet down) and $0.435\,\text{fb}^{-1}$ with negative magnet polarity (magnet up). The main data sample used in the analysis is a subset of this sample, after applying trigger, stripping, and selection requirements, which will be presented in Sec. 6.2.

The raw dataset is processed with BRUNEL v41r1 for the track reconstruction (Reco12) and DAVINCI v29r1 for the Stripping (Stripping17). The resulting stripped dataset is subsequently processed with DAVINCI v29r3p1 to create tuples suited for an analysis with the ROOT data analysis framework [98]. These tuples include flavour tagging information provided by the FlavourTagging package v12r7 and re-fits of the reconstructed decay time and mass of each B^0 candidate using the DecayTreeFitter.

6.1.2 Simulated datasets

Simulated datasets are a perfect testbed for the analysis procedures. They are used to perform sanity checks of the analysis strategy and allow the study of effects that could influence the

measurement. Two categories of simulated data are used: Fully simulated Monte Carlo (MC) datasets and Toy Monte Carlo (ToyMC) datasets.

Fully simulated datasets are produced with the Monte Carlo algorithms and packages embedded in the LHCb simulation framework, see Sec. 4.5.3. These samples are centrally produced by the collaboration and adapted to the needs of the analysts, e.g. the simulated beam settings are changed according to the different data taking periods. The samples contain simulations of full *pp* collisions and interactions of the resulting particle showers with the detector material. Hence, the production of these samples is computing intensive and is expensive in terms of storage space.

Toy Monte Carlo samples, on the other hand, consist of pseudo-experiments with a comparatively fast simulation time and small storage needs. In contrast to the fully simulated samples, their production mechanisms are not based on a full description of particle interactions, but on the form of the phenomenological distributions. This type of simulation is extensively used throughout the analysis, in particular for the estimation of systematic uncertainties.

6.2 Selection requirements

As described in Sec. 6.1.1, the recorded LHCb dataset is reduced to a manageable size before being analysed. The first reduction is achieved through trigger requirements, which are applied in the course of data taking, see Sec. 4.4. Only potentially interesting events are selected for further analysis. In a next step, the Stripping performs a pre-selection with loose requirements for an efficient reconstruction and selection of $B^0 \to J/\psi K_S^0$ decays, with subsequent decays of $J/\psi \to \mu^+\mu^-$ and $K_S^0 \to \pi^+\pi^-$, while rejecting background. Additional offline processing steps further reduce the sample by applying tighter requirements.

6.2.1 Stripping and offline selection

The selection strategy is inspired by selections developed in the course of other analyses of *B* meson decays to final states containing a *J/ψ* meson, like the measurement of time-dependent *CP* violation in $B_s^0 \to J/\psi\phi$ decays [130, 131]. The stripping selection applies loose requirements to the full dataset to create a sub-sample enriched with decays of $B^0 \to J/\psi K_S^0$. In the offline selection, some of the requirements applied in the stripping are further tightened, and additional cuts are introduced. The requirements applied in the stripping and offline selection are presented in Tab. 6.1. The resulting overall requirements will be summarised in the following paragraphs.

The reconstruction of $B^0 \to J/\psi K_S^0$ decay candidates is based upon the combination of a $J/\psi \to \mu^+\mu^-$ decay with a $K_S^0 \to \pi^+\pi^-$ decay. Only charged tracks with a track fit χ^2/ndf of less than 4 are considered, where ndf is the number of degrees of freedom of the fit.

The *J/ψ* candidates are formed from two oppositely-charged tracks with $p_T > 500$ MeV/c and particle identification information that favours the muon over the pion hypothesis. Only pairs of long tracks (see Sec. 4.5.1 for the definition of track types) whose distance of closest approach fit have a χ^2 of less than 20 are considered. Muon tracks that fulfil these demands must further form a common vertex with a fit χ^2/ndf < 11 and a *J/ψ* candidate with an invariant mass in the range of 3035–3160 MeV/c^2.

The K^0_S candidates are reconstructed from two-oppositely charged pions, each with a momentum of at least 2000 MeV/c and a distance of closest approach fit with a χ^2 of less than 25. In LHCb, K^0_S mesons with their comparably long lifetime $\mathcal{O}(0.1\,\mathrm{ns})$ mostly decay outside the acceptance of the VELO detector. Hence, K^0_S candidates are either reconstructed from pairs of long tracks (long K^0_S candidate) or of downstream tracks (downstream K^0_S candidate). Candidates formed from a long and a downstream pion track would enlarge the data set by less than 2% and are therefore omitted. As the downstream K^0_S candidate reconstruction resorts back to less precisely measured tracks, requirements for downstream and long K^0_S candidates differ. To diminish the contribution of tracks originating directly from a *pp* interaction, the approximate χ^2 of the impact parameter, $\chi^2_{\mathrm{IP,PV}}$, of the pions to any primary vertex is required to lie above 9 (4) for long (downstream) K^0_S candidates. Here, $\chi^2_{\mathrm{IP,vtx}}$ (with vtx = PV) represents the difference of the χ^2 between the vertex fit with and without the particle's track taken into account. For a vertex formed from an infinite number of tracks, $\chi^2_{\mathrm{IP,vtx}}$ is equivalent to the χ^2 of an impact parameter fit. Furthermore, the pion tracks must form a common vertex with a fit χ^2/ndf < 20 and an invariant mass within the range of 485.6–509.6 MeV/c^2 (long K^0_S candidates) or 476.6–518.6 MeV/c^2 (downstream K^0_S candidate). The fitted decay length significance of the resulting K^0_S candidate with respect to the primary vertex with the smallest impact parameter is required to be significant at a 5σ level.

Finally, the B^0 candidates are formed from combinations of *J/ψ* and K^0_S candidates that form a vertex with a vertex χ^2/ndf < 10 and an invariant mass in the range 5150–5450 MeV/c^2. Resulting B^0 candidates are associated to the PV with the lowest impact parameter $\chi^2_{\mathrm{IP,PV}}$, which is required to not exceed the value of 20. To reduce the rate of incorrect PV association the second smallest impact parameter $\chi^2_{\mathrm{IP,vtx}}$ with respect to all other PVs must be larger than 50. Background contributions from K^{*0} mesons that are mis-identified as K^0_S candidates are reduced by requiring a decay time significance of the K^0_S candidate with respect to the B^0 decay vertex larger than 5.

Prompt background candidates, i.e. candidates that are formed from random tracks, *J/ψ* mesons, and K^0_S mesons that originate from a PV and not from a *B* decay, are omitted to a large extent by requiring a decay time of the B^0 candidate of more than 0.2 ps. The resulting sample is further referred to as "detached" and is used in the nominal analysis. However, studies of decay time related effects, such as acceptances and resolutions, require samples with the full decay time range down to negative reconstructed decay times. Therefore, an additional pre-selection, identical to the fore-mentioned selection but without the decay time requirement, is run in the stripping, but is subject to a random rejection of 70% of the events. The resulting sample will be referred to as "prescaled".

6.2.2 Additonal requirements

Additional requirements are applied to the output of the decay tree fit (see Sec. 5.4.2), which is used for a better determination of the decay time and the reconstructed mass, and to the output of the flavour tagging algorithms. The selection criteria are summarised in Tab. 6.2 and are explained here. However, selection requirements in the scope of auxiliary studies might differ and will be discussed in the appropriate sections.

Tab. 6.1: Stripping and selection criteria for $B^0 \to J/\psi\,K_S^0$ decays. Requirements are based on the track fits' χ^2_{track}/ndf, the difference $\Delta \log L_{\mu\pi}$ of likelihoods of the μ and the π hypotheses as provided by the particle identification system, the distance of closest approach (DOCA), the decay length significance (DLS), the impact parameter $\chi^2_{\text{IP,vtx}}$ of candidates' extrapolated flight path with respect to a vertex, e.g. the best PV and the next best PV (the PVs with the lowest and second lowest $\chi^2_{\text{IP,PV}}$, respectively). Here, the $\chi^2_{\text{IP,vtx}}$ is calculated as the difference of the χ^2 of the vertex fit with and without inclusion of the particle's track(s).

Selection step		Requirement	Stripping	Selection	Unit
$J/\psi \to \mu^+\mu^-$	$\mu^\pm$ candidates	χ^2_{track}/ndf	< 5	< 4	
		$\Delta \log L_{\mu\pi}$	> 0	> 0	
		p_{T}	> 500	> 500	MeV/c
		χ^2_{DOCA}/ndf	< 20	< 20	
	J/ψ candidates	χ^2_{vtx}/ndf	< 16	< 11	
		$m_{\mu^+\mu^-}$	> 3017	> 3035	MeV/c^2
			< 3177	< 3160	MeV/c^2
$K_S^0 \to \pi^+\pi^-$ (long)	$\pi^\pm$ candidates	χ^2_{track}/ndf	< 5	< 4	
		p	> 2000	> 2000	MeV/c
		χ^2_{DOCA}/ndf	< 25	< 25	
		$\min(\chi^2_{\text{IP,PV}})$	> 9	> 9	
	K_S^0 candidates	χ^2_{vtx}/ndf	< 20	< 20	
		DLS$_{\text{best PV}}$	> 5	> 5	
		$m_{\pi^+\pi^-}$	> 463	> 486	MeV/c^2
			< 533	< 510	MeV/c^2
$K_S^0 \to \pi^+\pi^-$ (downstream)	$\pi^\pm$ candidates	χ^2_{track}/ndf	< 5	< 4	
		p	> 2000	> 2000	MeV/c
		χ^2_{DOCA}/ndf	< 25	< 25	
		$\min(\chi^2_{\text{IP,PV}})$	> 4	> 4	
	K_S^0 candidates	χ^2_{vtx}/ndf	< 20	< 20	
		DLS$_{\text{best PV}}$	> 5	> 5	
		$m_{\pi^+\pi^-}$	> 434	> 477	MeV/c^2
			< 562	< 519	MeV/c^2
$B^0 \to J/\psi\,K_S^0$	B^0 candidates	$m_{\mu\mu\pi\pi}$	> 5150	> 5170	MeV/c^2
			< 5450	< 5420	MeV/c^2
		χ^2_{vtx}/ndf	< 10	< 10	
		$\chi^2_{\text{IP,best PV}}$	–	< 20	
		$\chi^2_{\text{IP,next best PV}}$	–	> 50	
		t	> 0.2	> 0.2	ps
	K_S^0 candidates	t/σ_t	–	> 5	

The reconstructed mass observable $m_{J/\psi K_S^0}$ is computed from a decay tree fit, as described in Sec. 5.4.2. If not stated otherwise, the reconstructed mass of the candidates is required to be in the range of 5230–5330 MeV/c^2. The decay time t of the B^0 candidates is computed from a decay tree fit under the constraint that the candidate's momentum points back to its associated primary vertex. Candidates are only kept if the fit χ^2/ndf is less than 5. If multiple candidates in an event are reconstructed, that with the best decay tree fit quality (lowest χ^2/ndf) is chosen. The fit uncertainty on t is used as an estimate of the decay time resolution σ_t, and must not exceed 0.2 ps.

Tab. 6.2: Additional offline requirements on observables computed by the decay tree fitter and the flavour tagging algorithms. If multiple candidates per event exist that with the lowest χ^2 of the decay tree fit is kept.

Requirement	Value	
Reconstructed mass $m_{J/\psi K_S^0}$	> 5230	MeV/c^2
	< 5330	MeV/c^2
Decay time t	> 0.3	ps
Decay time uncertainty σ_t	< 0.2	ps
Decay tree fitter χ^2	< 5	
Opposite-side tag d	$\neq 0$	

6.2.3 Trigger requirements

In principle, any further requirement for events to have been triggered by a specific subset of the available trigger algorithms reduces the sample size and consequently could as well reduce the statistical precision of the measurement. However, each involved trigger algorithm comes with its own kinematic requirements, leading to non-trivial inefficiencies in phase-space which need to be studied and accounted for in the analysis.

The decay of the J/ψ meson into two muons at the displaced B^0 decay vertex provides a clean signature for triggering events with $B^0 \to J/\psi K_S^0$, as the muon system allows for fast and efficient trigger implementations. In the time-dependent measurement of $B^0 \to J/\psi K_S^0$ decays, it is desirable to minimise the number of effects that introduce decay time acceptances. As the decay vertex of the J/ψ candidate strongly affects the decay time, only trigger lines are considered that make use of the decay signature of the J/ψ meson. Furthermore, events are only kept, if the reconstructed $B^0 \to J/\psi K_S^0$ decay, in particular the $J/\psi \to \mu^+\mu^-$ decay, meets the trigger requirements.

In HLT1, the choice is limited to the `DiMuonHighMass` trigger line, which requires two oppositely-charged muon tracks that fulfil the kinematic requirements as quoted in Tab. 6.3 and that form a common vertex. This trigger line does not introduce a decay time acceptance. In HLT2, the `DiMuonJpsi` and the `DiMuonDetachedJPsi` trigger lines are considered. Their requirements are summarised in Tab. 6.4. The `DiMuonJpsi` line does not introduce decay time acceptances, but has a prescale of 20% leading to a stern rate reduction. In contrast, the `DiMuonDetachedJPsi` line demands a flight distance χ^2_{FD}/ndf > 9 of the J/ψ candidate with respect to the primary vertices, leading to a non-trivial decay time acceptance of the B^0

candidates. These choices result in two trigger combinations: The *decay time biased* triggers require `DiMuonHighMass` in HLT1 and `DiMuonDetachedJPsi` in HLT2, and the *decay time unbiased* triggers require `DiMuonHighMass` in HLT1 and `DiMuonJpsi` in HLT2.

Tab. 6.3: Requirements of the HLT1 trigger line.

Requirement	`DiMuonHighMass`
L0 decision	`L0Muon` ∨ `L0DiMuon`
$\mu^{\pm}$ transverse momentum	$> 0.5\,\text{GeV}/c$
$\mu^{\pm}$ momentum	$> 6.0\,\text{GeV}/c$
$\mu^{\pm}$ $\chi^2_{\text{track}}/\text{ndf}$	< 4
$\mu^+\mu^-$ distance of closest approach	$< 0.2\,\text{mm}$
$\chi^2_{\text{vtx}}/\text{ndf}$	< 25
$m_{\mu^+\mu^-}$	$> 2.7\,\text{GeV}/c^2$

Tab. 6.4: Requirements of the HLT2 trigger lines.

Requirement	`DiMuonJpsi`	`DiMuonDetachedJPsi`
$\mu^{\pm}$ $\chi^2_{\text{track}}/\text{ndf}$	< 5	< 5
Vertex $\chi^2_{\text{vtx}}/\text{ndf}$	< 25	< 25
$m_{\mu^+\mu^-}[\text{GeV}/c^2]$	3.77 ± 0.12	3.77 ± 0.12
Flight distance $\chi^2_{\text{FD}}/\text{ndf}$	–	> 9
Pre-scale	0.2	–

6.2.4 Nominal dataset

The choice of selection and trigger requirements results in multiple sub-samples which can be used for different auxiliary studies. The nominal sample, which is used in the final measurement, consists of candidates selected by the detached stripping line and triggered by the biased trigger lines. The decay time t of the candidates must lie in the range 0.3–$18.3\,\text{ps}$. Finally, candidates are only considered for the final analysis if the opposite-side flavour tagging algorithms provide a prediction for the production flavour of the B^0 candidate. These requirements leave more than 65% of all available stripped and tagged signal candidates for the final analysis. Other sub-samples used in preparatory studies will be introduced in the context of the particular study.

It is important to note, that each sub-sample is further divided into a downstream and a long sample depending on whether the B^0 candidate was reconstructed from a downstream or a long K_S^0, respectively. As these candidates have different reconstructed mass and decay time resolutions, they need to be studied separately. The mass distributions of each the downstream and the long track sample after applying the full selection, but including both the tagged and untagged candidates, are shown in Fig. 6.1. A likelihood fit to these mass distributions yields a total of approximately 25 000 signal and 6500 background candidates.
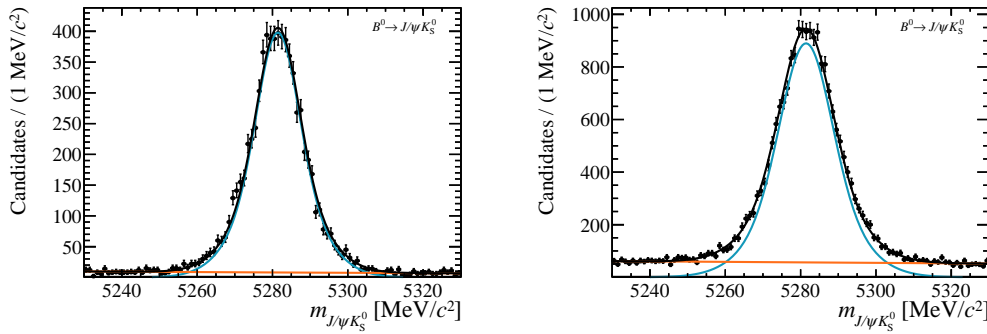
Fig. 6.1: Mass distribution in the long (left) and downstream (right) sample after applying the full selection, but including both the tagged and untagged candidates. Superimposed is the projection of the fitted mass PDF (black), with the signal component (blue) modelled by a double Gaussian function and the background (orange) modelled by an exponential.

6.3 Flavour tagging studies

The commonly used flavour tagging strategies at LHCb have been described in Sec. 5.3. In this section, the flavour tagging strategy specific to the measurement of *CP* violation in $B^0 \to J/\psi K_S^0$ decays, as well as the necessary calibration and performance studies conducted with the 2011 dataset are summarised. A more thorough description of these studies that have been performed by LHCb's Flavour Tagging group is given in Ref. [116].

6.3.1 Flavour tagging strategy

Of all the available tagging algorithms, the opposite-side taggers as well as the same-side pion tagger, and in particular their combination, are eligible for the *CP* measurement in $B^0 \to J/\psi K_S^0$ decays. However, at the time of the analysis, no calibration of the same-side tagging algorithm was available. Therefore, the choice of taggers is limited to the combination of the opposite-side flavour taggers.

The most efficient usage of the information provided by the flavour tagging algorithms, is to use the combined tag d and mistag estimate η of the opposite-side taggers: Instead of using one global mean mistag fraction or a specific number of mean mistag fractions in categories of η, the mistag fraction ω is extracted on an event-by-event basis from the combined per-event mistag prediction of the opposite-side taggers. First, a mistag correction function $\omega(\eta)$ must be determined using self-tagging control channels like $B^+ \to J/\psi K^+$.

6.3.2 Calibration of the opposite-side taggers

For each reconstructed candidate, each opposite-side tagging algorithm i provides a tag d_i and an associated mistag probability estimate η_i, as shown in Fig. 6.2. These single tagger responses are calibrated in a fit by using the measured mistag fraction ω in the self-tagging decay channel $B^\pm \to J/\psi K^\pm$, which follows from comparing the tag d_i with the "true" tag d_i^{true}
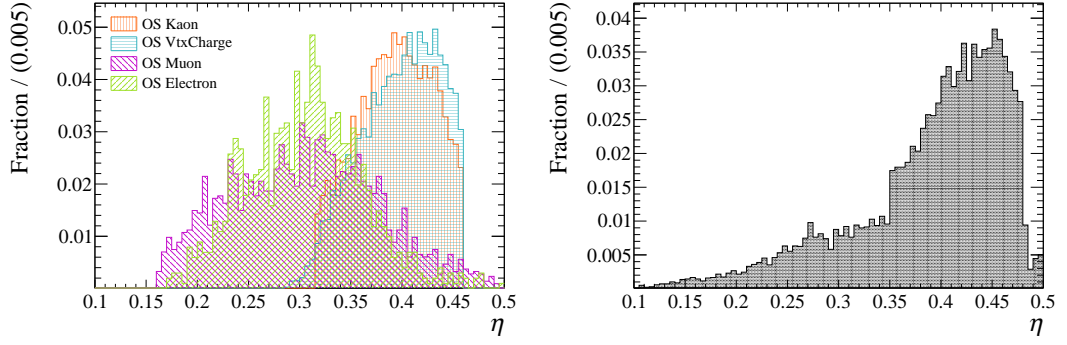
Fig. 6.2: Distribution of the per-event mistag estimate η of the single opposite-side taggers (left, normalised for each tagger) and of the combined opposite-side taggers (right) for $B^0 \to J/\psi K^0_S$ candidates.

defined by the charge of the final state K^+ or K^-. A linear dependence between the measured and the predicted mistag fraction of the signal is observed in data, and is parametrised as

$$\omega(\eta) = p_0 + p_1 \left(\eta - \langle \eta \rangle\right), \tag{6.1}$$

where p_0 and p_1 are parameters of the fit and $\langle \eta \rangle$ is the average predicted mistag fraction for the signal candidates in the particular channel of interest. A perfect calibration implies $p_1 = 1$ and $p_0 = \langle \eta \rangle$.

While the $\langle \eta \rangle$ parameter is calculated from the background subtracted distributions, the other parameters are attained through an unbinned maximum likelihood fit to the reconstructed mass, tagging decision, and predicted mistag probability η. In a first step, each single opposite-side tagging algorithm is calibrated individually, where the largest correction is applied for the vertex charge tagger. Then, the combined mistag probability prediction is corrected for using the same linear model. This additional calibration corrects for neglecting the correlation among the taggers in the combination of the taggin information. For a more detailed description of the combination see Sec. 5.3.4.

The resulting parameters for the combined opposite-side tagging output are

$$\begin{aligned}
p_1 &= 1.035 \pm 0.021 \,(\text{stat.}) \pm 0.012 \,(\text{syst.}), \\
p_0 &= 0.392 \pm 0.002 \,(\text{stat.}) \pm 0.009 \,(\text{syst.}), \\
\langle \eta \rangle &= 0.391,
\end{aligned} \tag{6.2}$$

with a correlation coefficient of $\rho(p_0, p_1) = 0.13$. The systematic uncertainties are estimated by repeating the calibration procedure on other control channels, like $B^0 \to J/\psi K^{*0}$ and $B^0 \to D^{*-} \mu^+ \nu_\mu$. As these channels represent flavour specific decays but are not self-tagging, the number of unmixed candidates, N_{unmixed}, for which tag decision and decay flavour agree, and the number of mixed candidates, N_{mixed}, for which tag decision and decay flavour disagree, are compared as function of decay time t. Due to B^0–$\bar{B}^0$ mixing, this results in the mixing asymmetry

$$\mathcal{A}_{\text{mix}}(t) = \frac{N_{\text{unmixed}}(t) - N_{\text{mixed}}(t)}{N_{\text{unmixed}}(t) + N_{\text{mixed}}(t)} = (1 - 2\omega) \cos \Delta m_d t, \tag{6.3}$$

which is diluted by the mistag fraction only, as *CP* violation plays no significant role in these decays. The resulting calibration functions measured in $B^+ \to J/\psi K^+$ and $B^0 \to J/\psi K^{*0}$ are shown in Fig. 6.3. Other systematic uncertainties originate from differences in calibration parameters measured for different run periods and magnet polarities. The largest systematic uncertainty arises from the dependence on the *B* production flavour.
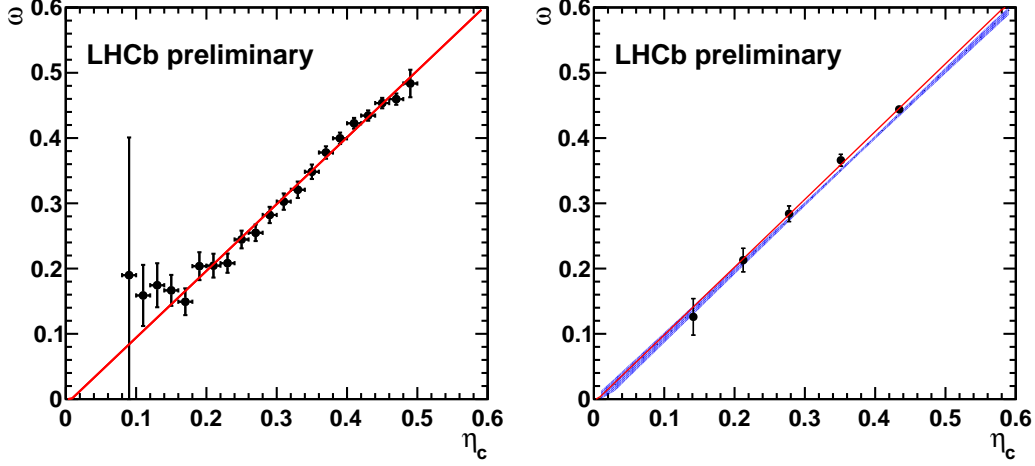

Fig. 6.3: Dependence of the measured mistag fraction ω on the predicted mistag fraction $\eta_c = \eta$ for $B^+ \to J/\psi K^+$ candidates (left) and $B^0 \to J/\psi K^{*0}$ candidates (right) after background subtraction. In each plot, a fit of the linear calibration model in the specific channel is superimposed (red). Additionally, in the right plot, the $B^+ \to J/\psi K^+$ calibration function is superimposed as shaded, blue area, which corresponds to the 1σ error band. Taken from Ref. [118].

6.3.3 Flavour tagging asymmetries

The tagging calibration measurements indicate that the performance of the opposite-side flavour tagging algorithms depends on the initial flavour of the B^0 meson. This is mainly related to the different interaction probabilities of the charged decay products of the tagging *B* hadron with the detector material, e.g. of K^+ and K^- which are used by the opposite-side kaon tagger. These differences can result in flavour dependent tagging efficiencies ε_{tag} and mistag fractions ω. Concerning the difference in tagging efficiencies, a negligible difference of

$$\Delta\varepsilon_{\text{tag}} = \varepsilon_{\text{tag}}^{\bar{B}} - \varepsilon_{\text{tag}}^{B} = 0.000 \pm 0.001 \tag{6.4}$$

is measured in $B^+ \to J/\psi K^+$ decays. For the mistag fraction, two calibration functions similar to Eq. (6.1) are needed,

$$\begin{aligned}
\omega^B(\eta) &= p_0^B + p_1^B \left(\eta - \langle\eta\rangle\right), \\
\omega^{\bar{B}}(\eta) &= p_0^{\bar{B}} + p_1^{\bar{B}} \left(\eta - \langle\eta\rangle\right).
\end{aligned} \tag{6.5}$$

The parameters p_i^B and $p_i^{\bar{B}}$, with $i \in \{0, 1\}$, can be expressed in terms of the mean parameters p_i and the differences Δp_i as

$$p_i^B = p_i + \frac{\Delta p_i}{2}, \quad p_i^{\bar{B}} = p_i - \frac{\Delta p_i}{2}.$$

(6.6)

The differences are measured in $B^+ \to J/\psi K^+$ decays as

$$\begin{aligned}
\Delta p_0 = p_0^B - p_0^{\bar{B}} &= 0.011 \pm 0.003, \\
\Delta p_1 = p_1^B - p_1^{\bar{B}} &= 0.06 \pm 0.04.
\end{aligned}$$

(6.7)

While the value for Δp_1 is in good agreement with 0, a significant difference of p_0 for B and $\bar{B}$ is observed, and measurements in other channels like $B^0 \to J/\psi K^{*0}$ support this finding. Hence, the parametrisations for the mistag calibration functions that incorporate Δp_0 are used,

$$\begin{aligned}
\omega^B(\eta) &= p_1 (\eta - \langle \eta \rangle) + p_0 + \frac{\Delta p_0}{2}, \\
\omega^{\bar{B}}(\eta) &= p_1 (\eta - \langle \eta \rangle) + p_0 - \frac{\Delta p_0}{2},
\end{aligned}$$

(6.8)

while the difference Δp_1 is neglected. As now differences in mistag fraction are correctly considered in the calibration, the systematic uncertainty of the p_0 parameter is reduced, so that

$$\begin{aligned}
p_1 &= 1.035 \pm 0.021 \, \text{(stat.)} \pm 0.012 \, \text{(syst.)}, \\
p_0 &= 0.392 \pm 0.002 \, \text{(stat.)} \pm 0.008 \, \text{(syst.)}, \\
\langle \eta \rangle &= 0.391.
\end{aligned}$$

(6.9)

These values of the calibration parameters will be used throughout the analysis. Varying tagging performances between different channels is already accounted for in the systematic uncertainties of the calibration parameters.

6.3.4 Tagging performance in $B^0 \to J/\psi K_S^0$

The tagging performance in $B^0 \to J/\psi K_S^0$ decays in terms of the tagging efficiency ε_{tag}, the dilution $\mathcal{D}_\omega = (1 - 2\omega)$, and the effective tagging efficiency ε_{eff}, as defined in Sec. 5.3.3, is estimated using the nominal dataset, including both the tagged and the untagged sub-samples. For this study, asymmetries in the tagging efficiency and mistag probabilities, as described in the previous section, are ignored. In a simultaneous, unbinned maximum likelihood fit to the reconstructed mass, the yields of untagged and tagged candidates are measured, leading to an estimated tagging efficiency of

$$\varepsilon_{\text{tag}} = (32.65 \pm 0.31)\%.$$

(6.10)

To determine the effective tagging efficiency ε_{eff},

$$\varepsilon_{\text{eff}} = \varepsilon_{\text{tag}} \mathcal{D}_{\omega,\text{eff}}^2,$$

(6.11)

the effective dilution $\mathcal{D}_{\omega,\text{eff}}$ needs to be calculated from the per-event mistag fraction estimates $\omega(\eta)$ of each signal candidate through

$$\mathcal{D}^2_{\omega,\text{eff}} = \langle \mathcal{D}^2_\omega \rangle = \int \; d\eta \, p(\eta) \big(\mathcal{D}_\omega(\eta) \big)^2 \quad = \frac{1}{N} \sum_i \big(1 - 2\omega(\eta_i) \big)^2 , \tag{6.12}$$

where $p(\eta)$ is the distribution of mistag fraction estimates. With the choice of the linear calibration function in Eq. (6.1), the uncertainty on $\langle \mathcal{D}^2_\omega \rangle$ can be calculated using linear Gaussian error propagation, as

$$\sigma^2_{\langle \mathcal{D}^2_\omega \rangle} = \left(\frac{\partial \langle \mathcal{D}^2_\omega \rangle}{\partial p_0} \sigma_{p_0} \right)^2 + \left(\frac{\partial \langle \mathcal{D}^2_\omega \rangle}{\partial p_1} \sigma_{p_1} \right)^2 + 2\rho(p_0, p_1) \frac{\partial \langle \mathcal{D}^2_\omega \rangle}{\partial p_0} \frac{\partial \langle \mathcal{D}^2_\omega \rangle}{\partial p_1} , \tag{6.13}$$

with

$$\frac{\partial \langle \mathcal{D}^2_\omega \rangle}{\partial p_0} = \frac{1}{N} \sum_i -4(1 - 2\omega_i), \tag{6.14a}$$

$$\frac{\partial \langle \mathcal{D}^2_\omega \rangle}{\partial p_1} = \frac{1}{N} \sum_i -4(1 - 2\omega_i)(\eta_i - \langle \eta \rangle). \tag{6.14b}$$

Here, σ_{p_0} and σ_{p_1} are the combined statistical and systematic uncertainties of the tagging calibration parameters p_0 and p_1, respectively. The uncertainty on the effective dilution is then given by

$$\sigma^2_{\mathcal{D}_{\omega,\text{eff}}} = \frac{1}{(2\mathcal{D}_{\omega,\text{eff}})^2} \sigma^2_{\langle \mathcal{D}^2_\omega \rangle} . \tag{6.15}$$

The determination of the effective dilution requires the knowledge of the η distribution of the signal. For this, the sPlot method is applied [132]. A fit to the mass distribution is used to extract signal weights, as the reconstructed mass is a good observable to discriminate signal and background components. Then, the weights are applied to the distributions in other observables like η, which are not correlated with the discriminating observables. As a result, one arrives at a signal distribution in η. Plugging this distribution into Eq. (6.13) allows to measure the effective dilution $\mathcal{D}_{\omega,\text{eff}}$ of the signal as

$$\mathcal{D}_{\omega,\text{eff}} = 0.270 \pm 0.015 , \tag{6.16}$$

corresponding to an effective mistag fraction of $\omega_{\text{eff}} = 0.365 \pm 0.008$ and resulting in an effective tagging efficiency of

$$\varepsilon_{\text{eff}} = (2.38 \pm 0.27)\% . \tag{6.17}$$

A comparison with the effective tagging efficiency quoted in the final Belle result on $S_{b \to c\bar{c}s}$ and $C_{b \to c\bar{c}s}$ [63],

$$\varepsilon^{\text{Belle}}_{\text{eff}} = (29.8 \pm 0.4)\% , \tag{6.18}$$

disclose the challenges of flavour tagging in LHC's pp collisions. In contrast to LHCb and other experiments at hadron colliders, the B factories can rely on clean $\Upsilon(4S) \to B\bar{B}$ events, allowing for a high tagging efficiency and a small mistag rate. Furthermore, the irreducible

mistag fraction of the opposite-side taggers, which is a result of using oscillated B^0 mesons as tagging B candidates, is non-existent in the B factories, due to the coherent B–$\bar{B}$ production. Hence, to compete with B factories like Belle, LHCb needs a larger number of reconstructed signal decays, due to its comparably poor flavour tagging. Fortunately, the high b production cross-section at LHC can compensate for this, but requires a reasonably powerful selection and a good understanding of other experimental effects, like production asymmetries and background composition.

6.4 Production asymmetry

A possible B^0–$\bar{B}^0$ production asymmetry at LHCb has been studied by other analyses in decays of $B^0 \to J/\psi K^{*0}$ [133], where CP violating effects are expected to be below the level of $\mathcal{O}(10^{-3})$, and in decays of $B^0/B_s^0 \to K\pi$ [134], in which direct CP violation is expected. As the latter study exploits the larger dataset of $0.69\,\mathrm{fb}^{-1}$ collected in 2011, its production asymmetry measurement is used as input to the $B^0 \to J/\psi K_S^0$ measurement. For completeness, this section briefly describes the corresponding analysis, where a measurement of the time-dependent rates of candidates tagged as B and $\bar{B}$ that decay to the flavour specific $K^+\pi^-$ or $K^-\pi^+$ final states at decay time t is performed.

Using an unbinned maximum likelihood fit to the reconstructed mass m, the decay time t, the final state ψ, where a ψ of $+1$ (-1) represents a decay to the final state $f = K^+\pi^-$ $(\bar{f} = K^-\pi^+)$, and the tag decision d, where a d of $+1$ (-1) stands for a B $(\bar{B})$ tag from the opposite-side taggers, the analysis is performed simultaneously in categories of predicted mistag fractions. The PDF used in the maximum likelihood fit incorporates the production asymmetries A_P for B^0 and A_P^s for B_s^0 production,

$$A_\mathrm{P} = \frac{R_{\bar{B}^0} - R_{B^0}}{R_{\bar{B}^0} + R_{B^0}}, \quad A_\mathrm{P}^s = \frac{R_{\bar{B}_s^0} - R_{B_s^0}}{R_{\bar{B}_s^0} + R_{B_s^0}}, \tag{6.19}$$

where R_P is the meson production rate. A brief description of effects that lead to b hadron production rate asymmetries has been given in Sec. 4.2. Besides the production asymmetry, the PDF describes the detection asymmetry

$$A_f = \frac{\varepsilon_{\bar{f}} - \varepsilon_f}{\varepsilon_{\bar{f}} + \varepsilon_f}, \tag{6.20}$$

where ε_f and $\varepsilon_{\bar{f}}$ are the reconstruction efficiencies for a final state f or $\bar{f}$, respectively. Additionally, tagging efficiency and mistag probability differences need to be accounted for. Then, the observed raw asymmetry, which is given by the interplay of the CP asymmetry and the experimental asymmetries described above, can be used to determine the direct CP asymmetries A_{CP} for $B^0 \to K\pi$ decays and A_{CP}^s for $B_s^0 \to K\pi$ decays, which are measured as

$$A_{CP} = \frac{B(\bar{B}^0 \to \bar{f}) - B(B^0 \to f)}{B(\bar{B}^0 \to \bar{f}) + B(B^0 \to f)}, \quad A_{CP}^s = \frac{B(\bar{B}_s^0 \to \bar{f}) - B(B_s^0 \to f)}{B(\bar{B}_s^0 \to \bar{f}) + B(B_s^0 \to f)}. \tag{6.21}$$

The measured production asymmetries are

$$A_\mathrm{P} = -0.015 \pm 0.013, \quad A_\mathrm{P}^s = -0.03 \pm 0.06, \tag{6.22}$$

and hereby in good agreement with the theoretical predictions, as described in Sec. 4.2, and with the measurement performed in the $B^0 \to J/\psi K^{*0}$ channel. Though, the statistical uncertainties still do not allow for a precise measurement of the production asymmetry, and much less for an analysis of its dependency on the B meson kinematics.

6.5 Background estimation

The main background contributions to the selected $B^0 \to J/\psi K_S^0$ sample are expected to originate from combinatorial background, i.e. random combinations of pions, muons, K_S^0 mesons, and J/ψ mesons that are directly produced in the pp collisions, or from long-lived background, i.e. partially reconstructed B hadron decays where the J/ψ candidate is a decay product of a B hadron but is combined with a K_S^0 meson candidate originating from a different process. As these long-lived components might introduce non-vanishing tagging asymmetries, it is important to understand the portion and source of these backgrounds.

6.5.1 Studies on simulated datasets

An extensive study of simulated samples that contain potential sources of background is performed. First, the full stripping and selection requirements, as quoted in Sec. 6.2, are applied to these samples. Then, for each remaining $B^0 \to J/\psi K_S^0$ candidate, the decay chain is matched to the simulated decay chains, thus identifying the source of background candidates. By counting the occurrences of the different non-signal decays, the ratio of expected background contributions is assessed.

In a first step, the background search is performed on inclusive samples, which contain a variety of decays:

- 20 million events containing a $J/\psi \to \mu^+\mu^-$ decay within the LHCb acceptance

- 24 million events containing a b and two muons within the LHCb acceptance each with a minimum momentum of $3\,\mathrm{GeV}/c$

- 6 million events with decays of $B^0 \to J/\psi X$ and subsequent $J/\psi \to \mu^+\mu^-$ decay within the LHCb acceptance

- 6 million events with decays of $B^+ \to J/\psi X$ and subsequent $J/\psi \to \mu^+\mu^-$ decay within the LHCb acceptance

- 2 million events with decays of $B_s^0 \to J/\psi X$ and subsequent $J/\psi \to \mu^+\mu^-$ decay within the LHCb acceptance

The results in Tab. 6.5 show that small exclusive background contributions from $B_s^0 \to J/\psi K_S^0$, $\Lambda_b \to J/\psi \Lambda$, and $B^0 \to J/\psi K^{*0}$ decays can be expected. Due to the $\approx 100\,\mathrm{MeV}/c^2$ mass difference between B_s^0 and B^0 meson, the $B_s^0 \to J/\psi K_S^0$ contribution of 1% can be easily incorporated in the analysis by either excluding the B_s^0 mass region from the fit, or by fitting its contribution in a broad mass window using the same parametrisation as for the B^0 signal, as both, J/ψ and K_S^0, candidates are correctly reconstructed. This stands in contrast

to the backgrounds that arise from mis-reconstructed $\Lambda_b \to J/\psi \Lambda$ and $B^0 \to J/\psi K^{*0}$ decays, in which either the proton from the Λ meson decay or the kaon from the K^{*0} decay is mis-identified as a π^+ candidate.

Tab. 6.5: Truth-matched decays that were reconstructed as $B^0 \to J/\psi K_S^0$ decays and fulfilled the stripping and selection requirements in the inclusively simulated samples. Besides candidates from combinatorial backgrounds, no reconstructed candidates that could be matched to a specific decay mode were found in the inclusive $B^+ \to J/\psi(\mu^+\mu^-)X$ sample.

Sample	Decay mode	#Events	Ratio %
20M $pp \to X J/\psi(\mu^+\mu^-)$	$B^0 \to J/\psi(\mu^+\mu^-)K_S^0(\pi^+\pi^-)$	2893	98.0 %
	$B_s^0 \to J/\psi(\mu^+\mu^-)K_S^0(\pi^+\pi^-)$	40	1.4 %
	$\Lambda_b \to J/\psi(\mu^+\mu^-)\Lambda(p\pi^-)$	18	0.6 %
25M $pp \to bX \to X'\mu^+\mu^-$	$B^0 \to J/\psi(\mu^+\mu^-)K_S^0(\pi^+\pi^-)$	592	97.9 %
	$B_s^0 \to J/\psi(\mu^+\mu^-)K_S^0(\pi^+\pi^-)$	13	2.1 %
6M $B^0 \to J/\psi(\mu^+\mu^-)X$	$B^0 \to J/\psi(\mu^+\mu^-)K_S^0(\pi^+\pi^-)$	26 759	99.9 %
	$B^0 \to J/\psi(\mu^+\mu^-)K^{*0}(K^+\pi^-)$	13	0.1 %
2M $B_s^0 \to J/\psi(\mu^+\mu^-)X$	$B_s^0 \to J/\psi(\mu^+\mu^-)K_S^0(\pi^+\pi^-)$	455	100.0 %

To better understand the structure of these backgrounds in the reconstructed mass distribution, simulated events of pp collisions with either $\Lambda_b \to J/\psi(\mu^+\mu^-)\Lambda(p\pi^-)$ or $B^0 \to J/\psi(\mu^+\mu^-)K^{*0}(K^+\pi^-)$ decays are reconstructed and the full selection procedure is applied. The resulting mass and decay time distributions are shown in Fig. 6.4, and include both the mis-reconstructed exclusive decays as well as combinatorial background. The observed mass distributions are reasonably flat within the interesting mass range, and no clearly peaking background contributions are observed. In the decay time distribution, an exponential behaviour is observed, with a larger pseuo-lifetime for the candidates reconstructed in the $\Lambda_b \to J/\psi \Lambda$ than in the $B^0 \to J/\psi K^{*0}$ samples. In summary, these mis-reconstructed exclusive background components can be easily taken care of by incoporating them as part of the long-lived background contribution.

6.5.2 Studies on data

As has been shown in the previous section by studying simulated datasets, only small contributions of exclusive backgrounds are expected. The studies suggest that the background contribution should be dominated by combinatorial background and that only the contribution of $B_s^0 \to J/\psi K_S^0$ decays might need to be separately accounted for. This is verified by a cross-check performed on data, in which the reconstructed mass of $B^0 \to J/\psi K_S^0$ candidates is analysed in a wide mass region, using both tagged and untagged candidates. In a simultaneous fit to the long and downstream sub-samples, the $B^0 \to J/\psi K_S^0$ signal contribution is modelled as double Gaussian with common mean but different widths, the $B_s^0 \to J/\psi K_S^0$ contribution is modelled by a single Gaussian function, and the combinatorial and long-lived component is represented by an exponential function. The mean masses of B_s^0 and B^0 contributions are each shared between the downstream and the long sample. The distribution of reconstructed
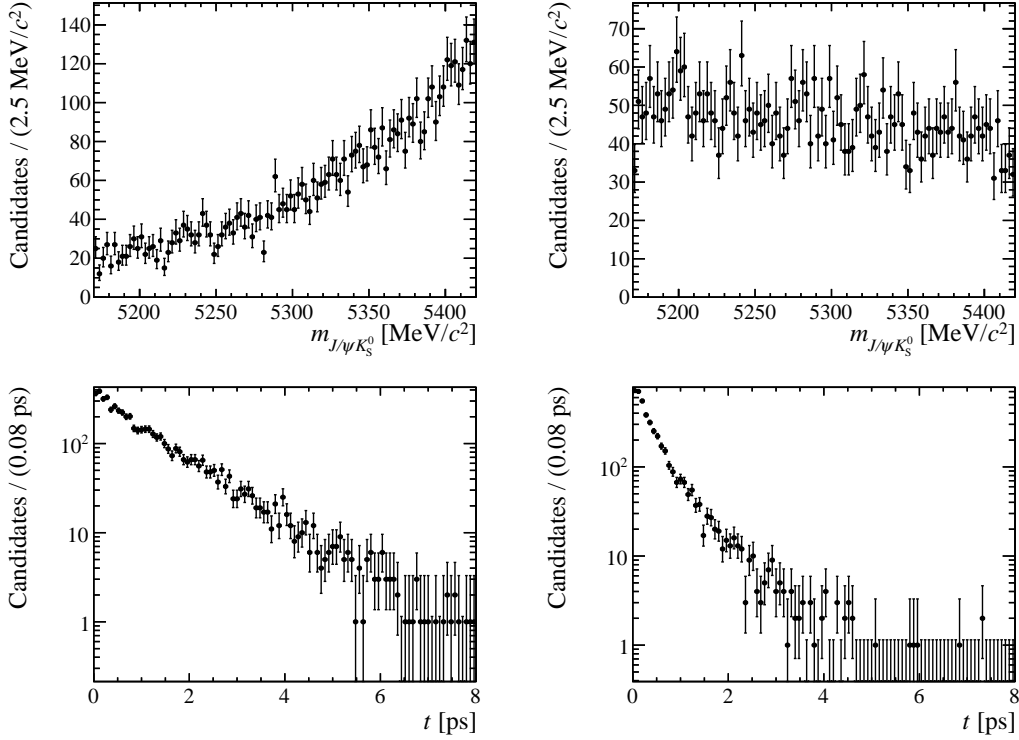
Fig. 6.4: Distribution of the reconstructed mass (top) and the decay time (bottom) of simulated $\Lambda_b \to J/\psi\,\Lambda$ decays (left) and $B^0 \to J/\psi\,K^{*0}$ decays (right) that were mis-reconstructed as $B^0 \to J/\psi\,K_S^0$ due to $p\pi$ and $K\pi$ mis-identification or due to partially random combinations with other tracks.

masses and the fit projections are shown in Fig. 6.5. Besides a clear B^0 signal peak, a small B_s^0 peak is visible, which is limited to outside the final, nominal fit range. Further, the remaining background component nicely describes the background contributions. No apparent peaking background components stand out of the flat combinatorial background.

A further study is performed to exclude any *CP*-like asymmetries in the background contributions, e.g. as a result of partially reconstructed b hadron decays that could have oscillating properties or could suffer from large production asymmetries. For this study, a fit to the reconstructed mass of the detached, biased, tagged sample in the nominal mass range is used to discriminate signal and background contributions and determine background weights for each candidate with the sPlot method [132]. Then, the time-dependent raw asymmetry

$$\mathcal{A}_{\mathrm{bkg}}(t) = \frac{N_{\mathrm{bkg}}^{\bar{B}^0}(t) - N_{\mathrm{bkg}}^{B^0}(t)}{N_{\mathrm{bkg}}^{\bar{B}^0}(t) + N_{\mathrm{bkg}}^{B^0}(t)}, \tag{6.23}$$

where $N_{\mathrm{bkg}}^{\bar{B}^0}(t)$ ($N_{\mathrm{bkg}}^{B^0}(t)$) is the number of reconstructed background decays at decay time t tagged as $\bar{B}^0$ (B^0), is analysed and checked for oscillating and non-oscillating background components, see Fig. 6.6. Qualitatively, no oscillating behaviour is observed. The difference
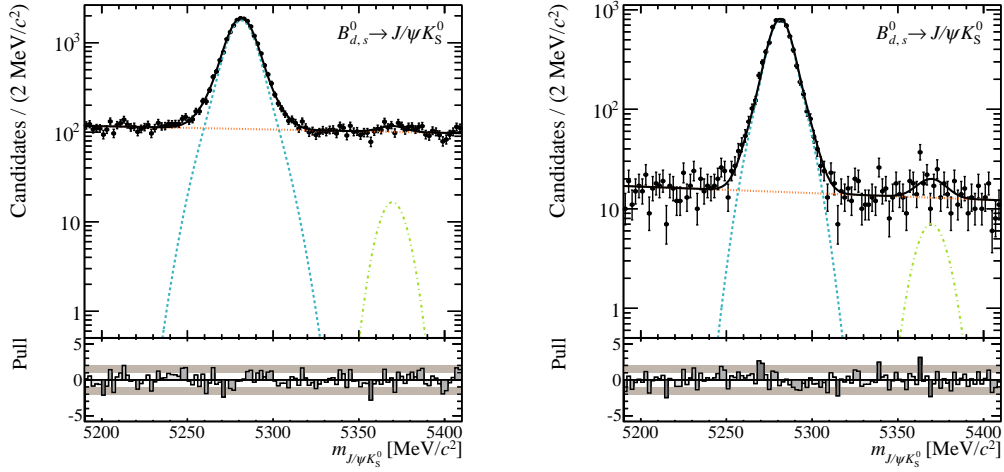
Fig. 6.5: Distribution of the reconstructed mass of downstream (left) and long (right) $J/\psi K_S^0$ candidates as observed on data. The projection of a simultaneous fit to both distributions is overlayed, where the dashed line (blue) represents the $B^0 \to J/\psi K_S^0$ signal, the dash-dotted (green) line the $B_s^0 \to J/\psi K_S^0$ contribution, and the dotted (orange) line the background. The solid (black) line descibes the sum of all contributions.

of time-integrated rates of background candidates tagged as B^0 and candidates tagged as $\bar{B}^0$ is found to be balanced except for 5 candidates. Hence, the background is assumed to be equally tagged as B^0 and $\bar{B}^0$ and no time-dependent or -independent asymmetries need to be incorporated in the description of the background contributions.
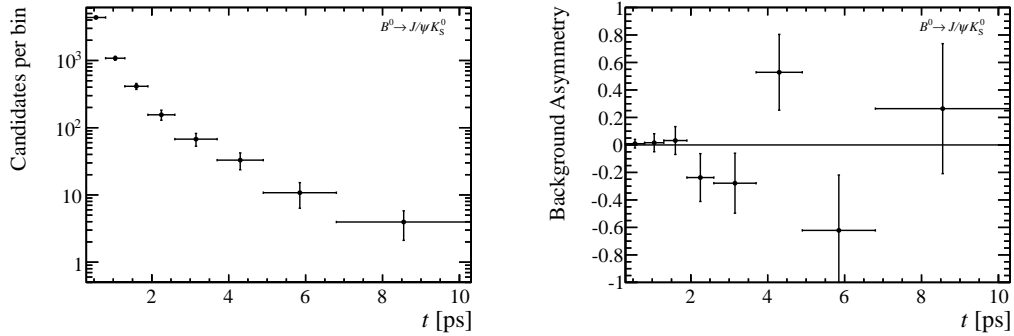

Fig. 6.6: Decay time distribution (left, logarithmic scale) and the time-dependent tagging asymmetry $\mathcal{A}_{\mathrm{bkg}}(t)$ (right) of the background candidates, determined from an sPlot to the reconstructed mass.

6.6 Decay time resolution

The finite vertex and momentum resolution of the tracking system leads to a finite decay time resolution of the reconstructed B^0 mesons. While the LHCb design foresees a decay

time resolution of approximately 50 fs, it is important to estimate the decay time resolution for the decay channel at hand. For instance, the resolution in a specific decay channel could be affected by kinematic properties of the decay channel, specific reconstruction effects, or selection criteria.

In the $B^0 \rightarrow J/\psi K_S^0$ measurement, the resolution is accounted for by convolving the PDF $P(t')$, which describes the distribution of true decay times t' with a resolution model $\mathcal{R}(t - t')$ to arrive at the distribution $P(t)$ of measured decay times t. In this section, the strategy to determine a decay time resolution model $\mathcal{R}(t - t')$ is presented. Most of the quoted results are explained in more detail in Refs. [25, 26].

6.6.1 Per-event resolution model

Typically, resolution models consist of weighted sums of Gaussian functions with different widths σ_i but common mean μ. In the $B^0 \rightarrow J/\psi K_S^0$, a per-event approach is chosen that makes use of the decay time error estimates σ_t of the decay tree fitter. The resolution is chosen as a weighted sum of multiple Gaussian functions with widths proportional to σ_t,

$$R(t - t'|\sigma_t) = \sum_i f_i \frac{1}{\sqrt{2\pi} s_i \sigma_t} \exp\left(-\frac{(t - t' - b\sigma_t)^2}{2(s_i \sigma_t)^2} \right), \qquad (6.24)$$

where t' is the true decay time, t is the measured decay time, and σ_t is the decay time resolution estimate from the decay tree fitter, f_i is the fraction of each Gaussian function i, s_i its scale factor, and b is a relative bias parameter shared among the Gaussian functions.

6.6.2 Resolution in simulated samples

In a first attempt to identify a valid resolution model, the resolution in simulated samples is studied, separately for downstream and long truth-matched $B^0 \rightarrow J/\psi K_S^0$ candidates that fulfil the selection requirements. Different resolution models are fitted to the residuals $(t - t')$ of reconstructed and generated decay time. The most reasonable result is found when choosing a triple Gaussian per-event resolution model. However, a slightly asymmetric distribution towards negative residuals can be observed with large simulated samples. The projections of the resolution model to the distribution of decay time residuals are shown in Fig. 6.7, separately for downstream and long candidates.

6.6.3 Resolution in data samples

The prescaled sample offers access to prompt background candidates, formed from tracks that originate from a primary pp collision, i.e. from a PV, rather than from a B^0 decay. As such background candidates should possess a flight distance of zero, and hence peak at $t' = 0$, their distribution in reconstructed decay time t can be used for a convenient determination of the decay time resolution. However, the nominal dataset using candidates from the detached stripping line is not suited for such a study, as acceptance effects from the trigger's decay length significance requirement as well as the decay time requirement, $t > 0.3$ ps, removes any remaining prompt background. Instead, the prescaled dataset is used, and only decay
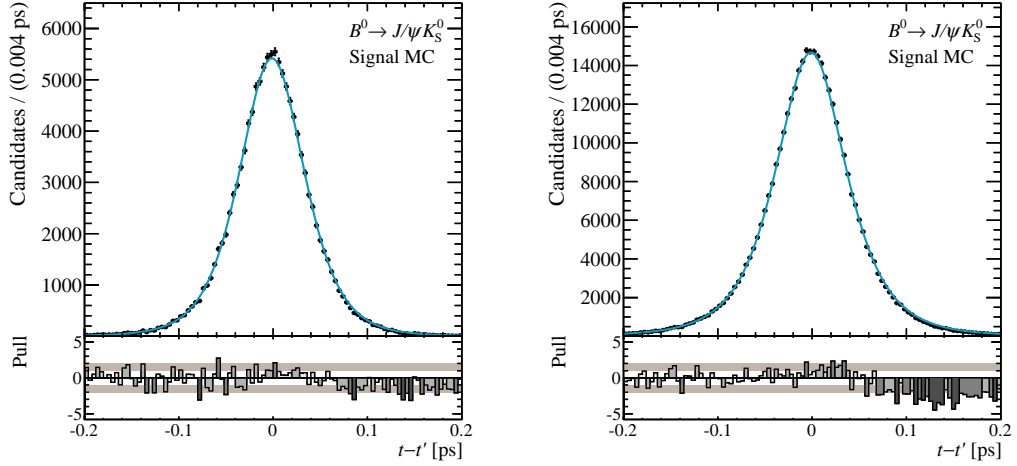
Fig. 6.7: Distribution of the decay time residuals ($t - t'$) of truth-matched long (left) and downstream (right) $B^0 \to J/\psi K^0_S$ candidates in simulated samples. The projections of the fitted triple Gaussian per-event resolution models are superimposed.

time unbiased trigger lines are required, i.e. the HLT2 `DiMuonJpsi` line, with a prescale of 20%, see Sec. 6.2.3. Additionally, the requirements on the minimal decay time as well as the tagging requirements are dropped.

In the $B^0 \to J/\psi K^0_S$ reconstruction, the decay vertex of the B^0 meson is mainly defined by the J/ψ decay vertex. Therefore, it is reasonable to only use candidates of the prescaled unbiased sample that were formed from true J/ψ decays. For this, the sPlot method is used by fitting the reconstructed mass of the J/ψ candidates to determine signal weights. These are then used to create signal distributions of the decay time. The J/ψ signal is modelled by the sum of a Crystal Ball function [135–137] and a Gaussian function, while the background is modelled as an exponential function. The fit is performed separately for the long and the downstream sample, see Fig. 6.8. The resulting sWeighted dataset is then used to perform a fit to the decay time of the B^0 candidates in the range of $t \in [-1.5, 8]$ ps. The prompt peak is modelled by the triple Gaussian resolution model, while the long-lived tails from the signal and long-lived background components are modelled by the sum of three exponentials with different lifetime and fraction parameters, and each convolved with the resolution function. Again, the fit is performed separately for long and downstream candidates. Its results are summarised in Tab. 6.6. The decay time distributions and resulting fit projections are shown in Fig. 6.9.

Using the resolution model in a fit to the nominal samples, its equivalent average resolution is measured as 56 fs (66 fs) for candidates with long (downstream) K^0_S, resulting in dilution factors > 99.9%. Hence, resolution effects are negligible in the time-dependent *CP* measurement in $B^0 \to J/\psi K^0_S$ decays. In contrast, the resulting dilution factor for $B^0_s \to J/\psi K^0_S$ is expected to be at 61% (50%) in the long (downstream) sample.
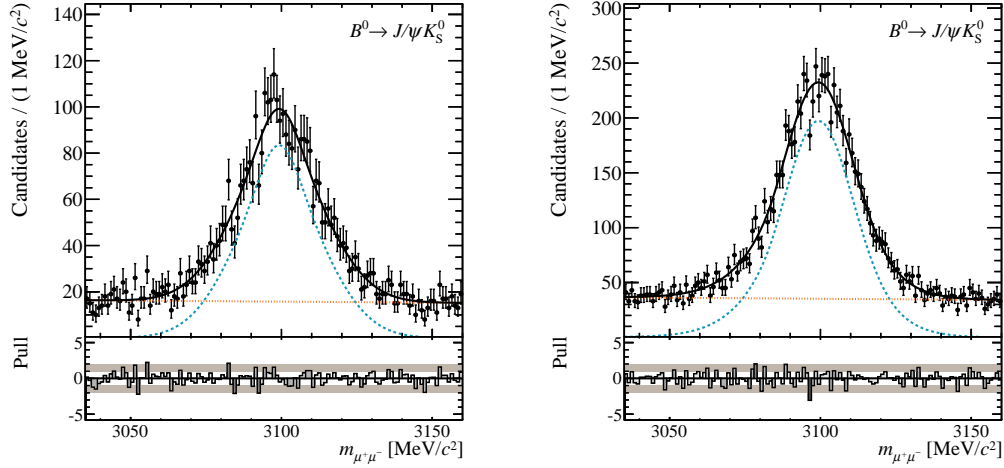
Fig. 6.8: Distribution of the reconstructed mass of *J/ψ* candidates in the long (left) and downstream (right) prescaled unbiased samples. Superimposed are the projections of fits to each of the distributions, where the signal is represented by the dashed (blue) line and the background is represented by the dotted (orange) line. The projection of the total PDF is described by the solid (black) line.

Tab. 6.6: Result of a fit of the triple Gaussian per-event resolution model to data. The definition of the dimensionless parameters of the resolution model is given in Eq. (6.24).

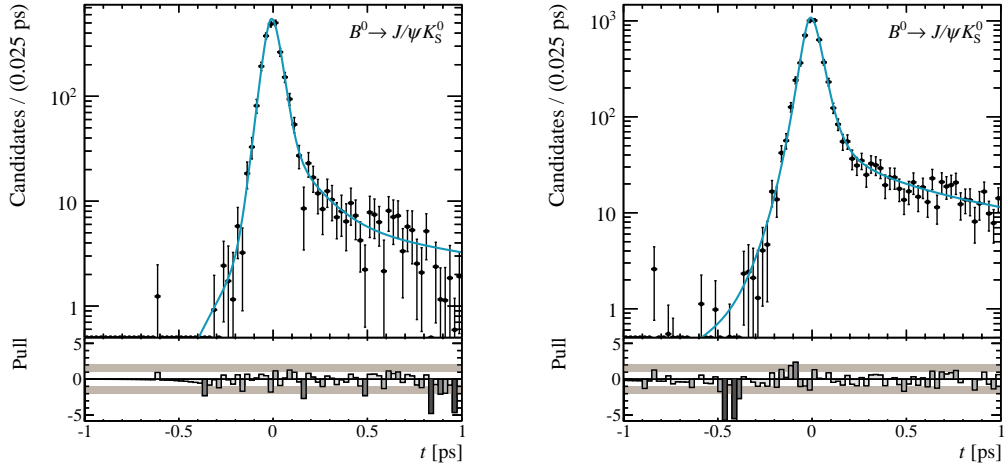| Parameter	long	downstream
b	-0.23 ± 0.06	-0.19 ± 0.04
f_2	0.62 ± 0.22	0.24 ± 0.10
f_3	0.019 ± 0.008	0.012 ± 0.004
s_1	1.03 ± 0.17	1.09 ± 0.06
s_2	1.61 ± 0.14	1.94 ± 0.22
s_3	7 ± 1	9 ± 2

Fig. 6.9: Weighted distribution of the reconstructed decay time of B^0 candidates using J/ψ signal weights from an sPlot in the long (left) and downstream (right) prescaled unbiased samples. Superimposed are the projections of fits of the triple Gaussian resolution models and the exponential functions, which describe the signal and long-lived components and are convolved with the resolution.
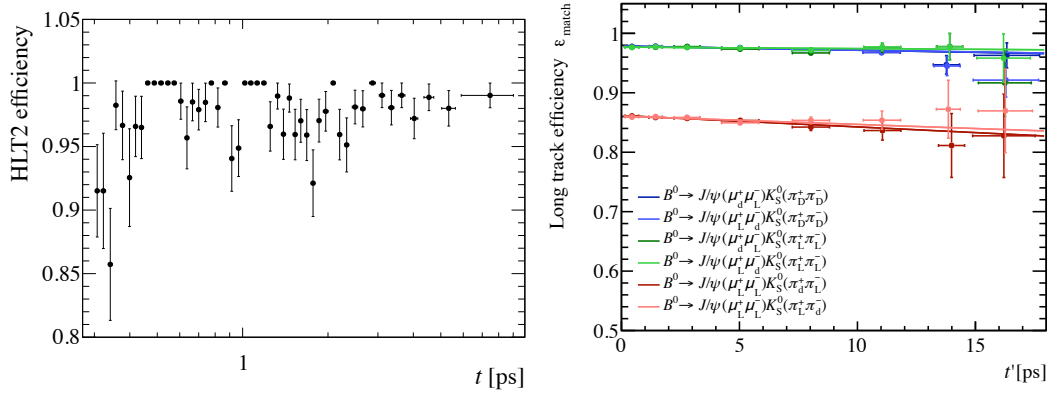

Fig. 6.10: Left: Efficiency of the biased HLT2 line as function of the reconstructed decay time t as evaluated on data, see Ref. [25]. Note the logarithmic t scale. Right: Long track matching efficiency as function of the true decay time t' as evaluated in simulated samples using truth-matched $B^0 \rightarrow J/\psi K_S^0$ decays, where one of the final particles' tracks is reconstructed as downstream track ("d") and is then matched to an associated long track, if possible. The labels "D" (downstream) and "L" (long) denote the track type of the other reconstructed final state particles. See Ref. [29].

6.7 Decay time acceptance

A decay time acceptance is a result of decay time dependent inefficiencies, e.g. detector accept-ances, reconstruction effects, or trigger and selection requirements. It can be parametrised as a function of decay time that takes values between 0 and 1, and modulates the theoretically expected distribution, e.g. an exponential decay function for the untagged signal, to arrive at the experimentally observed distribution. In the case of the $B^0 \rightarrow J/\psi K_S^0$ measurement at LHCb, decay time acceptances at low and high decay times of the B^0 candidates are observed.

The low decay time acceptance in the nominal data sample can mainly be ascribed to the decay length significance requirement on the J/ψ candidate in the biased HLT2 trigger line, as neither the required HLT1 line nor the selection introduce non-trivial decay time biasing requirements. Though, due to the $t > 0.3$ ps requirement in the final selection, the decay time acceptance is expected to be negligible in the nominal sample. To back this claim, studies on simulated samples are performed, see Ref. [25], which show, that acceptance effects above a decay time of 0.3 ps are small. Additionally, a data driven method is pursued. First, the selection is adapted to allow for candidates for which the muons of the J/ψ candidate induced a positive trigger decision by the biased HLT2 `DiMuonDetachedJPsi` line or by the unbiased HLT2 `DiMuonJpsi` line, without changing the requirement for the HLT1 line. To increase the sample size, untagged candidates are added as well. Then, the time-dependent efficiency can be evaluated as the time-dependent ratio of signal candidates that pass both HLT2 lines over the signal candidates that pass the unbiased lines,

$$\epsilon_{\text{low}}(t) = \frac{\text{Signal candidates} \in \texttt{DiMuonDetachedJPsi} \wedge \texttt{DiMuonJpsi}}{\text{Signal candidates} \in \texttt{DiMuonJpsi}} \,. \tag{6.25}$$

The signal yields are determined from fits to the reconstructed mass of the B^0 candidates in bins of the decay time. Bin boundaries are chosen such that all bins contain approximately the same number of signal candidates. The resulting efficiency is shown as a histogram in decay time in Fig. 6.10. As discussed before, the decay time efficiency is nearly negligible at the examined decay times, $t > 0.3$ ps, in good agreement with the studies in simulated datasets.

A high decay time acceptance, which leads to a loss of candidates at large decay times, is observed. Ignoring it leads to underestimated measurements of the B^0 lifetime. Using simulated datasets, a possible parametrisation of this acceptance is found as

$$\epsilon_{\text{high}}(t) = 1 + \beta t \,, \tag{6.26}$$

with

$$\beta^{\text{d}} = (-19.4 \pm 3.2) \cdot 10^{-3} \text{ps}^{-1} \quad \text{and} \quad \beta^{\text{l}} = (-4.2 \pm 2.0) \cdot 10^{-3} \text{ps}^{-1} \,,$$

for the downstream and long track sample, respectively. To understand, why the extent of the effect is more apparent in the long than in the downstream sample, additional studies are performed using simulated data [29]. The largest effect is found to originate from the VELO reconstruction, which is required for long tracks. Tracks with large distance-of-closest-approach with respect to the beam axis (DOCAz) have a lower efficiency to be reconstructed as long tracks [138]. As DOCAz is correlated with the B^0 meson lifetime, a small inefficiency that increases with decay time t can be observed, see Fig. 6.10.

7 Measurement of *CP* Violation in $B^0 \to J/\psi K_S^0$

Chapters 5 and 6 have covered a description of the analysis strategy, the most important tools, the required inputs, the datasets, and the preparatory studies for a measurement of *CP* violation in the $B^0 \to J/\psi K_S^0$ channel with LHCb's 2011 dataset. The final step, the actual measurement, is presented in this chapter.

As the analysis is performed in terms of an unbinned maximum likelihood fit, the choice of PDFs is discussed, based on the findings of the preparatory studies. Then, the fit method is validated and a first realistic estimate of the statistical uncertainty of the measurement is given. Now, the fit is performed on the actual dataset, and provides estimates for the central values and statistical uncertainties of the *CP* parameters and of the nuisance parameters, like the B^0 lifetime and the mixing frequency. The validity of the results relies on an accurate description of the distributions, and hence on an accurate PDF parametrisation and an unbiased parameter estimation. Thus, some basic cross-checks on the stability of the result among different sub-samples and when using different analysis approaches are performed. Finally, systematic uncertainties are assessed, and the full result of the measurement of the *CP* observables $S_{J/\psi K_S^0}$ and $C_{J/\psi K_S^0}$ is presented.

7.1 Likelihood fit

The analysis is performed in terms of an extended maximum likelihood fit, simultaneous to the two independent sub-samples of the downstream and long candidates, allowing for a different treatment of resolution effects in the two sub-samples. The likelihood,

$$\mathcal{L}(\lambda) = \prod_s \frac{e^{-\sum_j N_j^s}}{n_s!} \prod_i^{n_s} \sum_j N_j^s \mathcal{P}_j^s(x^s | \lambda_j^s), \tag{7.1}$$

is a product of the two extended likelihoods which describe the two subsets s of downstream and long candidates. Each of these likelihoods consists of a sum of components/species j described by a PDF $\mathcal{P}_j^s(x^s | \lambda)$ and a yield parameter N_j^s, which represents the number of observed candidates of each species. For each sub-sample, a Poisson term relates the number of measured candidates, i.e. the sum of observed candidates in each species $\sum_j N_j^s$, to the actual number n_s of candidates in that specific sub-sample. The implementation of the likelihood fit makes use of the RooFit library provided by the ROOT framework [98, 139].

7.1.1 Observables

Although the PDF parametrisations differ among the two sub-samples, they describe the distributions of the same observables:

- The invariant mass $m = m_{J/\psi K_S^0}$ from a decay tree fit under the constrain that the masses of the daughters, J/ψ and K_S^0, are consistent with the average from other measurements [31], and that the B^0 candidate originates from its associated primary vertex.

- The decay time t from a similar decay tree fit, but without the constrain on the masses of the J/ψ and K_S^0 candidates.

- The decay time resolution estimate σ_t as derived from the fit uncertainty of the decay tree fit used for the determination of the decay time t.

- The tag d and calibrated mistag fraction estimate η from the combination of opposite-side tagging algorithms.

The measurement is performed on limited ranges to ensure the validity of the fit model. The chosen ranges are quoted in Tab. 7.1.

Tab. 7.1: Ranges of the observables used in the fit.

Observable	Range
Reconstructed mass $m_{J/\psi K_S^0}$	5230–5330 MeV/c^2
Decay time t	0.3–18.3 ps
Decay time resolution estimate σ_t	0.0–0.2 ps
Flavour tag d	$\{-1, +1\}$
Wrong tag fraction estimate η	0.0–0.5

7.1.2 Parametrisation

Each subset's PDF $\mathcal{P}^s(\boldsymbol{x})$, where the parameter vector λ^s has been dropped for simplicity of notation, is described as the sum of a signal component, $\mathcal{P}_S^s$, and a background component, $\mathcal{P}_B^s$,

$$N^s \mathcal{P}^s(\boldsymbol{x}) = N_S^s \mathcal{P}_S^s(\boldsymbol{x}) + N_B^s \mathcal{P}_B^s(\boldsymbol{x}), \tag{7.2}$$

where the latter describes both the combinatorial background as well as the background formed from partially reconstructed b decays. As the fit is simultaneous in the candidates formed from downstream and long track pion tracks, the choice of notation is

$$\mathcal{P}_j^s(\boldsymbol{x}) \quad \text{with the sub-sample index } s \in \{\text{d (downstream)}, \text{l (long)}\},$$

$$\text{with the components } j \in \{\text{S (signal)}, \text{B (background)}\}.$$

For each sub-sample s and each component j it is assumed that the associated PDFs $\mathcal{P}_j^s(m, t, \sigma_t, d, \eta)$ can be factorised into a product of a PDF describing the mass distribution and a PDF describing the distribution in the remaining observables

$$\mathcal{P}_j^s(m, t, \sigma_t, d, \eta) = \mathcal{P}_j^s(m) \cdot \mathcal{P}_j^s(t, \sigma_t, d, \eta). \tag{7.3}$$

The PDFs $\mathcal{P}_S^s(t, \sigma_t, d, \eta)$ of the signal components cannot be further factorised into naive products, as the part of the PDF that describes *CP* violation depends on the decay time t and the flavour tag d, its resolution depends on the resolution estimate σ_t, and the mistag fraction estimate η is an event-by-event observable rather than a parameter. Thus, making use of conditional PDFs, the PDF $\mathcal{P}_S^s(t, \sigma_t, d, \eta)$ can be rewritten as

$$\mathcal{P}_S^s(t, \sigma_t, d, \eta) = \mathcal{P}_S^s(t, d | \eta, \sigma_t) \cdot \mathcal{P}_S^s(\eta) \cdot \mathcal{P}_S^s(\sigma_t). \tag{7.4}$$

In contrast, as no significant time-dependent asymmetry has been observed for the background component, see Sec. 6.5 for details, it is assumed, that the background is equally distributed in tags d, $\mathcal{P}_B^s(d) = 1$, and that the PDF describing the distribution in predicted mistag fractions η factorises, and hence

$$\mathcal{P}_B^s(t, \sigma_t, d, \eta) = \mathcal{P}_B^s(t | \sigma_t) \cdot \mathcal{P}_B^s(\sigma_t) \cdot \mathcal{P}_B^s(\eta) \cdot \mathcal{P}_B^s(d). \tag{7.5}$$

Here, $\mathcal{P}_B^s(t | \sigma_t)$ is the conditional decay time PDF of the background, whose resolution depends on the event-by-event value of the decay time resolution estimate σ_t.

The reconstructed mass distributions of the signal has been studied in simulated samples. Due to the constraint on the J/ψ and the K_S^0 masses, radiative tails to lower masses are removed to a large extent, so that the signal mass distribution can be described by the sum of two Gaussian PDFs,

$$\mathcal{P}_S^s(m) = f_{S,m}^s \mathcal{G}(m | m_{B^0}, \sigma_{S,m,1}^s) + (1 - f_{S,m}^s) \mathcal{G}(m | m_{B^0}, \sigma_{S,m,2}^s), \tag{7.6}$$

with common mean m_{B^0} but different widths $\sigma_{S,m,1}^s$ and $\sigma_{S,m,2}^s$. Only the mean parameter is shared between the two sub-samples. The background component, which shows a nearly flat mass distribution, is parametrised as an exponential distribution,

$$\mathcal{P}_B^s(m) \propto \exp\left(-\alpha_{B,m}^s m_{B^0}\right). \tag{7.7}$$

The mass distributions and the projections of the signal and background components of the full PDF are shown in Fig. 7.1.

The signal and background distributions of the mistag fraction estimate η are described by PDFs that are formed from histograms obtained with the sPlot technique, where the reconstructed mass is used as discriminating observable. The histogrammed PDFs are identical for both sub-samples, as shown in Fig. 7.2.

The distributions of the estimated decay time resolutions σ_t are modelled differently in each component and each sub-sample, but are all represented by sums of lognormal functions

$$\mathrm{Ln}(\sigma_t | M_{\sigma_t}, k) = \frac{1}{\sqrt{2\pi}\sigma_t \ln k} \exp\left(-\frac{\ln^2\left(\sigma_t/M_{\sigma_t}\right)}{2\ln^2(k)}\right), \tag{7.8}$$
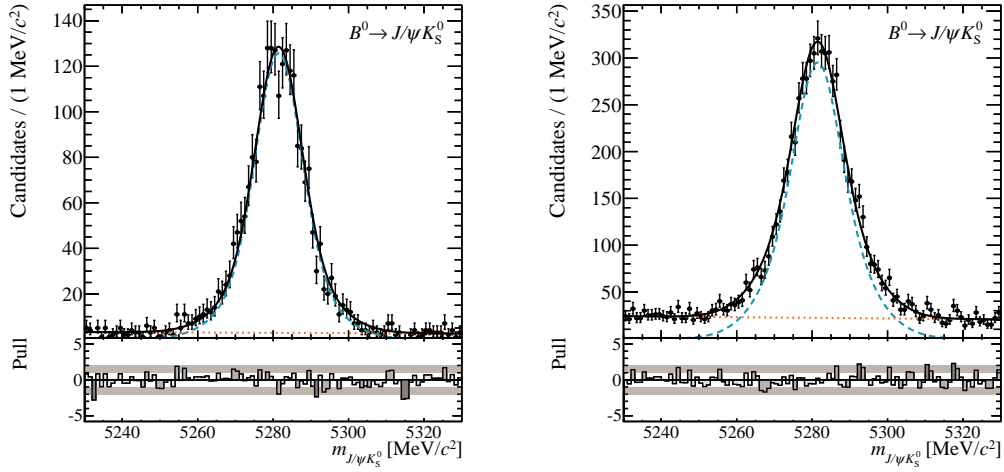
Fig. 7.1: Mass distribution of the nominal data sample for the long (left) and downstream (right) sub-samples. Besides the data points, the PDF projections of the signal (blue, dashed), the background (orange, dotted), and the full PDF (black, solid) are shown. Comparing with Fig. 6.1, the yield reduction from requiring candidates to be tagged by the opposite-side taggers is evident.
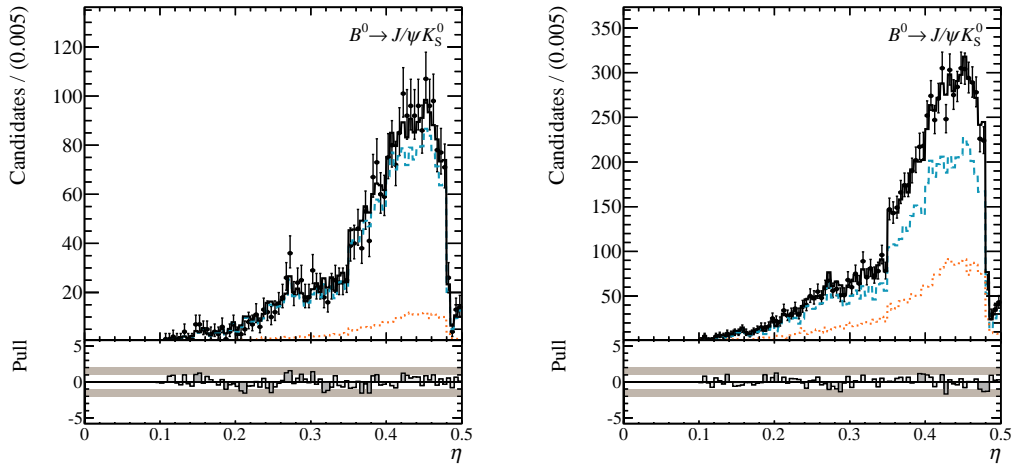

Fig. 7.2: Distribution of mistag fraction estimates η in the nominal data sample for the long (left) and downstream (right) sub-samples. Besides the data points, the PDF projections of the signal (blue, dashed), the background (orange, dotted), and the full PDF (black, solid) are shown.

where M_{σ_t} is the median and k is the tail parameter. In both sub-samples, each of the background components are described by single lognormal functions. Each of the signal components in the two sub-samples is chosen as a sum of two lognormal functions, but with common median parameter for the sub-sample of long candidates, and different median parameters in the downstream sub-sample. The distribution of the sub-samples in σ_t and the PDF projections from the nominal fit are shown in Fig. 7.3.
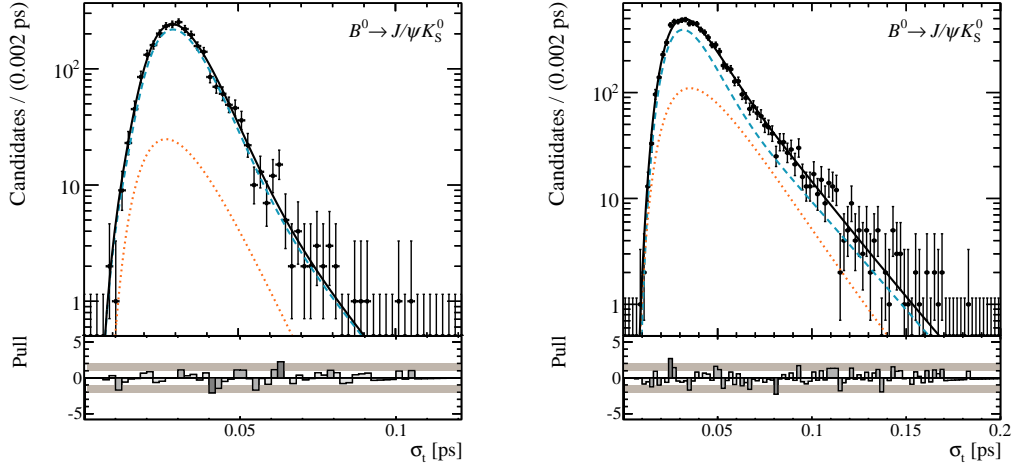
Fig. 7.3: Distribution of the nominal data sample in the σ_t observable, the decay time resolution estimate, shown separately for the long (left) and downstream (right) sub-samples in a logarithmic y-scale. Note, that due to different resolutions in the downstream and long sample, different σ_t scales have been chosen for better illustration. Besides the data points, the PDF projections of the signal (blue, dashed), the background (orange, dotted), and the full PDF (black, solid) are shown.

The decay time resolution function $\mathcal{R}^s(t - t'|\sigma_t)$, which correlates the true decay times t' as described by the decay time PDFs with the measured decay times t, is chosen differently for the two sub-samples, but is shared between the signal and the background component of each sub-sample. The resolutions depend on the event-by-event resolution estimate σ_t, and are chosen as the sum of three Gaussian functions,

$$\mathcal{R}^s(t - t'|\sigma_t) = \sum_{i=1}^{3} f_i^s \frac{1}{\sqrt{2\pi}s_i \sigma_t} \exp\left(-\frac{(t - t' - b^s \sigma_t)^2}{2(s_i^s \sigma_t)^2} \right), \tag{7.9}$$

where the parameters are the three fractions f_i^s, which sum up to unity, the three scale factors s_i^s, and the relative bias parameter b^s. The values of the parameters can be found in Tab. 6.6 of Sec. 6.6.1, which explains the strategy to determine the resolution from a data-based analysis.

For the distribution of the background component in decay time t, a description using a sum of two exponential decay functions is chosen. As can be observed in simulated samples, see Sec. 6.5.1, the background candidates mainly originate from mis-reconstructed b hadron decays or combinatorial background, which both exhibit different pseudo-lifetimes when reconstructed as $B^0 \to J/\psi K_S^0$ decays. At the background level in this dataset, two exponentials seem to suffice for a good description of the backgrounds, as validated in studies in the side-bands of the reconstructed mass. The explicit choice of the PDFs is given as

$$\mathcal{P}_B^s \propto \left(f_{B,t}^s \frac{1}{N_{B,t,1}^s} e^{-t'/\tau_{B,t,1}^s} + (1 - f_{B,t}^s) \frac{1}{N_{B,t,2}^s} e^{-t'/\tau_{B,t,2}^s} \right) \otimes \mathcal{R}^s(t - t'|\sigma_t), \tag{7.10}$$

where t' denotes the true decay time, $f_{B,t}^s$ is a fraction parameter, and $N_{B,t,i}^s$ and $\tau_{B,t,i}^s$ are an appropriately chosen normalisation factor and a pseudo-lifetime of the i-th decay distribution,

respectively. Fraction and pseudo-lifetime parameters are not shared between the background components of the two sub-samples.

For the signal distribution in decay time t and flavour tag d, the PDF is split up into a time-dependent efficiency function $\epsilon_S^s(t)$, which accounts for the low and high decay time acceptances described in Sec. 6.7, and a conditional PDF,

$$\mathcal{P}_S^s(t, d|\sigma_t, \eta) \propto \epsilon_S^s(t) \cdot \left(\mathcal{P}_S^s(t', d|\eta) \otimes \mathcal{R}^s(t - t'|\sigma_t) \right). \tag{7.11}$$

The parametrisation of the PDF $\mathcal{P}_S^s(t', d|\eta)$,

$$\begin{aligned}
\mathcal{P}_S^s(t', d|\eta) \propto \mathrm{e}^{-t'/\tau} \bigg(& 1 - d\Delta p_0 - d A_P \big(1 - 2\omega(\eta) \big) \\
& - \Big(d \big(1 - 2\omega(\eta) \big) - A_P \big(1 - d\Delta p_0 \big) \Big) S_{J/\psi K_S^0} \sin \Delta m t' \\
& + \Big(d(1 - 2\omega(\eta)) - A_P \big(1 - d\Delta p_0 \big) \Big) C_{J/\psi K_S^0} \cos \Delta m t' \bigg),
\end{aligned} \tag{7.12}$$

incorporates the production asymmetry A_P, the calibrated mistag probability estimates $\omega(\eta)$, the tagging asymmetry parameter Δp_0, the B^0–$\bar{B}^0$ oscillation parameter Δm, and the *CP* parameters $S_{J/\psi K_S^0}$ and $C_{J/\psi K_S^0}$. Besides exploiting the time-dependent asymmetries, the PDF adds sensitivity to the asymmetry parameters by accessing the time-integrated asymmetries through its normalisation conditions. The *CP* parameters $S_{J/\psi K_S^0}$ and $C_{J/\psi K_S^0}$, as well as the production asymmetry A_P, the mistag fraction $\omega(\eta)$ which depends on the misag fraction estimate η, and the mistag fraction difference for $B^0/\bar{B}^0$ mesons Δp_0 are shared among the signal PDFs of the two sub-samples. The tagging calibration function, which transforms predicted mistag fraction estimates η into the event-by-event mistag fraction $\omega(\eta)$, is chosen following the discussion in Sec. 6.3, as

$$\omega(\eta) = p_1(\eta - \langle \eta \rangle) + p_0. \tag{7.13}$$

The distribution of decay times t and the projections of the signal and background components of the PDF are shown in Fig. 7.4.

7.1.3 Fixed and constrained parameters

Some of the parameters required for the PDFs used in the fit have been measured in the preparatory studies, see Ch. 6, as they cannot be determined in the fit to the nominal data sample. For instance, the resolution parameters, which describe the relation of decay time resolution estimates σ_t and the measured resolution, as well as the decay time acceptance parameters are fixed to the values determined in Secs. 6.6 and 6.7. This is reasonable for this set of parameters, as they have comparably small uncertainties and are only weakly correlated with the *CP* parameters.

In contrast, the tagging calibration parameters p_0, p_1, and Δp_0 and the production asymmetry parameter A_P are strongly correlated with the *CP* parameters. To correctly transfer their statistical uncertainties to the *CP* parameters $S_{J/\psi K_S^0}$ and $C_{J/\psi K_S^0}$, they are constrained within
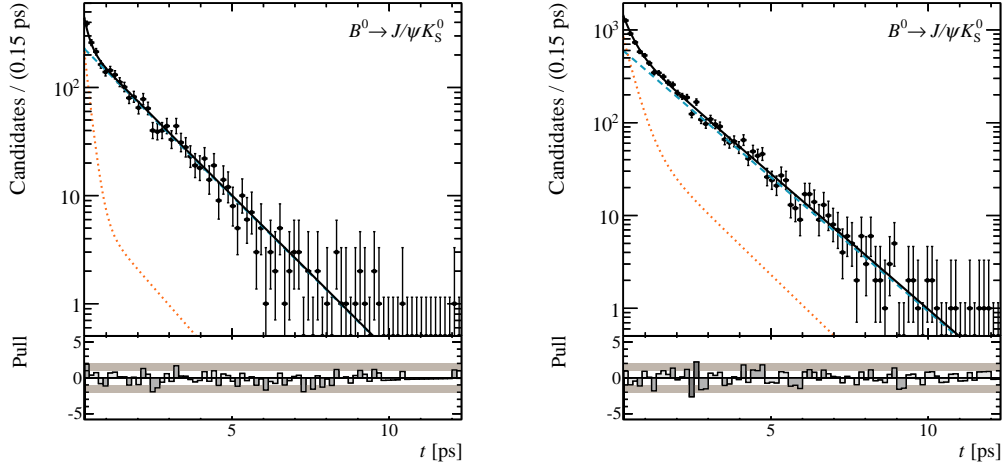
Fig. 7.4: Decay time distribution of the nominal data sample for the long (left) and downstream (right) sub-samples in a logarithmic *y*-scale. Besides the data points, the PDF projections of the signal (blue, dashed), the background (orange, dotted), and the full PDF (black, solid) are shown.

their statistical uncertainties by Gaussian constraints in the likelihood. A summary of their central values and statistical uncertainties can be found in Tab. 7.2. The systematic uncertainties for this parameters are separately considered in the studies of systematic effects in Sec. 7.4.

Tab. 7.2: Constrained parameters.

Parameter	Value
Tagging calibration parameter p_1	1.035 ± 0.021
Tagging calibration parameter p_0	0.392 ± 0.009
Mistag fraction asymmetry Δp_0	0.0110 ± 0.0034
Production asymmetry A_{P}	-0.015 ± 0.013

7.1.4 Sensitivity and fit validation

The implementation of the likelihood fit with the presented parametrisation is tested on a large number (10 000) of simulated pseudo-experiments, so-called toy datasets, see Sec. 6.1.2. The distribution of observables in these toy datasets are generated from the full PDF parametrisation. All parameters, including the yields of the different components, are set to the values determined from fits to data, except for the *CP* parameters, which are chosen as

$$S_{J/\psi K_S^0} = 0.69, \quad C_{J/\psi K_S^0} = 0, \tag{7.14}$$

in accordance with the results of former measurements by other experiments. In each toy dataset i, a fit is performed to determine the fit estimates for each parameter's central value λ_i

and uncertainty $\sigma_{\lambda,i}$. These are used to study the distributions of the residuals $\text{Res}_{\lambda,i}$ and pulls $\text{Pull}_{\lambda,i}$,

$$\text{Res}_{\lambda,i} = \lambda_i - \lambda_{\text{gen},i}, \quad \text{Pull}_{\lambda,i} = \text{Res}_{\lambda,i}/\sigma_{\lambda,i}. \tag{7.15}$$

Here, $\lambda_{\text{gen},i}$ is the parameter value used in the generation of the data sample. In case of asymmetric uncertainties, the positive (negative) uncertainty is used for the parameter estimate that are larger (smaller) than the generated value.

In the Gaussian limit, an unbiased parameter estimation leads to distributions of residuals and pulls that can be described by a Gaussian function centred at 0. Deviations of the mean from 0 can indicate issues in the fit model or its implementation. In a Gaussian distribution of the residuals, the width represents the expected average parameter uncertainty, and can be used as an estimate for the sensitivity of the measurement. Further, if the parameter uncertainty estimates are correct, the pull distribution should resemble a Gaussian distribution with width 1.

In Fig. 7.5, the residual and pull distributions for the *CP* parameters $S_{J/\psi K_S^0}$ and $C_{J/\psi K_S^0}$ are shown, together with the overlayed projections and results of the fit of a Gaussian function. The width of the residual distributions imply an expected statistical uncertainty of 0.08 for $S_{J/\psi K_S^0}$ and 0.10 for $C_{J/\psi K_S^0}$, and a small negative bias. Further, the pull distributions indicate a slight underestimation of the uncertainties by 10% and a bias in the order of 5% of the statistical uncertainty. These biases need to be considered in the estimation of systematic uncertainties.
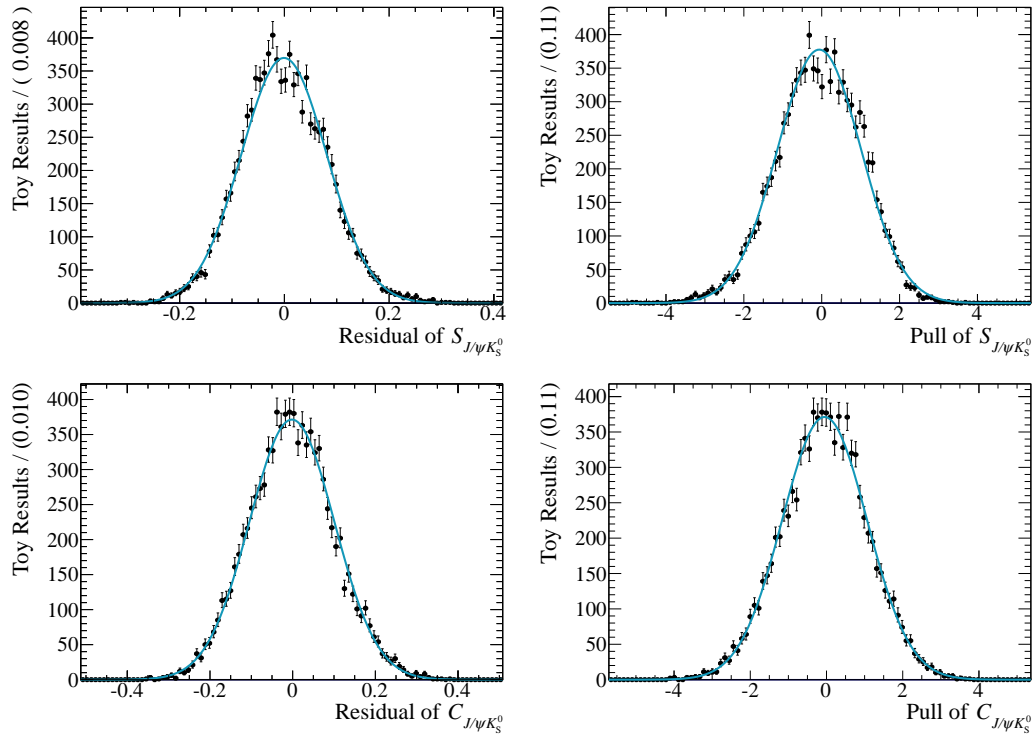
Fig. 7.5: Residual (left) and pull (right) distributions of the *CP* parameters $S_{J/\psi K_S^0}$ (top) and $C_{J/\psi K_S^0}$ (bottom) from a toy study using 10 000 simulated samples. Overlayed is the projection of a Gaussian fit to the distributions.

7.2 Preliminary results

The fit method described in Sec. 7.1 is applied to the $B^0 \to J/\psi K_S^0$ data sample after applying the full selection requirements described in Sec. 6.2. In the fit, the values of a total of 36 floating parameters are estimated, whilst leaving 4 parameters constrained and 9 parameters fixed. Prior to the final fit, both *CP* parameters, $S_{J/\psi K_S^0}$ and $C_{J/\psi K_S^0}$, were blinded by an unknown offset to avert observer bias. Only after completing the studies of systematic effects and their related uncertainties, which are presented in Sec. 7.4, the blinding was removed. The results quoted here refer to unblinded results if not specified otherwise.

While full fit results for all parameters will be quoted, the set of physics parameters λ_{phys},

$$\lambda_{\text{phys}} = (S_{J/\psi K_S^0}, C_{J/\psi K_S^0}, \tau, \Delta m, m_{B^0}), \tag{7.16}$$

which represent properties of the B^0 meson system and its decay into a $J/\psi K_S^0$ final state will be discussed more thoroughly.

7.2.1 Fit results

The fit results for the signal and background yields are given in Tab. 7.3, all other parameter estimates are quoted in Tab. 7.4. The projections of the PDFs to the distributions of the two sub-samples are shown in Figs. 7.1 to 7.4. The *CP* parameters are measured as

$$S_{J/\psi K_S^0} = 0.73 \pm 0.07,$$

$$C_{J/\psi K_S^0} = 0.03 \pm 0.09,$$

where the uncertainties are statistical only. These values are in excellent agreement with former measurements and their uncertainties lie in the expected range. Likewise, a good agreement with other measurements is observed for the estimates of the physics parameters of the B^0 meson system,

$$\Delta m = (0.52 \pm 0.04)\,\hbar\text{ps},$$

$$\tau = (1.516 \pm 0.018)\,\text{ps},$$

$$m_{B^0} = 5281.46 \pm {}^{0.10}_{0.11}\,\text{MeV}/c^2.$$

Only the B^0 meson mass shows a significant deviation from results of other measurements, in particular when comparing with the measurement of B meson masses performed by the LHCb experiment [140], which yields $m_{B^0} = (5279.58 \pm 0.32)\,\text{MeV}/c^2$. The main source of this discrepancy is related to an incorrect calibration of the momentum scale at the level of $< \mathcal{O}(0.15\%)$, which depends on the running conditions and has been corrected for in the quoted analysis. Implications of the momentum scale uncertainty on the measurement will be discussed more thoroughly within the scope of the analysis of systematic effects in Sec. 7.4.

The full correlation matrix of the fit is shown in Fig. 7.6. Besides a large correlation of $\rho(S_{J/\psi K_S^0}, C_{J/\psi K_S^0}) = 0.416$ between the *CP* parameters $S_{J/\psi K_S^0}$ and $C_{J/\psi K_S^0}$, the parameter $S_{J/\psi K_S^0}$ only shows correlations $\mathcal{O}(10\%)$ with the tagging calibration parameters and the production and tagging asymmetry parameters. In contrast, a high correlation of $\mathcal{O}(70\%)$ is observed between the $C_{J/\psi K_S^0}$ and the mass difference Δm. This can be explained by the

fact that the determination of $C_{J/\psi K_S^0}$ strongly depends on measuring the time-integrated asymmetry, which depends on the value of Δm, while the estimate for $S_{J/\psi K_S^0}$ is dominated by the sensitivity to the time-dependent asymmetry. This effect is further enhanced by only considering decay times $t > 0.3\,\text{ps}$, hereby eliminating any sensitivity of the fit to the amplitude of the asymmetry at $t = 0\,\text{ps}$, where the maximum of the cosine term is reached and the sine term vanishes.

Furthermore, strong correlations are observed among the yield parameters and among the parameters of the lognormal PDFs used for the descripton of the distribution of decay time resolution estimates σ_t. However, these are expected and have only negligible influence on the *CP* parameter determination.

Tab. 7.3: Yields of the signal and background components in each sub-sample of downstream and long candidates as determined in the fit.

Component	Long	Downstream
Signal	$2266 \pm^{52}_{51}$	$5931 \pm^{96}_{95}$
Background	$289 \pm^{26}_{25}$	2235 ± 74

7.2.2 Scans of profile-likelihood ratios

The parameter and uncertainty estimations from a likelihood fit depend on the value and the shape of the located minimum of the log-likelihood function. These estimations are only valid under certain criteria that need to be met by the log-likelihood function's minimum. For instance, a nearly parabolic shape and the absence of other local minima in the vicinity of the minimum are signs of a valid minimum. Although the algorithms used in this analysis, i.e. the MINUIT package, uses a variety of checks to ensure that the chosen minimum is correct, a check of the shape of the log-likelihood function's minimum gives confidence on the validity of the method. For this, the profile likelihood technique is employed.

First, the value of the log-likelihood at the minimum $\ln \mathcal{L}_{\text{min}}$ is computed by a fit in which all parameters, the parameter of interest μ and the nuisance parameters λ, are left free. Then, the parameter of interest is fixed at a value μ' that differs from its value at the minimum, μ_{min}. A new likelihood minimisation is performed in which the nuisance parameters are kept free, leading to a new value of the negative log-likelihood function $-\ln \mathcal{L}(\lambda', \mu')$. By scanning through different fixed values of μ, and by subtracting each new $-\ln \mathcal{L}$ value by its value at the minimum, the profile of the logarithm of the likelihood-ratio with respect to the minimum of the best fit is gained,

$$-\Delta \ln \mathcal{L}(\mu) = \ln \mathcal{L}_{\text{min}} - \ln \mathcal{L}(\mu) = \ln \frac{\mathcal{L}_{\text{min}}}{\mathcal{L}(\mu)} \,. \tag{7.17}$$

Applying this technique to the parameters $S_{J/\psi K_S^0}$ and $C_{J/\psi K_S^0}$ leads to the one-dimensional profile likelihood scans shown in Fig. 7.7.

In the limit of an infinite dataset and uncorrelated parameters, the log-likelihood profile of each parameter is expected to be parabolic. By adopting the properties of the likelihood
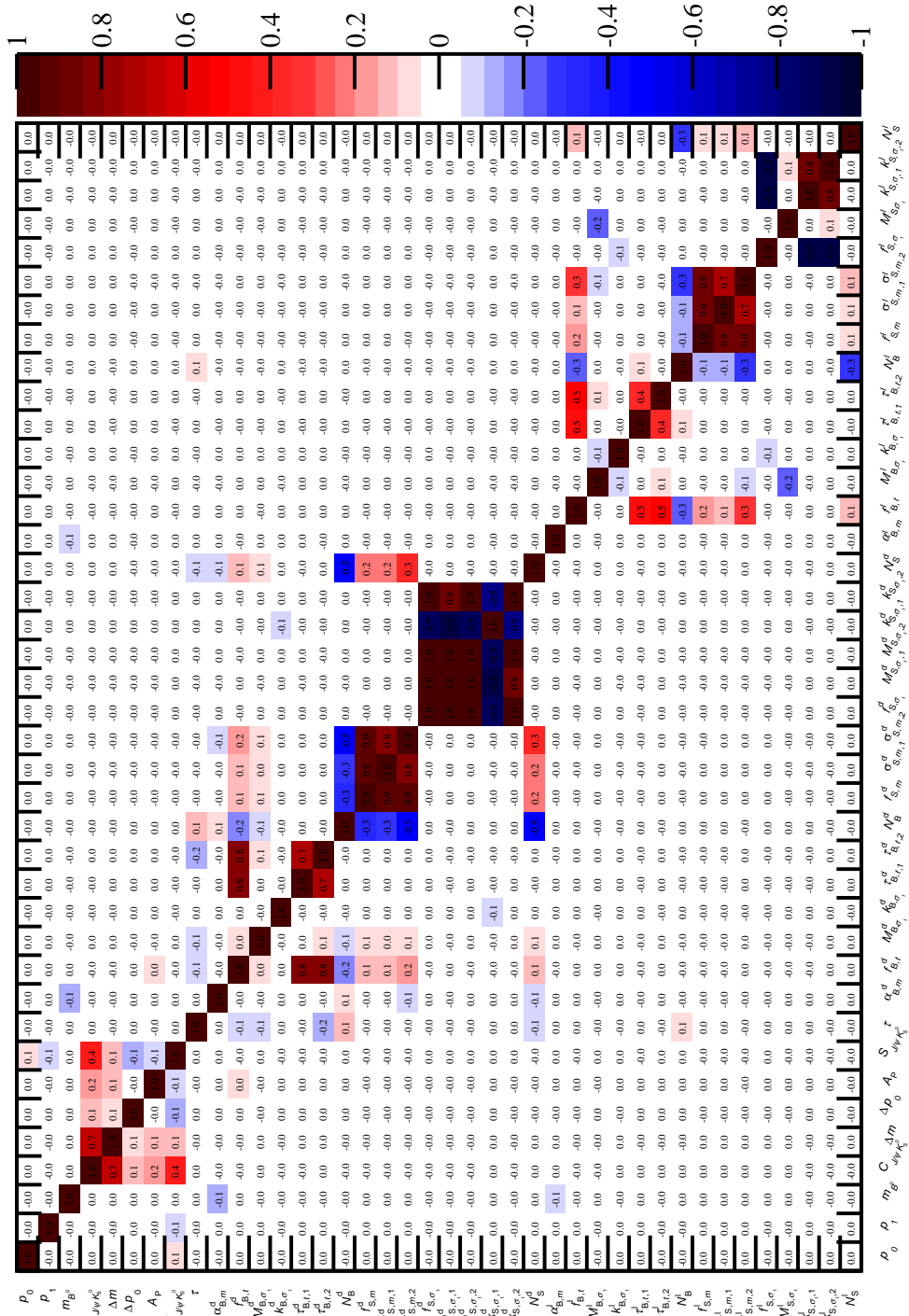
Fig. 7.6: Correlation matrix of the fit parameters. Positive (negative) correlations are represented by red (blue) colours, where darker colours denote higher correlations. Absolute correlations below 5% receive a white colour code.
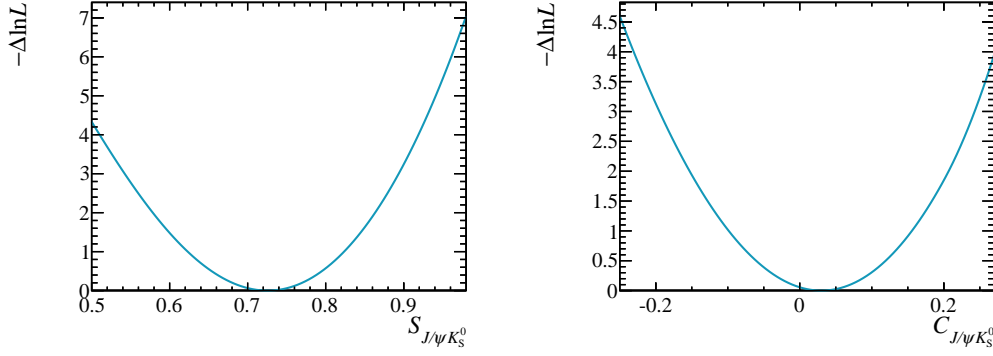
Fig. 7.7: One-dimensional projections of the negative log-likelihood function in the parameters $S_{J/\psi K_S^0}$ (left) and $C_{J/\psi K_S^0}$ (right) around the minimum determined in the best fit.

of a Gaussian function, the projection likelihood technique permits the determination of an approximate confidence interval, complementing the point estimates for the parameters of interest. In the frequentist interpretation, a confidence interval $[\mu_1, \mu_2]$ at a confidence level (CL) α will include the true value μ_t in a fraction α of repeated experiments. In particular, for a Gaussian likelihood function, the integral

$$\int_{-\mu_l}^{+\mu_l} d\mu \, \frac{1}{\sqrt{2\pi}} \exp\left(\frac{-\mu^2}{2}\right) = \mathrm{erf}\left(\frac{\mu_l}{\sqrt{2}}\right) \tag{7.18}$$

gives the confidence level for a confidence interval $[\mu_0 - \mu_l, \mu_0 + \mu_l]$ for a measured value μ_0 of the parameter μ. Translating this into the likelihood formalism, the confidence interval is given by the range of μ for which

$$-\Delta \ln \mathcal{L}(\mu) < \mu_l^2/2. \tag{7.19}$$

A widespread choice of the confidence level is 95%, in accordance with a 2σ statistical uncertainty, which in the case of a one-dimensional likelihood complies with $-\Delta \ln \mathcal{L}(\mu) < 1.92$. Applying this technique to the one-dimensional projection likelihoods of $S_{J/\psi K_S^0}$ and $C_{J/\psi K_S^0}$ results in the following one-dimensional confidence intervals:

$$S_{J/\psi K_S^0} \in [0.58, 0.86] \qquad \text{at 95\% CL}\,,$$

$$C_{J/\psi K_S^0} \in [-0.15, 0.20] \qquad \text{at 95\% CL}\,.$$

A more sophisticated frequentist method to determine confidence intervals that guarantees correct coverage is the Feldman-Cousins method [141]. An implementation of this method, leading to a two-dimensional confidence interval for $S_{J/\psi K_S^0}$ and $C_{J/\psi K_S^0}$, but using a considerably simpler fit model, is presented in Ref. [27].

Tab. 7.4: Full fit results. Asymmetric uncertainties are quoted only if differences are significant.

Model	Component	Parameter	Value	Unit
Reconstructed mass	Signal	m_{B^0}	$5281.46 \pm^{0.10}_{0.11}$	MeV/c^2
		$f^{\mathrm{d}}_{S,m}$	$0.38 \pm^{0.11}_{0.09}$	
		$\sigma^{\mathrm{d}}_{S,m,1}$	5.7 ± 0.6	MeV/c^2
		$\sigma^{\mathrm{d}}_{S,m,2}$	$10.8 \pm^{0.8}_{0.6}$	MeV/c^2
		$f^{\mathrm{l}}_{S,m}$	0.61 ± 0.10	
		$\sigma^{\mathrm{l}}_{S,m,1}$	5.8 ± 0.4	MeV/c^2
		$\sigma^{\mathrm{l}}_{S,m,2}$	$11.2 \pm^{1.1}_{0.9}$	MeV/c^2
	Background	$\alpha^{\mathrm{d}}_{B,m}$	$-1.6 \pm 0.8 \cdot 10^{-3}$	(MeV/c^2)$^{-1}$
		$\alpha^{\mathrm{l}}_{B,m}$	$-2.3 \pm 2.2 \cdot 10^{-3}$	(MeV/c^2)$^{-1}$
Decay time, tagging, *CP*	Signal	$S_{J/\psi K^0_S}$	0.73 ± 0.07	
		$C_{J/\psi K^0_S}$	0.03 ± 0.09	
		Δm	0.52 ± 0.04	$\hbar$ps^{-1}
		τ	1.516 ± 0.018	ps
	Background	$f^{\mathrm{d}}_{B,t}$	0.70 ± 0.06	
		$\tau^{\mathrm{d}}_{B,t,1}$	0.305 ± 0.027	ps
		$\tau^{\mathrm{d}}_{B,t,2}$	$1.33 \pm^{0.17}_{0.15}$	ps
		$f^{\mathrm{l}}_{B,t}$	$0.81 \pm^{0.07}_{0.08}$	
		$\tau^{\mathrm{l}}_{B,t,1}$	$0.161 \pm^{0.023}_{0.022}$	ps
		$\tau^{\mathrm{l}}_{B,t,2}$	$1.31 \pm^{0.46}_{0.31}$	ps
	Common	p_0	0.3918 ± 0.0017	
		p_1	1.032 ± 0.021	
		Δp_0	$0.0112 \pm^{0.0033}_{0.0034}$	
		A_{P}	-0.014 ± 0.013	
Decay time resolution	Signal	$f^{\mathrm{d}}_{S,\sigma_t}$	$0.85 \pm^{0.06}_{0.13}$	
		$M^{\mathrm{d}}_{S,\sigma_t,1}$	$0.0347 \pm^{0.0008}_{0.0009}$	
		$k^{\mathrm{d}}_{S,\sigma_t,1}$	0.725 ± 0.008	
		$M^{\mathrm{d}}_{S,\sigma_t,2}$	$0.063 \pm^{0.013}_{0.012}$	
		$k^{\mathrm{d}}_{S,\sigma_t,2}$	0.69 ± 0.04	
		$f^{\mathrm{l}}_{S,\sigma_t}$	$0.79 \pm^{0.11}_{0.16}$	
		$M^{\mathrm{l}}_{S,\sigma_t}$	$31.29 \pm 0.20 \cdot 10^{-3}$	
		$k^{\mathrm{l}}_{S,\sigma_t,1}$	$0.779 \pm^{0.017}_{0.012}$	
		$k^{\mathrm{l}}_{S,\sigma_t,2}$	$0.652 \pm^{0.031}_{0.041}$	
	Background	$M^{\mathrm{d}}_{B,\sigma_t}$	0.0422 ± 0.0005	
		$k^{\mathrm{d}}_{B,\sigma_t}$	0.657 ± 0.005	
		$M^{\mathrm{l}}_{B,\sigma_t}$	0.0300 ± 0.0008	
		$k^{\mathrm{l}}_{B,\sigma_t}$	$0.721 \pm^{0.014}_{0.015}$	

7.3 Cross-checks

Several cross-checks are performed to monitor the stability of the results, e.g. by comparing the results for different configurations of the LHCb magnet and for different running periods. All of these cross-checks indicate that the results obtained in the different configurations are in good agreement. Therefore, the discussion in this section is limited to the checks on differences between results in the sub-samples of downstream and long candidates, and the comparability of the purely time-integrated and purely time-dependent asymmetry measurement.

7.3.1 Differences between the long and downstream sub-sample

Although being fit simultaneously in the nominal fit, the sub-samples formed from reconstructed K_S^0 candidates with either downstream or long track pions exhibit differences in the mass and decay time resolutions, in the high decay time inefficiencies, and in the amount and type of backgrounds. Therefore, it is important to check the comparability of results gained in the two sub-samples.

Separate measurements in the sub-samples

Instead of using the full information of both the downstream and long sample, each sub-sample is fit separately with the corresponding PDF. The fit results for the *CP* parameters $S_{J/\psi K_S^0}$ and $C_{J/\psi K_S^0}$ in each sub-sample together with the differences in results are quoted in Tab. 7.5. No statistically significant differences are found, and hence, systematic differences that have not been accounted for seem to be negligible at the level of precision available in this dataset.

Tab. 7.5: Results of the separate fits to the downstream and long sample. Quoted are the estimates for the parameters $S_{J/\psi K_S^0}$ and $C_{J/\psi K_S^0}$ and the differences Δ of the parameter values between the two fits. The uncertainty on the differences is calculated by addition in quadrature, as both sub-samples are independent.

Parameter	downstream	long	Δ
$S_{J/\psi K_S^0}$	0.78 ± 0.08	0.63 ± 0.11	0.15 ± 0.14
$C_{J/\psi K_S^0}$	0.08 ± 0.11	-0.09 ± 0.16	0.17 ± 0.19

Omitting the high decay time acceptance

As explained in Sec. 6.7, the high decay time acceptance is described by a linear efficiency $\epsilon(t)$ that decreases with decay time t. The extent of this efficiency drop is determined from fully simulated Monte Carlo samples, separately for the long and the downstream sub-samples. These different efficiencies, or rather inefficiencies, are accounted for in the nominal fit. Therefore, the B^0 meson lifetime parameter τ can be shared between the decay time PDFs of both sub-samples.

In the cross-check fit, the efficiency description is dropped from the PDF. Instead, two different B^0 lifetime parameters, τ^l for the long and τ^d the downstream sample, are used. These are then measured as

$$\tau^d = (1.522 \pm 0.022)\,\text{ps}\,, \quad \tau^l = 1.437 \pm^{0.032}_{0.030}\,\text{ps}\,. \tag{7.20}$$

In spite of large differences between the fitted lifetimes, the fit results for the *CP* parameters shows no significant changes. Hence, the high decay time acceptance and its description in the fit have only a negligible effect on the *CP* measurement.

7.3.2 Time-integrated and time-dependent sensitivity

In a further study, the sensitivity of the measurement to the purely time-dependent and the purely time-integrated asymmetries is examined, in contrast to the nominal measurement which exploits both. An issue in interpreting the time-integrated asymmetry is the lack of concurrent sensitivity for both *CP* parameters. Hence, the study is performed for a fixed value of $C_{J/\psi K_S^0} = 0.03$, as estimated in the nominal fit.

The purely time-dependent analysis is realised by first applying an sPlot to the reconstructed mass distribution to determine signal weights for each candidate. Then, the time-dependent asymmetry of the signal in terms of the tag decision d is calculated in bins of decay time. A fit to the resulting histogram is performed with the fit function

$$\mathcal{A}_{\text{obs}}(t) = \frac{\Delta p_0 + A_{\text{P}}(1 - 2\omega) + [(1 - 2\omega) + A_{\text{P}}\Delta p_0](S \sin \Delta mt - C \cos \Delta mt)}{1 + A_{\text{P}}S \sin \Delta mt - A_{\text{P}}S \cos \Delta mt}\,, \tag{7.21}$$

with $S = S_{J/\psi K_S^0}$ and $C = C_{J/\psi K_S^0}$. The time-dependent asymmetry can be derived from the full signal PDF of decay times and tags, see Eq. (7.12), while ignoring effects of the decay time resolution. The mistag ω is chosen via a mean mistag, i.e. $\omega = p_0$. Fixing all other parameters to their measured values in the nominal fit, the fit to the histogram estimates

$$S_{J/\psi K_S^0} = 0.77 \pm 0.08\,,$$

which is different from the full nominal fit result. The asymmetry histogram and the resulting fit function are shown in Fig. 7.8.

To measure the time-integrated asymmetry, the sample is likewise split into two sub-samples with either B^0 tags or $\bar{B}^0$ tags. Using an extended likelihood fit to the reconstructed mass, the fitted yields in each sample,

$$N_{B^0} = 3665 \pm 83\,, N_{\bar{B}^0} = 4465 \pm 86, \tag{7.22}$$

are used to calculate the measured time-integrated asymmetry

$$\mathcal{A}_{\text{int}} = \frac{N_{\bar{B}^0} - N_{B^0}}{N_{\bar{B}^0} + N_{B^0}} = 0.098 \pm 0.015\,. \tag{7.23}$$

As discussed in Sec. 5.1, the observed time integrated asymmetry (assuming $C_{J/\psi K_S^0} = 0$) should be related to $S_{J/\psi K_S^0}$, the overall dilution D, and the intrinsic asymmetry I via

$$\mathcal{A}_{\text{int}} = D \cdot S_{J/\psi K_S^0} + I\,. \tag{7.24}$$

Here, the complication arises from correctly determining the dilutions and intrinsic asymmetries. The overall dilution $\mathcal{D}$ is a product of all diluting effects, like the mixing induced dilution or the dilution from tagging inefficiencies. Likewise, the intrinsic asymmetry is a sum of the B^0–$\bar{B}^0$ production asymmetry, the flavour-dependent differences in the tagging efficiencies, and terms of higher order that correlate with the dilution. Additionally, decay time acceptances and selection criteria, like the $t > 0.3\,\mathrm{ps}$ cut, need to be taken into account. All of this is far beyond the scope of this cross-check. Therefore, a simplified approach using simulated toy datasets is employed. While scanning through values of the parameter $S_{J/\psi K_S^0}$, a high statistics dataset is produced at each scan point based on the full nominal PDF. For each of these datasets the resulting time-integrated asymmetry $\mathcal{A}_{\mathrm{int}}$ is calculated. Then, looking at the time-integrated asymmetry $\mathcal{A}_{\mathrm{int}}$ as a function of $S_{J/\psi K_S^0}$, as shown in Fig. 7.8, the estimate for $S_{J/\psi K_S^0}$ is

$$S_{J/\psi K_S^0} = 0.73 \pm 0.13 \,. \tag{7.25}$$

This result is in excellent agreement with the value obtained from the combined measurement. Interestingly, the uncertainty is 50% higher than the uncertainty in the purely time-dependent measurement. On the one hand, this shows that the time-integrated asymmetry gives some sensitivity to the measurement. On the other hand, it is clear that the time-dependent measurement is indispensable, as it gives the same additional sensitivity as a time-integrated asymmetry measurement with roughly twice the amount of data.
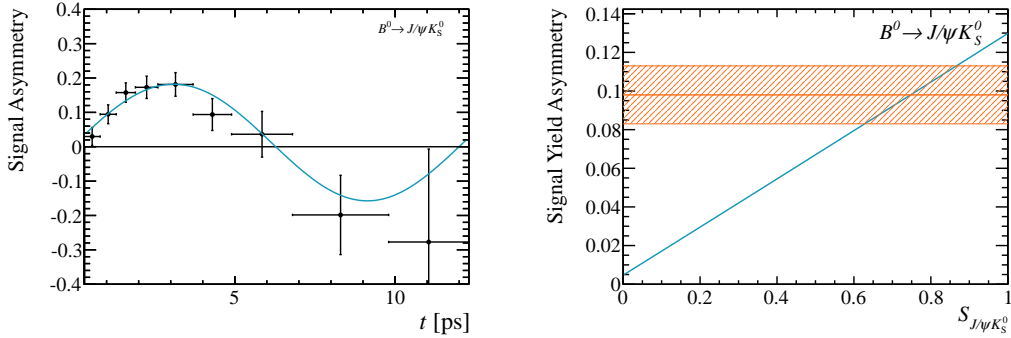

Fig. 7.8: Left: Result of the purely time-dependent study, using an asymmetry histogram of the signal candidates in bin of decay time t. The fit function is super-imposed (blue). Right: The time-integrated asymmetry as a function of $S_{J/\psi K_S^0}$ for fixed $C_{J/\psi K_S^0} = 0.3$ (blue), together with the measured value for the time-integrated asymmetry and the corresponding uncertainty band superimposed (orange).

In summary, the cross-check shows a reasonable agreement between the purely time-integrated and the purely time-dependent measurement. However, while correctly taking into account dilutions and asymmetries, both approaches ignore the uncertainties on the tagging calibration, the tagging asymmetries and the production asymmetry, as well as on Δm, τ, and $C_{J/\psi K_S^0}$. Hence, an underestimation of the uncertainties is expected.

Clearly, the presented studies are merely basic checks, and more sophisticated studies are necessary, especially in the case of a fully time-integrated measurement. The nominal analysis, exploiting both time-dependent and time-independent asymmetries, remains the best choice for an LHCb measurement of CP violation in $B^0 \rightarrow J/\psi K_S^0$ decays.

7.4 Studies of systematic effects

Several potential sources of systematic effects can bias the results, and many of them, like the B^0–$\bar{B}^0$ production asymmetry, have been taken into account in the nominal fit. Thus, these are properly described in the fit model and are covered by the statistical uncertainties. Others, like the limited knowledge of the accuracy of the tagging calibration have been studied, but still need to be interpreted in terms of systematic uncertainties on the results for the *CP* parameters $S_{J/\psi K_S^0}$ and $C_{J/\psi K_S^0}$. Often, the systematic uncertainties need to be estimated by using simulated pseudo-experiments (toy samples). These samples are generated while taking into account the considered systematic effect, but ignoring it in the fit. This procedure is repeated with a large number of samples to arrive at the residual and pull distributions of the parameters of interest, $S_{J/\psi K_S^0}$ and $C_{J/\psi K_S^0}$. If the average of pull and residual distributions is found to be compatible with 0, the systematic effect is assumed to be not biasing. Else-wise, the bias has to be corrected for, or a systematic uncertainty needs to be assigned.

Following the analysis steps, the systematic uncertainties from the selection requirements, the flavour tagging, the decay time description, together with uncertainties of the momentum and decay length scales that both affect the uncertainty on the decay time, and the uncertainties from the likelihood fit are evaluated and presented.

7.4.1 Best candidate selection

In the selection described in Sec. 6.2, only one candidate per event is retained: For events with multiple candidates, only the candidate with the lowest χ^2 of the decay tree fit is kept, hereby following a "best candidate" selection. This affects less than 4% of all candidates. In principle, such a best candidate selection can lead to a bias [142], as it distorts the decay tree fitter's χ^2 distribution and all correlated observables.

To roughly estimate a possible bias, a cross-check fit is performed using a data sample in which a "worst candidate" selection is applied: In case of multiple candidates in an event only the candidate with the highest decay tree fitter χ^2 is kept. Assuming a 96% correlation between the resulting and the nominal data sample, differences of

$$\Delta S_{J/\psi K_S^0} = 0.012 \pm 0.019, \quad \Delta C_{J/\psi K_S^0} = -0.028 \pm 0.026,$$

for the *CP* parameters are observed. These are compatible with no difference, and are therefore ignored. No systematic uncertainty is assigned. For future analysis, a random selection might offer an a priori unbiased "one candidate" selection.

Basically, the same arguments hold for choosing the associated primary vertex ("best primary vertex") of a candidate as the primary vertex with the lowest impact parameter χ^2. However, this is not further studied in the scope of this measurement.

7.4.2 Flavour tagging

Precise knowledge of the flavour tagging inefficiencies is required to correctly measure the *CP* parameters $S_{J/\psi K_S^0}$ and $C_{J/\psi K_S^0}$. Particularly, the dilution from wrong tags, $\mathcal{D}_\omega = (1 - 2\omega)$, with the mistag fraction ω needs to be assessed with high precision, as the observable asymmetry

scales with the product of the *CP* parameters and the dilution $\mathcal{D}_\omega$, see Ch. 5 for details. Thus, the under- or overestimation of $\mathcal{D}_\omega$ directly leads to an over- or underestimation of the *CP* parameters.

Tagging calibration

While the statistical uncertainties of the tagging parameters p_1 and p_0 have been taken into account in the fit, their systematic uncertainties need to be accounted for in the result. These systematic uncertainties of 0.012 on p_1 and 0.0076 on p_0 reflect the limited knowledge of the accuracy of the tagging calibration. They are assigned based on differences in the tagging calibration as observed in different channels, like $B^0 \rightarrow J/\psi K^{*0}$ and $B^0 \rightarrow D^- \pi^+$, and in datasets taken with different magnet polarities.

Using a large number of simulated pseudo-experiments, the according systematic uncertainty on the *CP* parameters is derived by varying the calibration parameters within their systematic uncertainties in the generation. Then, fits to the simulated datasets are performed using the nominal central values and statistical uncertainties for p_0 and p_1. The fit results are summarised in Tab. 7.6. The largest average shifts lead to an estimate of the systematic

Tab. 7.6: Means of the residual distributions of the parameters $S_{J/\psi K_S^0}$ and $C_{J/\psi K_S^0}$ from toy simulations. In each toy study, the tagging calibration parameters p_1 and p_0 are chosen within their systematic uncertainties in the generation, while using the nominal values in the fit.

p_0	p_1	$\Delta S_{J/\psi K_S^0}$	$\Delta C_{J/\psi K_S^0}$
$0.3920 + 0.0076$	$1.035 + 0.012$	-0.025	0.000
$0.3920 + 0.0076$	$1.035 - 0.012$	-0.031	0.001
$0.3920 - 0.0076$	$1.035 + 0.012$	0.034	0.001
$0.3920 - 0.0076$	$1.035 - 0.012$	0.028	0.001

uncertainties of

$$\sigma^{\text{ftc}}(S_{J/\psi K_S^0}) = 0.034\,, \quad \sigma^{\text{ftc}}(C_{J/\psi K_S^0}) = 0.001\,,$$

and hereby represents the largest systematic uncertainty on $S_{J/\psi K_S^0}$. Hopefully, with future measurements on larger datasets, the small differences observed in the various cross-checks can be better understood, leading to smaller systematic uncertainties.

Flavour-dependent tagging efficiency

In contrast to the production asymmetry A_P and the mistag fraction difference Δp_0 for B^0 and $\overline{B}^0$ mesons, the tagging efficiency difference $\Delta \epsilon_\text{tag}$ has been ignored in the fit—in excellent agreement with the measured central value of 0.000 ± 0.001. However, to account for the uncertainty of this measurement, another study using pseudo-experiments is performed. Similar to the other studies, two sets of data samples are produced: The first with a tagging efficiency difference of 0.001, the second with -0.001. Fits on the samples are performed

using the nominal central value of 0.0. Using once again the largest shift of the average residuals of the *CP* parameters, the systematic uncertainties are estimated as

$$\sigma^{\text{fte}}(S_{J/\psi K_S^0}) = 0.002, \quad \sigma^{\text{fte}}(C_{J/\psi K_S^0}) = 0.002,$$

which turn out to be tiny, especially for the $S_{J/\psi K_S^0}$ parameter when compared to the uncertainties from the tagging calibration.

7.4.3 Decay time description

A correct description of the decay time distribution is an important cornerstone of the analysis. Incorrect descriptions would affect both the time-integrated and time-dependent share of the analysis. The most obvious sources of systematic effects are related to the decay time resolution and to the decay time acceptance.

Decay time resolution

As explained in Sec. 6.6, the per-event resolution model is calibrated with prompt *J/ψ* background that fulfils most of the nominal selection criteria. In a first attempt to identify systematic effects, studies with fully simulated samples are performed.

First, the agreement of the decay time resolution observed in prompt $B^0 \to J/\psi K_S^0$ candidates formed from true prompt *J/ψ* mesons compared to the resolution of true B^0 mesons decaying to $J/\psi K_S^0$ final states is checked. Using an inclusive *J/ψ* MC sample, this assumption is found to be incorrect for the average resolution, however, the parameters of the per-event resolution model are found to be consistent between the samples. Hence, no systematic uncertainties are assigned.

Second, the method of determining the decay time distribution of B^0 candidates formed from prompt *J/ψ* candidates using the sPlot method is studied. As explained in Sec. 6.6, the reconstructed mass of the *J/ψ* candidates is used as the discriminating observable in the sPlot. However, the sPlot method is only valid if the signal and background *J/ψ* mass distributions are uncorrelated to the decay time and decay time resolutions. A study with a simulated sample of truth-matched *J/ψ* candidates shows, that a small correlation between the *J/ψ* mass and the residuals $(t - t')$ of reconstructed and simulated decay time is present. Therefore, the sPlot approach has only limited validity. This needs to be taken into account in the evaluation of systematic uncertainties.

Third, the dependencies of the scale factors s_i on the decay time are studied. On a simulated sample, the truth-matched $B^0 \to J/\psi K_S^0$ candidates are split into bins of increasing true decay time t'. In each bin, a single Gaussian per-event resolution is fitted to the pull distribution $(t - t')/\sigma_t$. Here, the width of the Gaussian represents the scale factor in that specific bin. A dependency of the scale factors on the true decay time t' is observed, with a maximum decrease of 5% with respect to the scale factor in the bin at 0 ps [26].

A systematic uncertainty is estimated using toy simulations. The study is designed such that it easily covers for the sources of systematic uncertainties and for fixing of the resolution model in the fit. Though, as the resolution is found to have a negligible effect on the overall dilution, the resulting uncertainties are expected to be small.

Using the full PDF, two types of toy samples are generated. The first type uses scale factors that are scaled down by 50% with respect to the measured values, the second type uses scale factors that are twice as large than measured. The fits to the simulated samples are performed with the nominal PDF and scale factors. In the resulting pull and residual distributions of the $S_{J/\psi K_S^0}$ and $C_{J/\psi K_S^0}$ parameters, the largest differences to the generated values are determined. These are used as estimates of the systematic uncertainty, resulting in uncertainties of

$$\sigma^{\mathrm{res}}(S_{J/\psi K_S^0}) = 0.0014\,, \quad \sigma^{\mathrm{res}}(C_{J/\psi K_S^0}) = 0.0022\,,$$

which are smaller than 10% of the parameter's statistical uncertainties.

Decay time acceptances

The cross-check on the effect of the high decay time acceptance has been described in Sec. 7.3.1. For the decay time acceptance from reconstruction inefficiencies at low decay times, another study with simulated samples generated from the full PDF is performed. In the generation, the decay time acceptance caused by the trigger requirements, see Sec. 6.7, is accounted for using the efficiency histogram. Similar to the nominal data fit, the acceptance is omitted in the PDF that is used to fit the samples. The means of the resulting residual distributions of the $S_{J/\psi K_S^0}$ and $C_{J/\psi K_S^0}$ parameters are shifted to small negative values. These shifts are used as estimates of the systematic uncertainties,

$$\sigma^{\mathrm{acc}}(S_{J/\psi K_S^0}) = 0.0024\,, \quad \sigma^{\mathrm{acc}}(C_{J/\psi K_S^0}) = 0.0062\,.$$

7.4.4 Momentum scale and z-scale

An upper bound of 0.15% for the uncertainty of the momentum scale has been determined by the LHCb tracking group, following procedures used in LHCb's measurement of b hadron masses [140], which is described more throughly in Ref. [143]. Measuring the deviations of the reconstructed mass of $J/\psi \to \mu^+\mu^-$ candidates with respect to their known masses in different data taking periods allows to estimate the momentum scale uncertainty, which affects both the reconstructed mass and the decay time of the B^0 candidates. The extent of the effect is studied with fully reconstructed and truth-matched decays of $B^0 \to J/\psi K_S^0$ in a simulated sample. First, the generated momenta of the final state particles, i.e. muons and pions, are scaled by 1.0015. Then, the resulting reconstructed masses and decay time are calculated and compared with the true, generated values.

The reconstructed decay time after scaling the momenta is determined as

$$t_{\mathrm{rec}} = \frac{l}{c\beta\gamma} = \frac{l\,m_{\mathrm{rec}}}{c\,|\boldsymbol{p}|}\,,$$

where l represents the true flight distance, $\beta\gamma$ are Lorentz factors, and the momentum $\boldsymbol{p}$ is given by the sum of the three-momenta of the final state particles after scaling. Similar to the nominal analysis, no mass constraints are applied in the determination of the decay time. Hence, the reconstructed mass m_{rec} is the invariant mass of the sum of four-momenta of the final state particles. In first order, this leads to a cancellation of the momentum scale in the

determination of t_{rec}. Still, higher order effects lead to a relative shift smaller than $\mathcal{O}(10^{-4})$, as shown in Fig. 7.9.

In contrast, large absolute deviations are observed for the reconstructed mass. Similar to the reconstructed mass used in the *CP* analysis, mass constraints for the intermediate J/ψ and K_S^0 candidates are applied after scaling the final state momenta. The distribution of mass shifts $\delta m_{J/\psi K_S^0} = m_{J/\psi K_S^0, \text{true}} - m_{J/\psi K_S^0, \text{rec}}$ are shown in Fig. 7.9. It indicates that the largest observed shifts are at the level of $4 \,\mathrm{MeV}/c^2$, while the average shift is $3.2 \,\mathrm{MeV}/c^2$, in good agreement with the shift of approximately $2 \,\mathrm{MeV}/c^2$ observed in data.
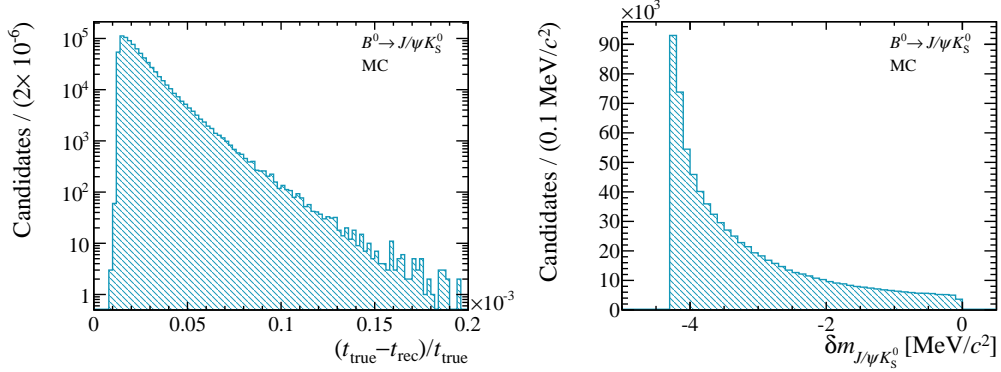
Fig. 7.9: Results of scaling the momenta of the final state particles: The relative time shift of the reconstructed time t_{rec} with respect to the true time t_{true} (left, logarithmic scale) and the absolute shifts of reconstructed masses $\delta m_{J/\psi K_S^0}$ with respect to the true mass of the B^0 candidate (right). In the latter study, mass constraints on the J/ψ and K_S^0 candidates are applied.

The uncertainty of the z-scale is estimated to be less than 0.1%. In a worst case scenario, this relative uncertainty directly enters the uncertainty on the decay length l and consequently the uncertainty on the decay time. Combined with the uncertainty on the momentum scale, this results in a maximum uncertainty of 0.1% on the reconstructed decay time. This might affect a lifetime measurement but has negligible effect on the *CP* measurement. Hence, no systematic uncertainty is assigned.

7.4.5 Fit model

Systematic uncertainties related to the fit method are evaluated. They cover the effects of mis-modelling the distributions in data and include the uncertainties on the reliability of the fit results.

Background treatment

The PDFs describing the signal component have been developed on the basis of studies with large samples of fully simulated LHCb events. Yet, it is impossible to follow the same strategy for the background components. Creating a realistic, fully simulated background sample that is consistent with the amount of data before applying trigger and selection criteria is not feasible due to storage and computing limitations. Hence, the background model is chosen

empirically. An incorrect model, especially for the decay time distribution, might bias the fit results.

Relying on the assumption that the mass distribution of signal and background component are well described by the chosen PDFs, a fit to the mass distributions is used to determine signal sPlot weights for each event. These are then used to fit the signal component PDFs to the resulting signal distributions in all other observables. By construction, no PDFs describing the background component are needed. The fit yields differences to the result from the full, nominal fit. These are used as estimates of the uncertainty on the background model,

$$\sigma^{\text{bkg}}(S_{J/\psi K_S^0}) = 0.0012 \,, \quad \sigma^{\text{bkg}}(C_{J/\psi K_S^0}) = 0.0088 \,.$$

Bias of the fit method

The bias on the *CP* parameter estimates from the likelihood fit have been evaluated in Sec. 7.1.4. In the study, using a large number of pseudo-experiments, a small but significant bias is found. Normally, biases need to be corrected for in the final result. However, the source of this bias has not been thoroughly studied and could be related to the complex PDF and some of the highly correlated nuisance parameters. Furthermore, intensive studies on its dependency on the size of the dataset are needed. Hence, the observed fit bias itself is not an accurate estimate of the bias, but is rather an estimate of the systematic uncertainty from fit biases. Using the product of the shift of the pull distribution and the statistical uncertainty of the parameter estimates, the systematic uncertainty on the *CP* parameters is assessed as

$$\sigma^{\text{fit}}(S_{J/\psi K_S^0}) = 0.0042 \,, \quad \sigma^{\text{fit}}(C_{J/\psi K_S^0}) = 0.0045 \,.$$

7.4.6 Combined systematic uncertainty

The total systematic uncertainties are listed in Tab. 7.7. Combining the different contributions by summing in quadrature results in total systematic uncertainties on $S_{J/\psi K_S^0}$ and $C_{J/\psi K_S^0}$ of

$$\sigma^{\text{tot}}(S_{J/\psi K_S^0}) = 0.036 \quad \text{and} \quad \sigma^{\text{tot}}(C_{J/\psi K_S^0}) = 0.012 \,.$$

The by far largest source of systematic uncertainty on $S_{J/\psi K_S^0}$ originates from the systematic uncertainty on the tagging calibration. In contrast, the largest systematic uncertainty on $C_{J/\psi K_S^0}$ is a result of potential mis-modelling of the background component, closely followed by the uncertainty from ignoring decay time acceptances in the fit. Still, the total uncertainty is dominated by the limited size of the data sample.

Tab. 7.7: Summary of the systematic uncertainties. The total systematic uncertainty is determined by summing the single uncertainties in quadrature.

Origin	$\sigma(S_{J/\psi K^0_S})$	$\sigma(C_{J/\psi K^0_S})$
Tagging calibration	0.034	0.001
Tagging efficiency difference	0.002	0.002
Decay time resolution	0.001	0.002
Decay time acceptance	0.002	0.006
Background model	0.012	0.009
Fit bias	0.004	0.005
Total	0.036	0.012

7.5 Final result

A measurement of time-dependent *CP* violation in approximately 8000 reconstructed $B^0 \rightarrow J/\psi K^0_S$ decays with assigned flavour tagging information is performed. The candidates are reconstructed in a dataset corresponding to $1\,\mathrm{fb}^{-1}$ of *pp* collisions collected by the LHCb experiment in 2011 at a centre-of-mass energy of $\sqrt{s} = 7\,\mathrm{TeV}$. The measurement is performed in terms of an unbinned likelihood fit exploiting both time-dependent and time-integrated asymmetries in the data sample. With an effective decay time resolution of less than 66 fs and an effective tagging efficiency of $(2.38 \pm 0.27)\%$, the *CP* violation parameters are measured as

$$S_{J/\psi K^0_S} = 0.73 \pm 0.07\,(\text{stat.}) \pm 0.04\,(\text{syst.}) \quad \text{and}$$
$$C_{J/\psi K^0_S} = 0.03 \pm 0.09\,(\text{stat.}) \pm 0.01\,(\text{syst.}).$$

The determined lifetime and oscillation frequency of the B^0 meson

$$\tau = 1.516 \pm 0.018\,\mathrm{ps},$$
$$\Delta m = 0.52 \pm 0.04\,\hbar\mathrm{ps},$$

are consistent with other measurements. A plot of the background corrected time-dependent asymmetry is shown in Fig. 7.10.
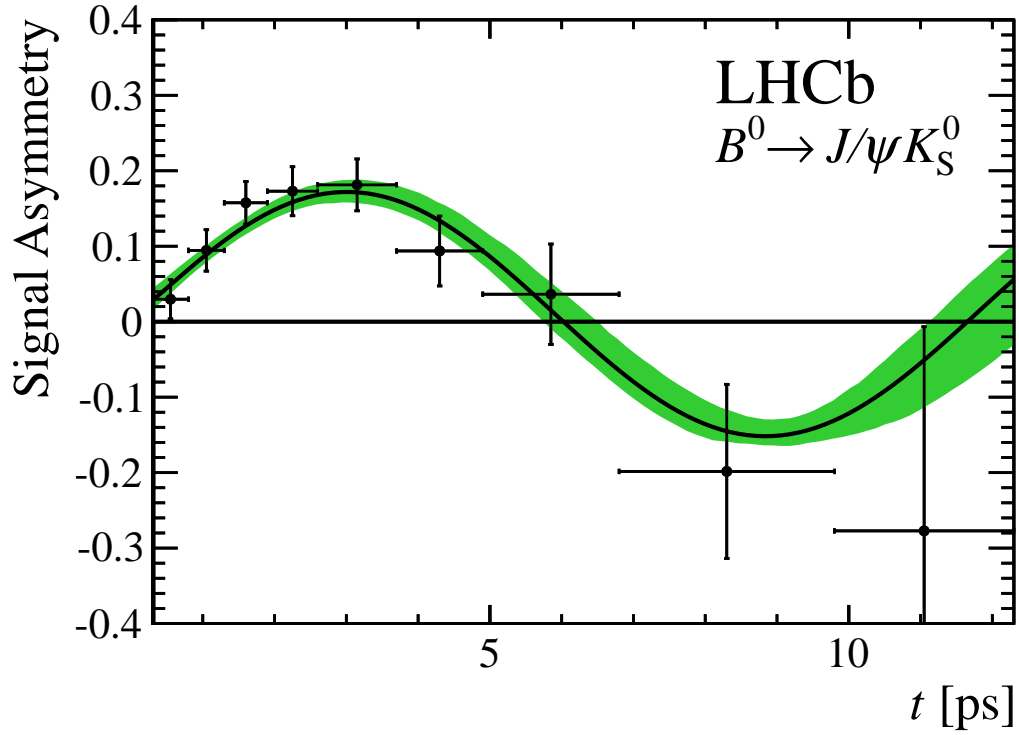
Fig. 7.10: Time-dependent asymmetry $(N_{\bar{B}^0}(t) - N_{B^0}(t)/(N_{\bar{B}^0}(t) + N_{B^0}(t))$. Here, $N_{B^0}(t)$ $(N_{\bar{B}^0}(t))$ represents the number of reconstructed $B^0 \to J/\psi K^0_S$ decays at decay time t with a B^0 $(\bar{B}^0)$ tag. The data points are obtained using the sPlot technique: Signal weights are assigned to each data point based on a fit to the distribution of reconstructed masses. The solid, black curve is a projection of the PDF. The green band corresponds to the statistical uncertainty.

8 Conclusion and Outlook

The Large Hadron Collider beauty experiment builds upon the success of more than four decades of flavour physics experiments, which have considerably expanded our knowledge and understanding of the nature of elementary particle interactions. A result of these and other efforts of particle physicists is the Standard Model of particle physics, which has turned out to be capable of describing the experimental data in a wide range of energies. Even a candidate for the long sought Higgs particle has been found, once again demonstrating the predictive power of the Standard Model. Yet, open questions, which are closely linked to particle physics, remain: What are the elementary constituents of dark matter? What role does gravity play in particle interactions? Why do we live in a universe dominated by matter, while anti-matter seems to have vanished?

Together with the other experiments at the Large Hadron Collider, LHCb probes the regime of high intensities to search for signs of New Physics, which could hint at answers to the aforementioned questions. As an experiment specialised in flavour physics, LHCb's focus lies on indirect searches for New Physics through precision measurements in decays of heavy quark hadrons like the B mesons. Both, rare decays and CP violating processes in these systems offer observables with precise predictions from the Standard Model, hereby allowing for stringent tests of our current understanding of particle physics. The sector of CP violation, in particular, could provide an insight to the mechanisms that have led to a matter dominated universe.

This thesis describes the LHCb measurement of CP violation in decays of B^0 mesons and their anti-particles into the $J/\psi K_S^0$ final state, with subsequent decays of $J/\psi \rightarrow \mu^+\mu^-$ and $K_S^0 \rightarrow \pi^+\pi^-$. Here, the interference of B^0–$\bar{B}^0$ mixing with the decay via a $b \rightarrow c\bar{c}s$ transition into a common final state leads to a time-dependent asymmetry between the differential decay rates of the B^0 and $\bar{B}^0$ flavour states. Two parameters, $S_{J/\psi K_S^0}$ and $C_{J/\psi K_S^0}$, describe the interference and direct CP violation, respectively, and are measured as

$$S_{J/\psi K_S^0} = 0.73 \pm 0.07 \,(\text{stat.}) \pm 0.04 \,(\text{syst.}) \quad \text{and}$$
$$C_{J/\psi K_S^0} = 0.03 \pm 0.09 \,(\text{stat.}) \pm 0.01 \,(\text{syst.}) \,,$$

with a correlation coefficient of $\rho = 0.416$. This result is in excellent agreement with former measurements of $S_{b \rightarrow c\bar{c}s}$ and $C_{b \rightarrow c\bar{c}s}$ in $b \rightarrow c\bar{c}s$ mediated decays of B^0 mesons, see Fig. 8.1, and represents the first statistically significant measurement of interference CP violation in B mesons at a hadron collider. This is particularly remarkable given that the analysis is limited to the LHCb data taken in 2011, in which both LHC and LHCb have not reached their nominal performance. Thus, the measurement demonstrates the capabilities of LHCb in the field of time-dependent CP measurements, and illustrates the in-depth understanding of all the involved technicalities. These range from triggering, reconstructing, and selecting interesting
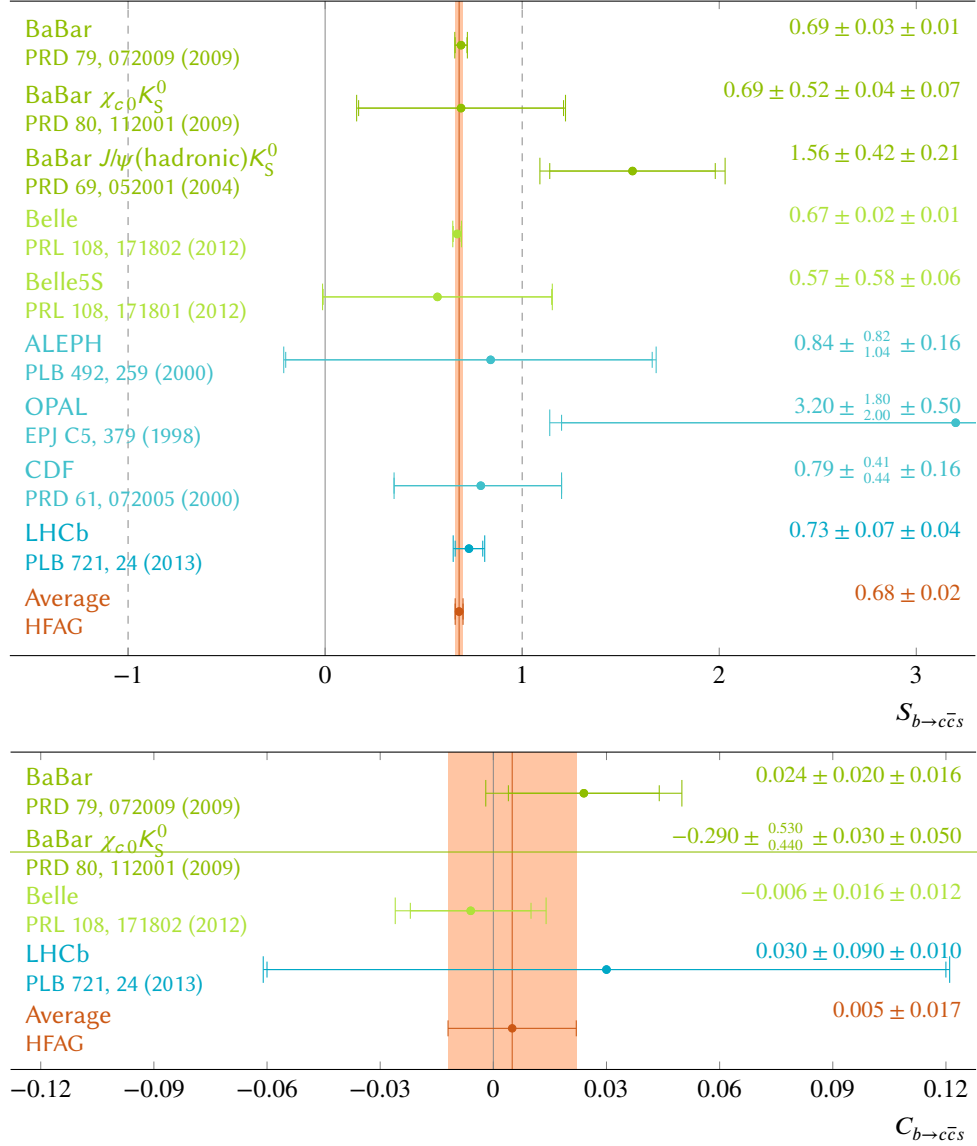
Fig. 8.1: Overview on measurements of the *CP* violation observables $S_{b\to c\bar{c}s}$ and $C_{b\to c\bar{c}s}$, including the LHCb measurement presented in this thesis, as well as the averages as calculated by the Heavy Flavour Averaging Group [12].

decay modes, to tagging the initial flavour of each *B* candidate, and measuring the resulting flavour tagging performance. Likewise, the measurement highlights LHCb's excellent vertex reconstruction and resulting decay time resolution. Other aspects, for instance the studies of the production rate asymmetry for $B^0/\bar{B}^0$ mesons, or the analysis of the background contribution and composition, emphasize the special challenges of a precision experiment at a hadron collider like the LHC.

Besides representing a perfect reference channel for other time-dependent CP measurements in LHCb that require flavour tagging, like $B_s^0 \to J/\psi\phi$ or $B_s^0 \to J/\psi\pi^+\pi^-$, $B^0 \to J/\psi K_S^0$ is the gold-plated channel for measurement of CP violation in the B^0 system. Its CP parameters allow for a theoretically clean determination of the CKM angle β, as $S = \sin 2\beta$ for $C = 0$. Though, the presented LHCb measurement still suffers from an experimental uncertainty which is more than a factor of 4 larger than the results of the B factories, BaBar and Belle, which include several other final states in B^0 decays via $b \to c\bar{c}s$ transitions. However, limiting the comparison to the measurements with $J/\psi K_S^0$ final states only, LHCb will already reach a similar sensitivity when including the data sample collected in 2012.

In its most recent measurement, Belle uses its full dataset of $7.7 \cdot 10^8$ $B\bar{B}$ pairs, of which approximately 12 500 are reconstructed in the $B^0 \to J/\psi K_S^0$ mode [63]. Thus, a reconstruction efficiency of approximately 45% can be estimated. The effective tagging efficiency of $\varepsilon_{\text{tag}}D^2 = (29.8 \pm 0.4)\%$ results in an effective yield of 3725 perfectly tagged events, which allows for the world's best measurement of $S_{J/\psi K_S^0}$ and $C_{J/\psi K_S^0}$ with statistical uncertainties of 0.029 and 0.021, respectively. In contrast, the LHCb result with the 2011 dataset, which corresponds to approximately $2 \cdot 10^{11}$ $B^0/\bar{B}^0$ mesons produced in the pp collisions at LHCb, uses $\approx 25\,000$ reconstructed $B^0 \to J/\psi K_S^0$ signal candidates. Thus, the reconstruction efficiency of only about 1% still leaves a larger sample of $B^0 \to J/\psi K_S^0$ decays than Belle. Yet, the effective tagging efficiency of $(2.38 \pm 0.27)\%$ reduces the effective yield to 598 perfectly tagged candidates, six times less than in the Belle sample. This clearly explains the larger statistical uncertainties of the LHCb measurement of $S_{J/\psi K_S^0}$ and $C_{J/\psi K_S^0}$.

To reach the goal of an LHCb measurement with a competitive result using the combined 2011 and 2012 dataset, an optimised analysis is needed, which includes the same-side pion tagger and extends the selection to more trigger lines. Furthermore, extrapolating the current performance to an upgraded LHCb detector, a statistical precision on $S_{J/\psi K_S^0}$ of ± 0.006 is expected [144]. Hence, assuming that the systematic uncertainties can be controlled at a comparable level, LHCb can perform a best measurement of the CKM parameter β.

At the same time, the further reduction of the experimental uncertainties in measurements of the $S_{b \to c\bar{c}s}$ and $C_{b \to c\bar{c}s}$ parameters will at some point require a better control of theoretical uncertainties in the determination of the CKM angle β. In particular the degree of penguin pollution, which can safely be ignored at the current experimental precision, needs to be further understood. Here, experimental input from a time-dependent CP measurement in the $B_s^0 \to J/\psi K_S^0$ channel, which is linked to $B^0 \to J/\psi K_S^0$ through flavour symmetries, could provide valuable constraints. The analysis presented in this thesis, including the various strategies and supporting studies that have led to the LHCb measurement of CP violation in the $B^0 \to J/\psi K_S^0$ channel, paves the way for a first CP measurement in $B_s^0 \to J/\psi K_S^0$ with the LHCb data taken in 2011 and 2012.

Appendix

1 Controlling penguin pollution with $B_s^0 \to J/\psi K_S^0$

In view of the search for New Physics and with the increasing experimental precision of *CP* measurements in $B^0 \to J/\psi K_S^0$, a stronger effort in controlling higher order Standard Model effects from a theoretical point of view is needed. In particular, the extent of penguin pollution in the decay amplitudes needs to be precisely estimated. Approaches for the $B^0 \to J/\psi K_S^0$ channel and others have been discussed in Refs. [55–57, 62, 145] and are summarised in this appendix for completeness.

Starting from the expressions for the *CP* observables in the $B^0 \to J/\psi K_S^0$ channel as quoted in Ch. 3, and now taking into account the sub-leading penguin contributions, the full expressions read as

$$
\begin{aligned}
S_{J/\psi K_S^0} &= \frac{\sin\phi_d + 2\epsilon a \cos\theta \sin(\phi_d + \gamma) + \epsilon^2 a^2 \sin(\phi_d + 2\gamma)}{1 + 2\epsilon a \cos\theta \cos\gamma + \epsilon^2 a^2}, \\
C_{J/\psi K_S^0} &= -\frac{2\epsilon a \sin\theta \sin\gamma}{1 + 2\epsilon a \cos\theta \cos\gamma + \epsilon^2 a^2},
\end{aligned}
\tag{1}
$$

with the dominant phase $\phi_d = 2\beta$. To determine the phase ϕ_d, it is useful to evaluate the expression

$$
\frac{S_{J/\psi K_S^0}}{\sqrt{1 - C_{J/\psi K_S^0}^2}} = \sin(\phi_d + \Delta\phi_d)
\tag{2}
$$

with

$$
\tan\Delta\phi_d = \frac{2\epsilon a \cos\theta \sin\gamma + \epsilon^2 a^2 \sin 2\gamma}{1 + 2\epsilon a \cos\theta \cos\gamma + \epsilon^2 a^2 \cos 2\gamma}.
\tag{3}
$$

The hadronic parameters a and θ from the doubly Cabibbo-suppressed penguin contributions in the decay amplitude of $B^0 \to J/\psi K_S^0$, which have been neglected in the considerations in Sec. 3.4, cannot be calculated using perturbative QCD. Values of $a \approx 0.2$ could lead to $\Delta\phi_d$ up to 0.02, leading to a theoretical uncertainty just below the current experimental precision. Ignoring these effects might result in an under- or overestimation of the mixing phase and hereby fake a consistency or inconsistency of the Standard Model's CKM picture. As theoretical calculations for the parameters suffer from large uncertainties, they need to be controlled using other experimental measurements.

A common approach is to relate the hadronic decay parameters in $B^0 \to J/\psi K_S^0$, i.e. a and θ, to other similar parameters in other non-leptonic decay modes of B mesons by applying symmetry relations for the strong interactions. For instance, flavour $SU(3)$ assumes that the u, d, and s quarks are light compared to the involved hadron masses and therefore the

strong interactions are dominantly flavour independent. This allows to relate the hadronic parameters of the decay amplitude of $\bar{B}^0 \to J/\psi \bar{K}^0$ to other decays of B^+, B^0, and B_s^0 mesons into a J/ψ and a pseudoscalar meson P, like $B^- \to J/\psi K^-$, $\bar{B}^0 \to J/\psi \pi^0$, $B^- \to J/\psi \pi^-$, while taking into account the sub-leading contributions. However, as flavour $SU(3)$ is broken, correction terms from $SU(3)$ breaking need to be taken into account to correctly relate the observables in the different decay channels [62] to make a reasonable estimate of $\Delta\phi_d$.

One of these $B \to J/\psi P$ channels that could be measured by the LHCb experiment is the decay $B_s^0 \to J/\psi K_S^0$, which is caused by $b \to c\bar{c}d$ and is related to the $B^0 \to J/\psi K_S^0$ decay by U-spin (an $SU(2)$ subgroup of the flavour $SU(3)$), i.e. the assumption of interchangeability of s and d in the strong interactions. In the further discussion, primed parameters will be used when describing the $b \to c\bar{c}d$ transitions, analogously to their unprimed counterparts in the $b \to c\bar{c}s$ transitions discussed in Sec. 3.3. Hence, the decay amplitude can be written as

$$A(B_s^0 \to J/\psi K^0) = -\lambda \mathcal{A}'(1 - a' e^{i\theta'} e^{i\gamma}), \tag{4}$$

where the primed $\mathcal{A}'$, a', and θ' are identical to the unprimed $\mathcal{A}$, a, and θ in $B^0 \to J/\psi K_S^0$ if U-spin symmetry holds perfectly. In contrast to $B^0 \to J/\psi K_S^0$, the penguin diagrams are not suppressed with ϵ. This allows for an access to the penguin contributions and their related parameters.

In analogy to the considerations in Sec. 3.3, the ratio of decay amplitudes of B_s^0 and $\bar{B}_s^0$ to $J/\psi K_S^0$ is given as

$$\frac{\bar{A}'_{J/\psi K_S^0}}{A'_{J/\psi K_S^0}} = -\frac{V_{cs}V_{cd}^*}{V_{cs}^*V_{cd}} e^{i2\epsilon'_K} \frac{V_{cb}V_{cd}^*}{V_{cb}^*V_{cd}} \frac{1 - a' e^{i\theta'} e^{-i\gamma}}{1 - a' e^{i\theta'} e^{+i\gamma}}. \tag{5}$$

The B_s^0–$\bar{B}_s^0$ mixing is mediated through box diagrams, where the dominant contribution comes from the box diagram with t quark in the loop, and hence

$$\frac{q'}{p'} = \frac{V_{tb}^*V_{ts}}{V_{tb}V_{ts}^*}. \tag{6}$$

Consequently, the full expression for the CP parameter $\lambda'_{J/\psi K_S^0}$ is given as

$$\lambda'_{J/\psi K_S^0} = -\frac{V_{tb}^*V_{ts}}{V_{tb}V_{ts}^*} \frac{V_{cs}V_{cd}^*}{V_{cs}^*V_{cd}} \frac{V_{cb}V_{cd}^*}{V_{cb}^*V_{cd}} \frac{1 - a' e^{i\theta'} e^{-i\gamma}}{1 - a' e^{i\theta'} e^{+i\gamma}}, \tag{7}$$

where the negligible phase ϵ'_K has been omitted. As $\Delta\Gamma_s$, the width difference between the heavy and light mass eigenstates of the B_s^0 can not be neglected, the time-dependent decay rates are given as

$$\Gamma(B_s^0(t) \to J/\psi K_S^0) = \frac{\tilde{A}'}{2} e^{-\Gamma_s t} \left[\quad \cosh\left(\frac{\Delta\Gamma_s}{2}t\right) \quad + D'_{J/\psi K_S^0} \sinh\left(\frac{\Delta\Gamma_s}{2}t\right) \right.$$
$$\left. + C'_{J/\psi K_S^0} \cos\left(\Delta m_s t\right) - S'_{J/\psi K_S^0} \sin\left(\Delta m_s t\right) \quad \right], \qquad (8a)$$

$$\Gamma_s(\bar{B}_s^0(t) \to J/\psi K_S^0) = \frac{\tilde{A}'}{2} e^{-\Gamma_s t} \left[\quad \cosh\left(\frac{\Delta\Gamma_s}{2}t\right) \quad + D'_{J/\psi K_S^0} \sinh\left(\frac{\Delta\Gamma_s}{2}t\right) \right.$$
$$\left. - C'_{J/\psi K_S^0} \cos\left(\Delta m_s t\right) + S'_{J/\psi K_S^0} \sin\left(\Delta m_s t\right) \quad \right], \qquad (8b)$$

with $\tilde{A}' = |A'_{J/\psi K_S^0}|^2(1 + |\lambda'_{J/\psi K_S^0}|^2)$, the decay width Γ_s of the B_s^0 meson, the B_s^0–$\bar{B}_s^0$ mixing frequency Δm_s. The *CP* observables $C'_{J/\psi K_S^0}$, $S'_{J/\psi K_S^0}$, and $D'_{J/\psi K_S^0}$ are given as

$$C'_{J/\psi K_S^0} = \frac{2a' \sin\theta' \sin\gamma}{1 - 2a' \cos\theta' \cos\gamma + a'^2},$$
$$S'_{J/\psi K_S^0} = \frac{\sin\phi_s - 2a' \cos\theta' \sin(\phi_s + \gamma) + a'^2 \sin(\phi_s + 2\gamma)}{1 - 2a' \cos\theta' \cos\gamma + a'^2}, \qquad (9)$$
$$D'_{J/\psi K_S^0} = \frac{\cos\phi_s - 2a' \cos\theta' \cos(\phi_s + \gamma) + a'^2 \cos(\phi_s + 2\gamma)}{1 - 2a' \cos\theta' \cos\gamma + a'^2}.$$

Here, ϕ_s is the B_s^0–$\bar{B}_s^0$ mixing phase which is expected to be

$$\phi_s = -2\beta_s = -2\arg\left(-\frac{V_{ts}V_{tb}^*}{V_{cs}V_{cb}^*}\right) \qquad (10)$$

in the Standard Model, with $-2\beta_s = -0.0363^{+0.0016}_{-0.0015}$ [23, 38]. The phase ϕ_s has been directly measured in the decay $B_s^0 \to J/\psi\phi$ by the LHCb [131, 146], CDF [147], D0 [148], and ATLAS [149] experiments and additionally in $B_s^0 \to J/\psi\pi^+\pi^-$ decays by LHCb [150], resulting in a measured average of $\phi_s = 0.04^{+0.10}_{-0.13}$ [12], which is in good agreement with the Standard Model expectations and leaves only little room for New Physics enhancements in B_s^0–$\bar{B}_s^0$ mixing.

Appendix

As shown in Ch. 2, Eq. (2.23), $C'_{J/\psi K_S^0}$, $S'_{J/\psi K_S^0}$, and $D'_{J/\psi K_S^0}$ are not independent. Hence, to extract either γ or ϕ_s in addition to the penguin parameters a' and θ', an additional observable H can be measured, which is defined as

$$
\begin{aligned}
H &= \frac{1}{\epsilon} \left| \frac{\mathcal{A}}{\mathcal{A}'} \right|^2 \frac{\langle \Gamma(B_s^0 \to J/\psi K_S^0) \rangle}{\langle \Gamma(B^0 \to J/\psi K_S^0) \rangle} \frac{\Phi^d_{J/\psi K_S^0}}{\Phi^s_{J/\psi K_S^0}} \\
&= \frac{1}{\epsilon} \left| \frac{\mathcal{A}}{\mathcal{A}'} \right|^2 \frac{\Phi^d_{J/\psi K_S^0}}{\Phi^s_{J/\psi K_S^0}} \frac{\tau_d}{\tau_s} \frac{\mathcal{B}(B_s^0 \to J/\psi K_S^0)}{\mathcal{B}(B^0 \to J/\psi K_S^0)} \\
&= \frac{1 - 2a' \cos\theta' \cos\gamma + a'^2}{1 + 2\epsilon a \cos\theta \cos\gamma + \epsilon^2 a^2} \, ,
\end{aligned}
\tag{11}
$$

where the parameters $\Phi^q_{J/\psi K_S^0}$ denote phase-space factors and τ_q the average lifetimes of the B_q^0 mesons ($q = s, d$). While the time-integrated branching ratio measurement has been performed by LHCb [151],

$$
\frac{\mathcal{B}(B_s^0 \to J/\psi K_S^0)}{\mathcal{B}(B^0 \to J/\psi K_S^0)} = 0.0420 \pm 0.0049 \,(\text{stat.}) \pm 0.0023 \,(\text{syst.}),
\tag{12}
$$

the amount of data collected in 2011 has not allowed for a full analysis of the time-dependent decay rates. This comes as no surprise, as the B_s^0 production at LHCb is four times lower than for B^0 and the $B_s^0 \to J/\psi K_S^0$ decay is Cabibbo-suppressed with respect to the $B^0 \to J/\psi K_S^0$ decay, leading to 100 times fewer reconstructed $B_s^0 \to J/\psi K_S^0$ decays than $B^0 \to J/\psi K_S^0$.

By using the branching ratio measurement of $B_s^0 \to J/\psi K_S^0$ and $B^0 \to J/\psi K_S^0$ decays and including the other currently available measurements that are related to $B^0 \to J/\psi K_S^0$ via flavour $SU(3)$ together with the relevant $SU(3)$ breaking corrections, a $\Delta\phi_d = -(0.022 \pm 0.013$ [57] is found. In a similar analysis [62], a shift $\Delta S_{J/\psi K_S^0} = [0.001, 0.005]$ (at 68% CL) caused by the sub-leading penguin contributions is derived, which is well compatible with 0. Nonetheless, a measurement of the CP observables in $B_s^0 \to J/\psi K_S^0$ will considerably help to improve these analyses.

Bibliography

[1] E. Noether, *Invariante Variationsprobleme*, Gött. Nachr. 1918 (1918), pp. 235–257, DOI: 10.1080/00411457108231446, arXiv: physics/0503066 [physics].

[2] E. P. Wigner, *Symmetry and conservation laws*, Phys. Today 17 (1964), pp. 34–40, eprint: http://www.pnas.org/content/51/5/956.full.pdf+html.

[3] T. D. Lee and C. N. Yang, *Question of parity conservation in weak interactions*, Phys. Rev. 104 (1956), pp. 254–258, DOI: 10.1103/PhysRev.104.254.

[4] C. S. Wu et al., *Experimental test of parity conservation in beta decay*, Phys. Rev. 105 (1957), pp. 1413–1415, DOI: 10.1103/PhysRev.105.1413.

[5] J. H. Christenson et al., *Evidence for the 2π decay of the K_2^0 meson*, Phys. Rev. Lett. 13 (1964), pp. 138–140, DOI: 10.1103/PhysRevLett.13.138.

[6] N. Cabibbo, *Unitary symmetry and leptonic decays*, Phys. Rev. Lett. 10 (1963), pp. 531–533, DOI: 10.1103/PhysRevLett.10.531.

[7] M. Kobayashi and T. Maskawa, *CP violation in the renormalizable theory of weak interaction*, Prog. Theor. Phys. 49 (1973), pp. 652–657, DOI: 10.1143/PTP.49.652.

[8] J. R. Ellis et al., *The phenomenology of the next left-handed quarks*, Nucl. Phys. B131 (1977), p. 285, DOI: 10.1016/0550-3213(77)90374-1.

[9] S. W. Herb et al., *Observation of a dimuon resonance at 9.5 GeV in 400-GeV proton-nucleus collisions*, Phys. Rev. Lett. 39 (1977), pp. 252–255, DOI: 10.1103/PhysRevLett.39.252.

[10] B. Aubert et al., *Observation of CP violation in the B^0 meson system*, Phys. Rev. Lett. 87 (2001), p. 091801, DOI: 10.1103/PhysRevLett.87.091801.

[11] K. Abe et al., *Observation of large CP violation in the neutral B meson system*, Phys. Rev. Lett. 87 (2001), p. 091802, DOI: 10.1103/PhysRevLett.87.091802.

[12] Y. Amhis et al., *Averages of b-hadron, c-hadron, and τ-lepton properties as of early 2012* (2012), arXiv: 1207.1158 [hep-ex].

[13] S. Glashow, *Partial symmetries of weak interactions*, Nucl. Phys. 22 (1961), pp. 579–588, DOI: 10.1016/0029-5582(61)90469-2.

[14] S. Weinberg, *A model of leptons*, Phys. Rev. Lett. 19 (1967), pp. 1264–1266, DOI: 10.1103/PhysRevLett.19.1264.

[15] A. Salam and J. C. Ward, *Electromagnetic and weak interactions*, Phys. Lett. 13 (1964), pp. 168–171, DOI: 10.1016/0031-9163(64)90711-5.

[16] F. Englert and R. Brout, *Broken symmetry and the mass of gauge vector mesons*, Phys. Rev. Lett. 13 (1964), pp. 321–323, DOI: 10.1103/PhysRevLett.13.321.

Bibliography

[17] P. W. Higgs, *Broken symmetries and the masses of gauge Bosons*, Phys. Rev. Lett. 13 (1964), pp. 508–509, DOI: 10.1103/PhysRevLett.13.508.

[18] G. Guralnik, C. Hagen and T. Kibble, *Global conservation laws and massless particles*, Phys. Rev. Lett. 13 (1964), pp. 585–587, DOI: 10.1103/PhysRevLett.13.585.

[19] G. Aad et al., *Observation of a new particle in the search for the Standard Model Higgs boson with the ATLAS detector at the LHC*, Phys. Lett. B716 (2012), pp. 1–29, DOI: 10.1016/j.physletb.2012.08.020, arXiv: 1207.7214 [hep-ex].

[20] S. Chatrchyan et al., *Observation of a new boson at a mass of 125 GeV with the CMS experiment at the LHC*, Phys. Lett. B716 (2012), pp. 30–61, DOI: 10.1016/j.physletb.2012.08.021, arXiv: 1207.7235 [hep-ex].

[21] P. Ade et al., *Planck 2013 results. XVI. Cosmological parameters* (2013), arXiv: 1303.5076 [astro-ph.CO].

[22] A. Sakharov, *Violation of CP invariance, C asymmetry, and baryon asymmetry of the universe*, Pisma Zh. Eksp. Teor. Fiz. 5 (1967), pp. 32–35, DOI: 10.1070/PU1991v034n05ABEH002497.

[23] J. Charles et al., *Predictions of selected flavor observables within the standard model*, Phys. Rev. D84 (2011), p. 033005, DOI: 10.1103/PhysRevD.84.033005.

[24] R. Aaij et al., *Measurement of the time-dependent CP asymmetry in $B^0 \to J/\psi K_S^0$ decays*, Phys. Lett. B721 (2013), pp. 24–31, arXiv: 1211.6093 [hep-ex].

[25] F. Meier, *Untersuchung der Zerfallszeitbeschreibung im Zerfall $B^0 \to J/\psi K_S^0$ bei LHCb*, Master's thesis, Technische Universität Dortmund, 2012.

[26] T. Schmelzer, *Untersuchungen und Vergleich verschiedener Algorithmen zur Bestimmung von Zerfallszeiten von B-Mesonen am LHCb-Experiment*, Bachelor's thesis, Technische Universität Dortmund, 2012.

[27] S. Roese, *Implementierung der Feldman-Cousins-Methode zur Bestimmung von Konfidenzintervallen für CP-Analysen am LHCb-Experiment*, Bachelor's thesis, Technische Universität Dortmund, 2012.

[28] T. Tekampe, *Goodness-of-Fit-Tests für die $\sin 2\beta$-Analyse in $B^0 \to J/\psi K_S^0$ am LHCb-Experiment*, Bachelor's thesis, Technische Universität Dortmund, 2012.

[29] M. Schellenberg, *Analyse der VELO-Rekonstruktionseffizienz im Zerfall $B^0 \to J/\psi K_S^0$ am LHCb-Experiment*, Bachelor's thesis, Technische Universität Dortmund, 2013.

[30] O. W. Greenberg, *CPT violation implies violation of Lorentz invariance*, Phys. Rev. Lett. 89 (2002), p. 231602, DOI: 10.1103/PhysRevLett.89.231602.

[31] J. Beringer et al., *Review of particle physics, 2012-2013. Review of particle properties*, Phys. Rev. D86.1 (2012), p. 010001.

[32] C. A. Baker et al., *Improved experimental limit on the electric dipole moment of the neutron*, Phys. Rev. Lett. 97 (2006), p. 131801, DOI: 10.1103/PhysRevLett.97.131801.

[33] L. H. Ryder, *Quantum field theory*, Cambridge: Cambridge Univ. Press, 1996, ISBN: 0-521-47814-6.

[34] M. Kaku, *Quantum field theory: a modern introduction*, New York, NY: Oxford Univ. Press, 1993.

[35] L.-L. Chau and W.-Y. Keung, *Comments on the parametrization of the Kobayashi-Maskawa matrix*, Phys. Rev. Lett. 53 (1984), pp. 1802–1805, DOI: 10.1103/PhysRevLett. 53.1802.

[36] L. Wolfenstein, *Parametrization of the Kobayashi-Maskawa Matrix*, Phys. Rev. Lett. 51 (1983), pp. 1945–1947, DOI: 10.1103/PhysRevLett.51.1945.

[37] A. J. Buras, M. E. Lautenbacher and G. Ostermaier, *Waiting for the top quark mass, $K^+ \to \pi^+ \nu \bar{\nu}$, $B_s^0 - \bar{B}_s^0$ mixing, and CP asymmetries in B decays*, Phys. Rev. D50 (1994), pp. 3433–3446, DOI: 10.1103/PhysRevD.50.3433.

[38] J. Charles et al., *CP violation and the CKM matrix: Assessing the impact of the asymmetric B factories*, Eur. Phys. J. C41 (2005), pp. 1–131, DOI: 10.1140/epjc/s2005-02169-1, arXiv: hep-ph/0406184 [hep-ph].

[39] C. Jarlskog, *Commutator of the quark mass matrices in the Standard Electroweak Model and a measure of maximal CP violation*, Phys. Rev. Lett. 55 (1985), p. 1039, DOI: 10. 1103/PhysRevLett.55.1039.

[40] G. C. Branco, L. Lavoura and J. P. Silva, *CP violation*, vol. 103, 1999, ISBN: 0 19 8503997.

[41] I. I. Bigi and A. Sanda, *CP violation*, vol. 9, Cambridge monographs on particle physics, nuclear physics, and cosmology, Cambridge University Press, 2000, pp. 1–382.

[42] P. F. e. Harrison and H. R. e. Quinn, *The BABAR physics book: Physics at an asymmetric B factory*, Stanford, CA: SLAC, 1998.

[43] V. Weisskopf and E. Wigner, *Über die natürliche Linienbreite in der Strahlung des harmonischen Oszillators*, Z. Phys. 65 (1930), pp. 18–29, DOI: 10.1007/BF01397406.

[44] V. Weisskopf and E. P. Wigner, *Berechnung der natürlichen Linienbreite auf Grund der Diracschen Lichttheorie*, Z. Phys. 63 (1930), pp. 54–73, DOI: 10.1007/BF01336768.

[45] R. Aaij et al., *First observation of CP violation in the decays of B_s^0 mesons*, Phys. Rev. Lett. 110 (2013), p. 221601, DOI: 10.1103/PhysRevLett.110.221601, arXiv: 1304.6173 [hep-ex].

[46] R. Aaij et al., *Measurement of the flavour-specific CP-violating asymmetry a_{sl}^s in B_s^0 decays*, Phys. Lett. (2013), arXiv: 1308.1048 [hep-ex].

[47] R. Aaij et al., *Measurement of the flavour-specific CP violating asymmetry $a_s l^s$ in B_s decays*, LHCb conference note CERN-LHCb-CONF-2012-022, CERN, 2012.

[48] J. Eeg and I. Picek, *On the double penguin like contributions to the $B^0 - \bar{B}^0$ mixing*, Z. Phys. C39 (1988), p. 521, DOI: 10.1007/BF01555981.

[49] J. S. Hagelin, *Mass mixing and CP violation in the $B^0 - \bar{B}^0$ system*, Nucl. Phys. B193 (1981), pp. 123–149, DOI: 10.1016/0550-3213(81)90521-6.

[50] J. S. Hagelin and M. B. Wise, *Comment on CP violation in $B^0 - \bar{B}^0$ mixing*, Nucl. Phys. B189 (1981), p. 87, DOI: 10.1016/0550-3213(81)90082-1.

[51] T. Inami and C. S. Lim, *Effects of superheavy quarks and leptons in low-energy weak processes $K_L \to \mu\bar{\mu}$, $K^+ \to \pi^+\nu\bar{\nu}$ and $K^0 \leftrightarrow \overline{K}^0$*, Prog. Theor. Phys. 65.1 (1981), pp. 297–314, DOI: 10.1143/PTP.65.297, eprint: http://ptp.oxfordjournals.org/content/65/1/297.full.pdf+html.

[52] A. Buras, W. Slominski and H. Steger, *B^0–$\bar{B}^0$ mixing, CP violation and the B meson decay*, Nucl. Phys. B245 (1984), p. 369, DOI: 10.1016/0550-3213(84)90437-1.

[53] A. Lenz and U. Nierste, *Theoretical update of B_s^0–$\bar{B}_s^0$ mixing*, JHEP 0706 (2007), p. 072, DOI: 10.1088/1126-6708/2007/06/072, arXiv: hep-ph/0612167 [hep-ph].

[54] A. Lenz and U. Nierste, *Numerical updates of lifetimes and mixing parameters of B mesons*, *6th International Workshop on the CKM Unitarity Triangle (CKM 2010)*, ed. by T. Gershon, 2011, arXiv: 1102.4274 [hep-ph].

[55] S. Faller et al., *The golden modes $B^0 \to J/\psi K_{S,L}^0$ in the era of precision flavour physics*, Phys. Rev. D79 (2008), 014030. 4 p, DOI: 10.1103/PhysRevD.79.014030, arXiv: 0809.0842 [79].

[56] R. Fleischer, *Extracting γ from $B_{s(d)} \to J/\psi K_S$ and $B_{d(s)} \to D_{d(s)}^+ D_{d(s)}^-$*, Eur. Phys. J. (1999), pp. 299–306, DOI: 10.1007/s100529900099, arXiv: hep-ph/9903455v1 [hep-ph].

[57] R. Fleischer, *Penguin effects in $\phi_{d,s}$ determinations* (2012), arXiv: 1212.2792 [hep-ph].

[58] M. Gronau, *Large penguin effects in the CP asymmetry of $B^0 \to \pi^+\pi^-$*, Phys. Lett. B300 (1993), pp. 163–168, DOI: 10.1016/0370-2693(93)90765-A, arXiv: hep-ph/9209279 [hep-ph].

[59] G. Kramer and W. Palmer, *Electroweak and strong penguins in $B^{\pm,0} \to \pi\pi$, πK, and KK decays*, Phys. Rev. D52 (1995), pp. 6411–6421, DOI: 10.1103/PhysRevD.52.6411, arXiv: hep-ph/9507329 [hep-ph].

[60] A. Dighe et al., *The width difference of B_d mesons*, PoS HEP2001 (2001), p. 096, arXiv: hep-ph/0112067 [hep-ph].

[61] A. Dighe et al., *Measurement of the lifetime difference of B_d mesons: Possible and worthwhile?*, Nucl. Phys. B624 (2002), pp. 377–404, DOI: 10.1016/S0550-3213(01)00655-1, arXiv: hep-ph/0109088 [hep-ph].

[62] M. Jung, *Determining weak phases from $B \to J/\psi P$ decays*, Phys. Rev. D86 (2012), p. 053008, DOI: 10.1103/PhysRevD.86.053008, arXiv: 1206.2050 [hep-ph].

[63] I. Adachi et al., *Precise measurement of the CP violation parameter $\sin 2\phi_1$ in $B^0 \to (c\bar{c})K^0$ decays*, Phys. Rev. Lett. 108 (2012), p. 171802, DOI: 10.1103/PhysRevLett.108.171802, arXiv: 1201.4643 [hep-ex].

[64] B. Aubert et al., *Measurement of time-dependent CP asymmetry in $B^0 \to c\bar{c}K^{(*)0}$ decays*, Phys. Rev. D79 (2009), p. 072009, DOI: 10.1103/PhysRevD.79.072009, arXiv: 0902.1708 [hep-ex].

[65] M. Bona et al., *The 2004 UTfit collaboration report on the status of the unitarity triangle in the standard model*, JHEP 0507 (2005), p. 028, DOI: 10.1088/1126-6708/2005/07/028, arXiv: hep-ph/0501199 [hep-ph].

[66] L. Evans and P. Bryant, *LHC machine*, JINST 3 (2008), ed. by L. Evans, S08001, DOI: 10.1088/1748-0221/3/08/S08001.

[67] C. Lefevre et al., *LHC: The guide*, 2009.

[68] G. Rumolo et al., *LHC experience with different bunch spacings in 2011*, Proceedings of Workshop on LHC performance, ed. by C. Carli, 2012.

[69] G. Aad et al., *The ATLAS experiment at the CERN Large Hadron Collider*, JINST 3 (2008), S08003, DOI: 10.1088/1748-0221/3/08/S08003.

[70] S. Chatrchyan et al., *The CMS experiment at the CERN LHC*, JINST 3 (2008), S08004, DOI: 10.1088/1748-0221/3/08/S08004.

[71] K. Aamodt et al., *The ALICE experiment at the CERN LHC*, JINST 3 (2008), S08002, DOI: 10.1088/1748-0221/3/08/S08002.

[72] G. Anelli et al., *The TOTEM experiment at the CERN Large Hadron Collider*, JINST 3 (2008), S08007, DOI: 10.1088/1748-0221/3/08/S08007.

[73] O. Adriani et al., *The LHCf detector at the CERN Large Hadron Collider*, JINST 3 (2008), S08006, DOI: 10.1088/1748-0221/3/08/S08006.

[74] J. Pinfold, *MoEDAL becomes the LHC's magnificent seventh*, CERN Cour. 50N4 (2010), pp. 19–20.

[75] R. Aaij et al., *Measurement of $\sigma(pp \to b\bar{b}X)$ at $\sqrt{s} = 7\,TeV$ in the forward region*, Phys. Lett. B694 (2010), pp. 209–216, DOI: 10.1016/j.physletb.2010.10.010, arXiv: 1009.2731 [hep-ex].

[76] R. W. Lambert and F. Muheim, *Generator study of the production asymmetry in LHCb*, LHCb public note LHCb-2007-124. CERN-LHCb-2007-124, CERN, 2007.

[77] R. Aaij et al., *Measurement of b-hadron production fractions in 7 TeV pp collisions*, Phys. Rev. D85 (2012), p. 032008, DOI: 10.1103/PhysRevD.85.032008, arXiv: 1111.2357 [hep-ex].

[78] M. Chaichian and A. Fridman, *On a possibility for measuring effects of CP violation at pp colliders*, Phys. Lett. B298 (1993), pp. 218–223, ISSN: 0370-2693, DOI: 10.1016/0370-2693(93)91733-4.

[79] E. Norrbin and T. Sjostrand, *Production and hadronization of heavy quarks*, Eur. Phys. J. C17 (2000), pp. 137–161, DOI: 10.1007/s100520000460, arXiv: hep-ph/0005110 [hep-ph].

[80] E. Norrbin and R. Vogt, *Bottom production asymmetries at the LHC*, Proceedings of the CERN 1999 Workshop on SM physics (and more) at the LHC (2000), arXiv: hep-ph/0003056 [hep-ph].

[81] P. Aarnio et al., *The DELPHI detector at LEP*, Nucl. Instrum. Meth. A303 (1991), pp. 233–276, DOI: 10.1016/0168-9002(91)90793-P.

[82] A. A. Alves Jr. et al., *The LHCb detector at the LHC*, JINST 3 (2008), S08005, DOI: 10.1088/1748-0221/3/08/S08005.

[83] F. Alessio, R. Jacobsson and S. Schleich, *The LHCb online framework for experiment protection, and global operational control and monitoring*, J. Phys. Conf. Ser. 331 (2011), p. 022002, DOI: 10.1088/1742-6596/331/2/022002.

[84] T. Ruf, *Panoramix PR images*, ed. by T. Ruf, 2013, URL: http://lhcb-reconstruction.web.cern.ch/lhcb-reconstruction.

[85] P. Cerenkov, *Visible luminescence of pure fluids induced by gamma rays*, Dokl. Akad. Nauk Ser. Fiz. 2 (1934), pp. 451–454.

[86] P. Cerenkov, *Visible radiation produced by electrons moving in a medium with velocities exceeding that of light*, Phys. Rev. 52 (1937), pp. 378–379, DOI: 10.1103/PhysRev.52.378.

[87] M. Kraan, *VELO tank with cutaway view including modules*, ed. by LHCb VELO Group, 2013, URL: https://lbtwiki.cern.ch/bin/view/VELO/VELOConferencePlots.

[88] T. Ruf, *RICH1 HPD Panels*, ed. by T. Ruf, 2013, URL: http://lhcb-reconstruction.web.cern.ch/lhcb-reconstruction/panoramix/running_panoramix.htm.

[89] R. Aaij et al., *The LHCb trigger and its performance in 2011*, JINST 8 (2013), P04022, DOI: 10.1088/1748-0221/8/04/P04022, arXiv: 1211.3055.

[90] G. Barrand et al., *GAUDI - A software architecture and framework for building HEP data processing applications*, Comput. Phys. Commun. 140 (2001), pp. 45–55, DOI: 10.1016/S0010-4655(01)00254-5.

[91] R. Aaij et al., *The Brunel project*, ed. by M. Cattaneo, 2013, URL: http://lhcb-release-area.web.cern.ch/LHCb-release-area/DOC/brunel/.

[92] D. Hutchcroft, *VELO pattern recognition*, LHCb public note CERN-LHCb-2007-013, CERN, 2007.

[93] O. Callot, *FastVelo, a fast and efficient pattern recognition package for the Velo*, LHCb public note CERN-LHCb-PUB-2011-001, CERN, 2011.

[94] P. E. Hart, *How the Hough transform was invented*, Sig.Proc.Mag. 26.6 (2009), pp. 18–22, DOI: 10.1109/msp.2009.934181.

[95] R. E. Kalman, *A new approach to linear filtering and prediction problems*, J. Basic Eng. 82 (Series D) (1960), pp. 35–45.

[96] V. Belyaev, V. Egorychev and D. Golubkov, *Study of π^0/γ reconstruction efficiency with 2011 data*, LHCb internal note CERN-LHCb-INT-2012-001, Geneva: CERN, 2012.

[97] R. Aaij et al., *The DaVinci project*, ed. by C. Jones, 2013, URL: http://lhcb-release-area.web.cern.ch/LHCb-release-area/DOC/davinci/.

[98] I. Antcheva et al., *ROOT: A C++ framework for petabyte data storage, statistical analysis and visualization*, Comp. Phys. Commun. 182 (2011), pp. 1384–1385, DOI: 10.1016/j.cpc.2011.02.008.

[99] M. Clemencic et al., *The LHCb simulation application, Gauss: Design, evolution and experience*, J. Phys. Conf. Ser. 331 (2011), p. 032023, DOI: 10.1088/1742-6596/331/3/032023.

[100]   I. Belyaev et al., *Handling of the generation of primary events in Gauss, the LHCb simulation framework*, J. Phys. Conf. Ser. 331 (2011), p. 032047, DOI: 10.1088/1742-6596/331/3/032047.

[101]   R. Aaij et al., *The Boole project*, ed. by M. Cattaneo, 2013, URL: http://lhcb-release-area.web.cern.ch/LHCb-release-area/DOC/boole/.

[102]   T. Sjostrand et al., *High-energy physics event generation with PYTHIA 6.1*, Comput. Phys. Commun. 135 (2001), pp. 238–259, DOI: 10.1016/S0010-4655(00)00236-8, arXiv: hep-ph/0010017 [hep-ph].

[103]   T. Sjostrand, S. Mrenna and P. Z. Skands, *PYTHIA 6.4 physics and manual*, JHEP 0605 (2006), p. 026, DOI: 10.1088/1126-6708/2006/05/026, arXiv: hep-ph/0603175 [hep-ph].

[104]   D. Lange, *The EvtGen particle decay simulation package*, Nucl. Instrum. Meth. A462 (2001), pp. 152–155, DOI: 10.1016/S0168-9002(01)00089-4.

[105]   P. Golonka and Z. Was, *PHOTOS Monte Carlo: A precision tool for QED corrections in Z and W decays*, Eur. Phys. J. C45 (2006), pp. 97–107, DOI: 10.1140/epjc/s2005-02396-4, arXiv: hep-ph/0506026 [hep-ph].

[106]   A. Buckley et al., *General-purpose event generators for LHC physics*, Phys. Rept. 504 (2011), pp. 145–233, DOI: 10.1016/j.physrep.2011.03.005, arXiv: 1101.2599 [hep-ph].

[107]   M. Bahr et al., *Herwig++ physics and manual*, Eur. Phys. J. C58 (2008), pp. 639–707, DOI: 10.1140/epjc/s10052-008-0798-9, arXiv: 0803.0883 [hep-ph].

[108]   T. Gleisberg et al., *SHERPA 1.alpha: A proof of concept version*, JHEP 0402 (2004), p. 056, DOI: 10.1088/1126-6708/2004/02/056, arXiv: hep-ph/0311263 [hep-ph].

[109]   T. Gleisberg et al., *Event generation with SHERPA 1.1*, JHEP 0902 (2009), p. 007, DOI: 10.1088/1126-6708/2009/02/007, arXiv: 0811.4622 [hep-ph].

[110]   S. Agostinelli et al., *GEANT4: A simulation toolkit*, Nucl. Instrum. Meth. A506 (2003), pp. 250–303, DOI: 10.1016/S0168-9002(03)01368-8.

[111]   J. Allison et al., *GEANT4 developments and applications*, IEEE Trans. Nucl. Sci. 53 (2006), p. 270, DOI: 10.1109/TNS.2006.869826.

[112]   R. Jacobsson, *Performance of the LHCb detector during the LHC proton runs 2010–2012*, *Nuclear Science Symposium and Medical Imaging Conference (NSS/MIC), 2012 IEEE*, ed. by B. Yu, Anaheim, CA, 2012, pp. 1479–1486, ISBN: 978-1-4673-2028-3, DOI: 10.1109/NSSMIC.2012.6551357.

[113]   K. T. McDonald, *Maximum-likelihood analysis of CP-violating asymmetries*, tech. rep. PRINCETON-HEP-92-04, Princeton, NJ: Princeton Univ., 1992.

[114]   M. Beyer, *CP violation in particle, nuclear, and astrophysics*, ed. by M. Beyer, Lecture Notes in Physics, Springer, 2010, ISBN: 9783642078309.

[115]   R. Aaij et al., *Measurement of B meson production cross-sections in proton-proton collisions at $\sqrt{s} = 7$ TeV*, JHEP 1308 (2013), p. 117, DOI: 10.1007/JHEP08(2013)117, arXiv: 1306.3663 [hep-ex].

[116] R. Aaij et al., *Opposite-side flavour tagging of B mesons at the LHCb experiment*, Eur. Phys. J. C72 (2012), DOI: 10.1140/epjc/s10052-012-2022-1, arXiv: 1202.4979 [hep-ex].

[117] M. G. Gándara, *Flavour tagging developments within the LHCb experiment*, Doctoral dissertation, Universitat de Barcelona, 2012.

[118] R. Aaij et al., *Performance of flavour tagging algorithms optimised for the analysis of* $B_s^0 \to J/\psi\phi$, LHCb conference note CERN-LHCb-CONF-2012-026, CERN, 2012.

[119] H.-G. Moser and A. Roussarie, *Mathematical methods for* B^0–$\overline{B}^0$ *oscillation analyses*, Nucl. Instrum. Meth. A384.2–3 (1997), pp. 491–505, DOI: 10.1016/S0168-9002(96)00887-X.

[120] C. Biino and S. Palestini, *Sensitivity to mixing and CP violation in the* B^0–$\overline{B}^0$ *systems by decay distribution study*, La Rivista del Nuovo Cimento 14 (1991), pp. 1–23, ISSN: 0393-697X, DOI: 10.1007/BF02813497.

[121] W. D. Hulsbergen, *Decay chain fitting with a Kalman filter*, Nucl. Instrum. Meth. A552 (2005), pp. 566–575, DOI: 10.1016/j.nima.2005.06.078, arXiv: physics/0503191 [physics].

[122] V. Blobel and E. Lohrmann, *Statistische und numerische Methoden der Datenanalyse*, 1st ed., Teubner Verlag, 1998, ISBN: 3519032430.

[123] G. Cowan, *Statistical data analysis*, Oxford University Press, Oxford, 1998, ISBN: 0-19-850155-2.

[124] F. James, *Statistical methods in experimental physics*, World Scientific, 2006, ISBN: 9789812567956.

[125] F. James and M. Roos, *MINUIT: A system for function minimization and analysis of the parameter errors and correlations*, Comput. Phys. Commun. 10 (1975), pp. 343–367, DOI: 10.1016/0010-4655(75)90039-9.

[126] F. James, *MINUIT homepage of the LCG project*, ed. by F. James, CERN, 2013, URL: https://seal.web.cern.ch/seal/work-packages/mathlibs/minuit/index.html (visited on 21/08/2013).

[127] F. James, *The interpretation of errors*, Technical report, CERN, 2004.

[128] R. Aaij et al., *Optimization and calibration of the LHCb flavour tagging performance using 2010 data*, LHCb conference note CERN-LHCb-CONF-2011-003, CERN, 2011.

[129] R. Aaij et al., *Search for CP violation in* $B^0 \to J/\psi K_S^0$ *decays with first LHCb data*, LHCb conference note CERN-LHCb-CONF-2011-004, CERN, 2011.

[130] M. Calvi et al., *Lifetime unbiased selection of* $B_s^0 \to J/\psi\phi$ *and related control channels:* $B_d \to J/\psi K*$ *and* $B^+ \to J/\psi K+$, LHCb public note CERN-LHCb-2009-025, CERN, 2009.

[131] R. Aaij et al., *Measurement of the CP-violating phase* ϕ_s *in the decay* $B_s^0 \to J/\psi\phi$, Phys. Rev. Lett. 108 (2012), p. 101803, DOI: 10.1103/PhysRevLett.108.101803, arXiv: 1112.3183 [hep-ex].

[132] M. Pivk and F. R. Le Diberder, *sPlot: A statistical tool to unfold data distributions*, Nucl. Instrum. Meth. A555 (2005), pp. 356–369, DOI: 10.1016/j.nima.2005.08.106, arXiv: physics/0402083 [`physics.data-an`].

[133] R. Aaij et al., *First evidence of direct CP violation in charmless two-body decays of B_s^0 mesons*, Phys. Rev. Lett. 108 (2012), p. 201601, DOI: 10.1103/PhysRevLett.108.201601, arXiv: 1202.6251 [`hep-ex`].

[134] R. Aaij et al., *Measurement of time-dependent CP violation in charmless two-body B decays*, LHCb conference note CERN-LHCb-CONF-2012-007, CERN, 2012.

[135] M. Oreglia, *A study of the reactions $\psi' \to \gamma\gamma\psi$*, Doctoral dissertation, Stanford University, 1980.

[136] J. Gaiser, *Charmonium spectroscopy from radiative decays of the J/ψ and ψ'*, Doctoral dissertation, Stanford University, 1982.

[137] T. Skwarnicki, *A study of the radiative CASCADE transitions between the Upsilon-Prime and Upsilon resonances*, Doctoral dissertation, Institute of Nuclear Physics Cracow, 1986.

[138] R. Aaij et al., *Measurements of the B^+, B^0, B_s^0 meson and Λ_b^0 baryon lifetimes*, (in preparation) (2013).

[139] W. Verkerke and D. P. Kirkby, *The RooFit toolkit for data modeling*, eConf C0303241 (2003), MOLT007, arXiv: physics/0306116 [`physics`].

[140] R. Aaij et al., *Measurement of b-hadron masses*, Phys. Lett. B708 (2012), pp. 241–248, DOI: 10.1016/j.physletb.2012.01.058, arXiv: 1112.4896 [`hep-ex`].

[141] G. J. Feldman and R. D. Cousins, *A unified approach to the classical statistical analysis of small signals*, Phys. Rev. D57 (1998), pp. 3873–3889, DOI: 10.1103/PhysRevD.57.3873, arXiv: physics/9711021 [`physics.data-an`].

[142] P. Koppenburg, *Dealing with multiple candidates*, LHCb internal note CERN-LHCb-INT-2011-009, CERN, 2011.

[143] M. Needham, *Momentum scale calibration using resonances*, LHCb public note CERN-LHCb-2008-037, CERN, 2008.

[144] R. Aaij et al., *Implications of LHCb measurements and future prospects*, Eur. Phys. J. C73 (2013), p. 2373, DOI: 10.1140/epjc/s10052-013-2373-2, arXiv: 1208.3355 [`hep-ex`].

[145] S. Faller, R. Fleischer and T. Mannel, *Precision physics with $B_s^0 \to J/\psi\phi$ at the LHC: The quest for New Physics*, Phys. Rev. D79 (2009), p. 014005, DOI: 10.1103/PhysRevD.79.014005, arXiv: 0810.4248 [`hep-ph`].

[146] R. Aaij et al., *Measurement of CP violation and the B_s^0 meson decay width difference with $B_s^0 \to J/\psi K^+K^-$ and $B_s^0 \to J/\psi\pi^+\pi^-$ decays*, Phys. Rev. D87 (2013), p. 112010, DOI: 10.1103/PhysRevD.87.112010, arXiv: 1304.2600 [`hep-ex`].

[147] T. Aaltonen et al., *Measurement of the CP-violating phase $\beta_s^{J/\psi\phi}$ in $B_s^0 \to J/\psi\phi$ decays with the CDF II detector*, Phys. Rev. D85 (2012), p. 072002, DOI: 10.1103/PhysRevD.85.072002, arXiv: 1112.1726 [`hep-ex`].

[148]   V. M. Abazov et al., *Measurement of the CP-violating phase* $\phi_s^{J/\psi\phi}$ *using the flavor-tagged decay* $B_s^0 \to J/\psi\phi$ *in 8 fb^{-1} of p$\bar{p}$ collisions*, Phys. Rev. D85 (2012), p. 032006, DOI: 10.1103/PhysRevD.85.032006, arXiv: 1109.3166 [hep-ex].

[149]   G. Aad et al., *Time-dependent angular analysis of the decay* $B_s^0 \to J/\psi\phi$ *and extraction of* $\Delta\Gamma_s$ *and the CP-violating weak phase* ϕ_s *by ATLAS*, JHEP 1212 (2012), p. 072, DOI: 10.1007/JHEP12(2012)072, arXiv: 1208.0572 [hep-ex].

[150]   R. Aaij et al., *Measurement of the CP-violating phase* ϕ_s *in* $\bar{B}_s^0 \to J/\psi\pi^+\pi^-$ *decays*, Phys. Lett. B713 (2012), pp. 378–386, DOI: 10.1016/j.physletb.2012.06.032, arXiv: 1204.5675 [hep-ex].

[151]   R. Aaij et al., *Measurement of the* $B_s^0 \to J/\psi K_S^0$ *branching fraction*, Phys. Lett. B713 (2012), pp. 172–179, DOI: 10.1016/j.physletb.2012.05.062, arXiv: 1205.0934 [hep-ex].

Acknowledgements